Nonideal Turbulence

Anna von der Heydt

2003

Ph.D. thesis
University of Twente

Twente University **Press**

Also available in print:
http://www.tup.utwente.nl/

NONIDEAL TURBULENCE

The research described in this thesis was funded by GIF (German Israel Foundation). The research was carried out at the Physics of Fluids group of the University of Twente and the University of Marburg.

Twente University **Press**

Publisher:
Twente University Press,
P.O Box 217, 7500 AE Enschede, The Netherlands
www.tup.utwente.nl

Cover design: Anna von der Heydt
Print: Océ Facility Services, Enschede

ISBN 9036519039

NONIDEAL TURBULENCE

PROEFSCHRIFT

ter verkrijging van
de graad van doctor aan de Universiteit Twente,
op gezag van de rector magnificus,
prof. dr. F.A. van Vught,
volgens besluit van het College voor Promoties
in het openbaar te verdedigen
op donderdag 24 april 2003 te 13.15 uur

door

Anna von der Heydt

geboren op 29 april 1974
te Regensburg, Duitsland.

Dit proefschrift is goedgekeurd door de promotoren:

prof. dr. D. Lohse

prof. dr. S. Grossmann

Table of Contents

Chapter 1

Introduction

1.1 What is turbulence?

Most flows occurring in nature and in engineering applications are turbulent. This can be easily observed in our every day's life. The water in rivers or waterfalls is turbulent. The smoke out of a chimney does not rise linearly, but we notice whorls and eddies of all sizes. Watching the motion of dancing leaves on a stormy autumn day indicates that the air motion is strongly turbulent. On a larger scale, the atmosphere of the earth is most of the time turbulent as are the water currents in the oceans. The air or water behind a moving car, airplane or ship is not calm, but highly turbulent. All these flows have in common that they are very unsteady and irregular, they look chaotic and unpredictable. Furthermore, always a large number of different length scales is involved. There exist many concepts of turbulence. However, most of them assume *ideal* flows, i.e., isotropic, homogeneous and stationary flows. We will introduce some of these concepts first. Obviously, most of the above given examples are in a way *nonideal*, in the sense that they may be anisotropic or inhomogeneous, as e.g. the flow in a river, or non-stationary as e.g. the pulsed flow through a pipeline. Some of these nonideal properties are the subject of this thesis.

The governing equation of fluid motion, the Navier-Stokes equation, is the conservation law of momentum:

$$\frac{\partial \boldsymbol{u}(\boldsymbol{x},t)}{\partial t} + \boldsymbol{u}(\boldsymbol{x},t) \cdot \nabla \boldsymbol{u}(\boldsymbol{x},t) = -\frac{1}{\rho} \nabla p(\boldsymbol{x},t) + \nu \Delta \boldsymbol{u}(\boldsymbol{x},t). \qquad (1.1)$$

It is known since 150 years [1]. Here $\boldsymbol{u}(\boldsymbol{x},t)$ is the velocity field, ρ the density of the fluid, p the pressure, and ν the kinematic viscosity. We restrict ourselves to incompressible flows, i.e., the density of the fluid is assumed to be constant. The conservation of mass reflected in the continuity equation then reduces to

$$\nabla \cdot \boldsymbol{u}(\boldsymbol{x}, t) = 0. \tag{1.2}$$

These two equations are completed by boundary conditions, often represented by an additional external driving force term ($+\boldsymbol{f}(\boldsymbol{x}, t)$ on the right hand side of Eq. (1.1)). In addition, other external forces may be added. The basic general properties of turbulence can be understood from the two equations. However, it is not possible to find solutions for all details, and in particular, to understand the tremendous amount of applications arising due to all kinds of different boundary conditions. The nonlinear term in Eq.(1.1) is the origin of the chaotic and self-similar behavior of the velocity. It is also this term which causes the ability of turbulent flows to mix the fluid much more efficiently than laminar flows.

How can we decide whether a flow is laminar or turbulent? There is one dimensionless parameter, defined by typical length and velocity scales L and U together with the kinematic viscosity ν, the Reynolds number (O. Reynolds (1883), [2])

$$Re \equiv \frac{UL}{\nu}. \tag{1.3}$$

L and U are determined by the boundary conditions or the external stirring force $\boldsymbol{f}$, which acts on the scale L and produces velocity differences on this scale of size U. If we write the Navier-Stokes equation in nondimemsional form by introducing the dimensionless time $\tilde{t} = tU/L$, length $\tilde{x} = x/L$ and velocity $\tilde{u} = u/U$, the Reynolds number determines the relative weight between the linear viscous term $\propto \nu \Delta \boldsymbol{u}$ and the nonlinear term $\propto \boldsymbol{u} \cdot \nabla \boldsymbol{u}$:

$$\frac{\partial \tilde{\boldsymbol{u}}(\tilde{\boldsymbol{x}}, \tilde{t})}{\partial \tilde{t}} + \tilde{\boldsymbol{u}}(\tilde{\boldsymbol{x}}, \tilde{t}) \cdot \tilde{\nabla} \tilde{\boldsymbol{u}}(\tilde{\boldsymbol{x}}, \tilde{t}) = -\tilde{\nabla} \tilde{p}(\tilde{\boldsymbol{x}}, \tilde{t}) + \frac{1}{Re} \tilde{\Delta} \tilde{\boldsymbol{u}}(\tilde{\boldsymbol{x}}, \tilde{t}) \tag{1.4}$$

with $\tilde{p} = p/(\rho U^2)$. If the product UL is much larger than the viscosity, i.e., Re is large, then the nonlinear term in the Navier-Stokes equation dominates the linear term, meaning that the convective transport of energy in the flow is larger than the energy loss by viscous dissipation. Turbulent flows have large Reynolds numbers. Different flows with different U, L, and ν but with the same Reynolds number obey to the same dimensionless equation if their velocities are scaled by U, lengths by L and times by L/U. Consequently, the physical properties of different flows with the same Reynolds number are similar.

Turbulence can be maintained only if an external stirring force or the boundaries continuously introduce energy into the system. This energy is dissipated by viscous forces. In this sense, a turbulent flow is not a closed system, but energy travels through it all the time. A basic concept has been introduced by Richardson (1922) [2, 3], namely the energy cascade in turbulent flows. The idea is, that the energy is fed into the fluid system by the driving forces on a large length scale, i.e., the forcing produces large eddies of sizes comparable to the characteristic length scale L. The eddies have large Reynolds numbers, $Re = LU/\nu$. It is observed that they are unstable. They break up and transfer their kinetic energy to smaller eddies. These eddies again split into smaller ones, and so on. The energy cascade continues until the resulting eddies are stable, i.e., the Reynolds number of these eddies of scale l, $Re(l) = lu(l)/\nu$, is small enough. Then, the viscous linear term in Eq.(1.1) is larger than the nonlinear term and the kinetic energy is dissipated by viscosity. Of course, in a statistically stationary situation, the total energy dissipation rate $\epsilon = \nu \langle\langle \frac{\partial u_i}{\partial x_j} \frac{\partial u_i}{\partial x_j} \rangle\rangle$ must equal the amount of energy which was originally put into the system by the driving force or via the boundaries. This implies $\epsilon = \langle\langle f_i u_i \rangle\rangle$. The brackets $\langle\langle ... \rangle\rangle$ denote the temporal and spatial average.

The idea of the energy cascade also enters in the classical K41 scaling theory by Kolmogorov [4], Obukhov [5], Heisenberg [6], Weizsäcker [7], and Onsager [8] from the 1940's for the moments of velocity differences

$$v_r \equiv u(x + r) - u(x) \tag{1.5}$$

in fully developed turbulence. There is an inertial subrange (ISR), where the energy is solely transferred from larger to smaller scales by the energy cascade mechanism. In this range, the only relevant physical quantity is the dissipation rate ϵ. Dimensional arguments then lead to scaling laws for the moments $\langle\langle v_r^n \rangle\rangle$ as

$$\langle\langle v_r^n \rangle\rangle \propto (\epsilon r)^{\zeta_n}, \qquad \text{with} \quad \zeta_n = n/3. \tag{1.6}$$

On very small scales instead, viscosity becomes more important. In this range, the viscous subrange (VSR), where most of the energy dissipation occurs, the moments scale like $\langle\langle v_r^n \rangle\rangle \propto r^n$. The crossover between the two scaling regimes takes place at $r \simeq 9\eta$, where η is the Kolmogorov dissipation scale $\eta \equiv \left(\frac{\nu^3}{\epsilon}\right)^{1/4}$, [2, 9].

In a variable-range mean-field theory by Effinger and Grossmann [10] it is shown that these scaling exponents for the second order velocity structure function $D(r) = \langle\langle v_r^2 \rangle\rangle$ can be derived from the Navier-Stokes equation within that theory without using dimensional analysis. This theory uses a scale-dependent decomposition of the velocity field. Also the crossover scale and the Kolmogorov constant b, which is the prefactor in the scaling law for the second order structure function, i.e., $D(r) = b(\epsilon r)^{2/3}$, can be determined from this theory in accordance with experimental data. This method will be used in parts of this present work.

A turbulent velocity signal is strongly fluctuating in space and time. The velocity behaves intermittently, meaning that there are calm periods and sudden bursts of strong fluctuations. Also the energy is not directly transported from large to small scales, but there is considerable transport of energy from small to large scales, as well. Only on average, the energy is transported down the energy cascade. These fluctuations lead to deviations from the K41 scaling exponents: the intermittency corrections. The latter are particularly large for the higher order moments, $\zeta_n < n/3$ for $n > 3$, [2]. For the second order velocity structure function the deviations are only small, $\zeta_2 \simeq 0.7$ instead of $2/3$. The mean-field approach [10] neglects these fluctuations, and therefore reproduces the K41 scaling of the second order structure function $D(r) = b(\epsilon r)^{2/3}$.

These concepts of turbulence all use the properties of *ideal* turbulence, i.e., they assume isotropy, homogeneity, and statistical stationarity. However, as was pointed out in the beginning of this chapter, for almost all realistic flows at least one of these assumptions is not valid. In other words, most of the time we have to deal with *nonideal* turbulence. The question, which immediately arises is, whether the basic properties of turbulence are changed in nonideal turbulent flows. In this thesis we will study some aspects of nonideal turbulence on a fundamental level. The variable-range mean-field theory is a powerful tool for this purpose and will be used extensively. Consequently, intermittency corrections will not be considered, but we will focus on the mean-field properties of nonideal turbulent flows. Only in Chapter 4 we will study numerical models including turbulent fluctuations in order to compare with the mean-field results.

Still, nature is much more complicated. Usually, not only one of the above mentioned ideal properties are broken. Furthermore, we have to deal with compressibility, multi-phase flows, etc. One striking example from nature which can be explained within a simplified model is studied in Chapter 5. It is the snap of the snapping shrimp.

1.2 Nonideal turbulence – a guide through the chapters

In Chapter 2 (see also *Scaling Exponents in Weakly Anisotropic Turbulence from the Navier-Stokes Equation* [11]) we consider a turbulent flow which is homogeneous and statistically stationary, but is driven by **weakly anisotropic** forces. As an example we may regard a shear flow far enough away from the boundaries to ensure homogeneity. The variable-range mean-field theory [10] can be extended to this case of weak anisotropy and scaling laws for the second order structure function can be derived.

In general, the second order structure function is a tensor, i.e.,

$$D_{ik}(\boldsymbol{r}) = \langle\langle v_i(\boldsymbol{r}) v_j(\boldsymbol{r}) \rangle\rangle, \tag{1.7}$$

where $v_i(\boldsymbol{r}) \equiv u_i(\boldsymbol{x}+\boldsymbol{r},t) - u_i(\boldsymbol{x},t)$. By projecting the velocity difference either onto the direction of the distance vector $\boldsymbol{r}$ or onto the directions perpendicular to it, this tensor can be decomposed into its longitudinal and transversal parts, respectively.

For a long time the scaling properties of turbulence have been studied mainly in terms of the longitudinal velocity structure function [9, 12]. This was mainly because these structure functions are easier to access in experiments. However, evidence has been found, that the transversal structure functions scale differently [13–17]. Instead of decomposing it into its longitudinal and transversal components, Arad et al. [18] suggested choosing a different decomposition. Namely, the structure function tensor is decomposed into its SO(3) invariants, reflecting the rotational symmetry of the Navier-Stokes equation:

$$D_{ik}(\boldsymbol{r}) = \sum_{jmq} d_{jmq}(r) B_{ik}^{jmq}(\hat{\boldsymbol{r}}), \tag{1.8}$$

with basis tensors $B_{ik}^{jmq}(\hat{\boldsymbol{r}})$, depending on the unit vector $\hat{\boldsymbol{r}}$, and amplitudes $d_{jmq}(r)$. In this decomposition, isotropic and anisotropic parts of the structure function can be easily distinguished, as all isotropic contributions are collected in the $j = 0$ sector. Within the decomposition into longitudinal and transversal parts, on the other hand, isotropic and anisotropic contributions are mixed, and therefore, those structure functions may not show a clean scaling behavior at all. Within the variable-range mean-field theory we calculate the scaling behavior of the amplitudes $d_{jmq}(r)$. For the isotropic part we find Kolmogorov scaling $d_{j=0} \propto r^{2/3}$, whereas the scaling of the anisotropic parts is found to depend on the type of the external stirring force.

In the Chapters 3 and 4 we come back to homogeneous and isotropic turbulence, but we assume a **time dependent** driving of the flow. Time dependent driving forces are ubiquitous: be it the periodic heating of the sun driving the atmosphere of the earth or the heart beats which drive the blood flow through the arteries. Many other biological and atmospherical as well as engineering flows are driven by time dependent driving forces which are often periodic. Here, we study a fully developed turbulent flow driven by a modulated energy input rate or a modulated force. Both cases are similar, but not exactly equal. The response of the flow can be studied in terms of the second order structure function on the outer length scale L, $D(L,t) = \langle\langle v(L,t)^2 \rangle\rangle$, the Reynolds number $Re(t) = u_{1,rms}L/\nu$, or the total energy of the system $E(t) = \frac{3}{2}u_{1,rms}^2$.

The picture of the energy cascade suggests that the energy, which is fed into the system on large scales and is dissipated mainly on small scales, stays some time in the system while it is traveling down the cascade. On average (in time), of course the total dissipation rate ϵ equals the energy input rate. On the other hand, at a certain time t the energy dissipation rate $\epsilon(t)$ will depend on the amount of energy put into the system at an earlier time $t - \tau$, where τ is the average time the energy needs to travel down the energy cascade. Using this picture, the response of the system can be calculated within the variable-range mean-field theory. This is shown in Chapter 3 (see also *Response maxima in modulated turbulence* [19]). The finite energy cascade time scale τ plays a crucial role in this theory. For driving frequencies larger than

$\simeq 1/\tau$ the system can follow less and less the oscillations of the driving. Furthermore, the time scale τ gives rise to maxima and minima of the response amplitude at frequencies connected with this time scale.

As mentioned before, turbulent fluctuations are not included in the mean-field theory. In real turbulence, on the other hand, the cascade time scale will be fluctuating. This may have an influence on the response maxima, i.e., they may be washed out. Therefore, in Chapter 4 we study modulated turbulence within two numerical models of turbulence, namely the GOY shell model[1] [20–27] and the reduced wave vector set approximation (REWA) [28–30] of the Navier-Stokes equation, in order to account for the effect of turbulent fluctuations (see also *Numerical simulations of modulated turbulence* [31]). The mean trend of the response function as predicted by the mean-field theory can be reproduced. Furthermore, we find the main response maximum in the simulations of both models, although it is weakened and broadened due to the fluctuations.

In Chapter 5 (see also *How snapping shrimp snap: Through cavitating bubbles* [32, 33]) an example from nature of nonideal turbulent flow is presented. The snapping shrimp produces a loud snapping sound while rapidly closing its snapper claw. These animals emit a high velocity water jet during the claw closure. The snapping is used for intra-specific communication as well as to stun or even kill prey animals [34–36]. The snapping sound, however, was commonly attributed to the mechanical noise from the two claw surfaces hitting each other. In experiments [32, 33] it was found that a cavitation bubble is growing due to the pressure drop produced by the high velocity of the jet. Subsequently, this bubble collapses violently. It was demonstrated that rather than mechanical noise, it it this collapse of a cavitation bubble which is the origin of the loud snapping sound. Here, we not only have a inhomogeneous, anisotropic and time dependent turbulent water jet, but, in addition, there is a cavitation bubble filled with a (compressible) gas, which is mostly water vapor. A simplified model for the dynamics of the bubble based on a Rayleigh-Plesset type equation is set up. The agreement between the model results and experimental data for the time dependence of the bubble radius as well as the emitted sound is surprisingly good as the model assumes several simplifications of the system.

The main results of our studies on nonideal turbulence will be summarized and discussed in Chapter 6.

---

[1] named after Gledzer, Ohkitani and Yamada

References

[1] L. D. Landau and E. M. Lifshitz, *Fluid Mechanics* (Pergamon Press, Oxford, 1987).

[2] S. B. Pope, *Turbulent Flows* (Cambridge University Press, Cambridge, 2000).

[3] L. F. Richardson, *Weather prediction by numerical process* (Cambridge University Press, Cambridge, 1922).

[4] A. N. Kolmogorov, CR. Acad. Sci. USSR. **30**, 299 (1941).

[5] A. Obukhov, CR. Acad. Sci. USSR **32**, 19 (1941).

[6] W. Heisenberg, Z. Phys. **124**, 628 (1948).

[7] C. F. von Weizsäcker, Z. Phys. **124**, 614 (1948).

[8] L. Onsager, Phys. Rev. **68**, 286 (1945).

[9] U. Frisch, *Turbulence* (Cambridge University Press, Cambridge, 1995).

[10] H. Effinger and S. Grossmann, Z. Phys. B **66**, 289 (1987).

[11] S. Grossmann, A. von der Heydt, and D. Lohse, J. Fluid Mech. **440**, 381 (2001).

[12] A. S. Monin and A. M. Yaglom, *Statistical Fluid Mechanics* (The MIT Press, Cambridge, Massachusetts, 1975).

[13] A. Noullez, G. Wallace, W. Lempert, R. B. Miles, and U. Frisch, J. Fluid Mech. **339**, 287 (1997).

[14] S. Grossmann, D. Lohse, and A. Reeh, Phys. Fluids **9**, 3817 (1997).

[15] B. Dhruva, Y. Tsuji, and K. R. Sreenivasan, Phys. Rev. E **56**, R4928 (1997).

[16] S. Chen, K. R. Sreenivasan, M. Nelkin, and N. Cao, Phys. Rev. Lett. **79**, 2253 (1997).

[17] W. van de Water and J. A. Herweijer, J. Fluid Mech. **387**, 3 (1999).

[18] I. Arad, V. L'vov, and I. Procaccia, Phys. Rev. E **59**, 6753 (1999).

[19] A. von der Heydt, S. Grossmann, and D. Lohse, Phys. Rev. E, in press (2003).

[20] E. B. Gledzer, Sov. Phys. Dokl. **18**, 216 (1973).

[21] M. Yamada and K. Ohkitani, J. Phys. Soc. Jpn. **56**, 4210 (1987).

[22] M. Yamada and K. Ohkitani, Prog. Theor. Phys. **79**, 1265 (1988).

[23] K. Ohkitani and M. Yamada, Prog. Theor. Phys. **81**, 329 (1989).

[24] M. H. Jensen, G. Paladin, and A. Vulpiani, Phys. Rev. A **43**, 798 (1991).

[25] L. Kadanoff, D. Lohse, J. Wang, and R. Benzi, Phys. Fluids **7**, 617 (1995).

[26] T. Bohr, M. H. Jensen, G. Paladin, and A. Vulpiani, *Dynamical Systems Approach to Turbulence* (Cambridge University Press, Cambridge, 1998).

[27] L. Biferale, Ann. Rev. Fluid Mech. **35**, 441 (2003).

[28] J. Eggers and S. Grossmann, Phys. Fluids A **3**, 1958 (1991).

[29] S. Grossmann and D. Lohse, Z. Phys. B **89**, 11 (1992).

[30] S. Grossmann and D. Lohse, Phys. Fluids **6**, 611 (1994).

[31] A. von der Heydt, S. Grossmann, and D. Lohse, *Numerical simulations of modulated turbulence*, Preprint, submitted to Phys. Rev. E (2003).

[32] M. Versluis, B. Schmitz, A. von der Heydt, and D. Lohse, Science **289**, 2114 (2000).

[33] M. Versluis, A. von der Heydt, D. Lohse, and B. Schmitz, Phys. Fluids **13**, S13 (2001).

[34] G. MacGinitie and N. MacGinitie, *Natural history of marine animals* (McGraw Hill, New York, 1949).

[35] J. Herberholz and B. Schmitz, Biol. Bull. **195**, 156 (1998).

[36] J. Herberholz and B. Schmitz, J. Comp. Physiol. A **185**, 41 (1999).

Chapter 2

Scaling Exponents in Weakly Anisotropic Turbulence from the Navier-Stokes Equation *

The second order velocity structure tensor of weakly anisotropic strong turbulence is decomposed into its SO(3) invariant amplitudes $d_j(r)$. Their scaling is derived within a scaling approximation of a variable-scale mean-field theory of the Navier-Stokes equation. In the isotropic sector $j = 0$ Kolmogorov scaling $d_0(r) \propto r^{2/3}$ is recovered. The scaling of the higher j-amplitudes (j even) depends on the type of the external forcing that maintains the turbulent flow. We consider two options: (i) For an analytic forcing and for decreasing energy input into the sectors with increasing j, the scaling of the higher sectors $j > 0$ can become as steep as $d_j(r) \propto r^{j+2/3}$. (ii) For a non-analytic forcing we obtain $d_j(r) \propto r^{4/3}$ for *all* nonzero and even j.

2.1 Introduction

In the last few decades scaling in fully developed turbulence was mainly analyzed in terms of the longitudinal velocity structure functions [1, 2]. Meanwhile experimental and numerical evidence has accumulated that at least for finite Reynolds numbers the transversal structure functions scale differently [3–7]. Two questions immediately arise: (i) What is the proper decomposition of the velocity structure tensor into

---

[*] See also S. Grossmann, A. von der Heydt, and D. Lohse, *Scaling exponents in weakly anisotropic turbulence from the Navier-Stokes equation*, J. Fluid Mech. **440**, 381 (2001)

invariant amplitudes, and (ii) what is the origin of their different scalings?

In addressing the first question, Arad et al. [8] suggested to decompose the second-order velocity structure tensor into the amplitudes $d_{jmq}(r)$ of the irreducible SO(3) representation,

$$D_{ik}(\boldsymbol{r}) = \langle\langle v_i(\boldsymbol{r},t) v_k(\boldsymbol{r},t)\rangle\rangle = \sum_{jmq} d_{jmq}(r) B_{ik}^{jmq}(\hat{\boldsymbol{r}}), \tag{2.1}$$

reflecting the rotational symmetry of the Navier-Stokes equation. Here, $v_i(\boldsymbol{r},t) = u_i(\boldsymbol{x}+\boldsymbol{r},t) - u_i(\boldsymbol{x},t)$ is the velocity difference, the brackets $\langle\langle ... \rangle\rangle$ denote the ensemble average and, as in reference [8], the tensors $B_{ik}^{jmq}(\hat{\boldsymbol{r}})$ are combinations of the spherical harmonics $Y_{jm}(\hat{\boldsymbol{r}})$ and operations like $\partial_{r_i},\ r_k,\ \delta_{ik}$, the index q labels the different types of such combinations, and $\hat{\boldsymbol{r}}$ denotes the unit vector in the direction of $\boldsymbol{r}$, $\hat{\boldsymbol{r}} = \frac{\boldsymbol{r}}{r}$. Nonzero values of j contribute to D_{ik} if the turbulence is not isotropic.

In the references [9–13] the scaling exponents of the amplitudes $d_j(r)$ were extracted from experimental as well as numerical data. For $j = 0$ a scaling exponent close to the Kolmogorov value $2/3$ was recovered, but for $j = 2$ values close to $4/3$ were found. This scaling exponent corresponds to a power spectrum $\sim k^{-7/3}$, a behavior first suggested for shear flow by Lumley [14] through a dimensional argument. Experimental evidence for it was found by Wyngaard and Cote [15] and, later, also by Saddoughi and Veeravalli [16], among others. For higher $j > 2$ Biferale and Toschi [17] have found even larger scaling exponents from the analysis of numerical data, namely 1.67–1.7 for $j = 4$ and 3.3–3.4 for $j = 6$.

Here we aim at analytically *calculating* the mean-field part of the scaling exponents of the j amplitudes from the Navier-Stokes equation for weakly anisotropic, homogeneous turbulence. We employ the variable-scale mean-field theory of Effinger and Grossmann [18], i.e., we disregard intermittency corrections.

2.2 The Effinger-Grossmann mean-field theory for the weakly anisotropic case

The main idea in reference [18] is to decompose the velocity field into a smooth part $u_i^{(r)}$, defined as spatial average over a sphere with variable radius r and therefore containing only scales larger than r, and a strongly varying part $\tilde{u}_i^{(r)}$, to which the scales smaller than r contribute. Within the Effinger-Grossmann theory, not only the K41 r-scaling exponent $2/3$ of the structure function can be analytically calculated from the Navier-Stokes equation, but also the Kolmogorov constant $b = 6.3$. As we now assume (weak) anisotropy of the flow, we introduce an average which reflects its scale r and, in addition, the direction of the averaging. Therefore, for each component, we choose an average over a line in $\hat{\boldsymbol{r}}$-direction with the length $2r$,

$$u_i^{(\boldsymbol{r})}(\boldsymbol{x},t) = \frac{1}{2r}\int_{-r}^{r} u_i(\boldsymbol{x}+y\hat{\boldsymbol{r}},t)dy \equiv \langle u_i(\boldsymbol{x}+y\hat{\boldsymbol{r}},t)\rangle_y^{(\boldsymbol{r})}. \tag{2.2}$$

Correspondingly, $\tilde{u}_i^{(\boldsymbol{r})}(\boldsymbol{x},t) = u_i(\boldsymbol{x},t) - u_i^{(\boldsymbol{r})}(\boldsymbol{x},t)$. The upper index $\boldsymbol{r}$ says, that these averages not only depend on the scale r, but also on the direction $\hat{\boldsymbol{r}}$ of averaging, thus on the full vector $\boldsymbol{r}$. The lower index y indicates the averaged variable. As in the original spherical averaging case there is a close relation between the second order moments of $u_i^{(\boldsymbol{r})}$ and the structure tensor $D_{ik}(\boldsymbol{r})$:

$$\langle\!\langle u_i^{(\boldsymbol{r})} u_k^{(\boldsymbol{r})}\rangle\!\rangle = \langle\!\langle u_i u_k\rangle\!\rangle - \frac{1}{2}\langle\langle D_{ik}(\boldsymbol{y}_1+\boldsymbol{y}_2)\rangle_{y_1}^{(\boldsymbol{r})}\rangle_{y_2}^{(\boldsymbol{r})}. \tag{2.3}$$

This relation is crucial for the method. For simplicity we use the abbreviation $\boldsymbol{y} = y\hat{\boldsymbol{r}}$. In the above double average $\boldsymbol{y}_1$ is thus parallel to $\boldsymbol{y}_2$.

Eliminating the pressure p renders a nonlocal term involving the Green function $G(x)$. Inserting the velocity decomposition into the Navier-Stokes equation and averaging, we obtain an equation of motion for the large scale (*“super-scale”*) velocity:

$$\begin{aligned}
\partial_t u_i^{(\boldsymbol{r})}(\boldsymbol{x},t) &= -u_j^{(\boldsymbol{r})}(\boldsymbol{x},t)\partial_{x_j} u_i^{(\boldsymbol{r})}(\boldsymbol{x},t) - \langle \tilde{u}_j^{(\boldsymbol{r})}(\boldsymbol{x}+y\hat{\boldsymbol{r}})\partial_{x_j}\tilde{u}_i^{(\boldsymbol{r})}(\boldsymbol{x}+y\hat{\boldsymbol{r}})\rangle_y^{(\boldsymbol{r})} \\
&\quad +\nu\Delta_x u_i^{(\boldsymbol{r})}(\boldsymbol{x},t) + f_i^{(\boldsymbol{r})}(\boldsymbol{x},t) \\
&\quad +\int d^3x' G(x')\partial_{x_i'}\{u_{k|l}^{(\boldsymbol{r})}(\boldsymbol{x}+\boldsymbol{x}',t)u_{l|k}^{(\boldsymbol{r})}(\boldsymbol{x}+\boldsymbol{x}',t) \\
&\qquad +\langle \tilde{u}_{k|l}^{(\boldsymbol{r})}(\boldsymbol{x}+\boldsymbol{x}'+y\hat{\boldsymbol{r}},t)\tilde{u}_{l|k}^{(\boldsymbol{r})}(\boldsymbol{x}+\boldsymbol{x}'+y\hat{\boldsymbol{r}},t)\rangle_y^{(\boldsymbol{r})}\}.
\end{aligned} \tag{2.4}$$

We use the abbreviation: $u_{i|k}(\boldsymbol{x},t) := \partial_{x_k} u_i(\boldsymbol{x},t)$, etc. Δ_x denotes the Laplacian with respect to $\boldsymbol{x}$. ν is the kinematic viscosity and f_i an external forcing maintaining the turbulent flow. In reference [18] isotropic forcing is considered. Here, by proper choice of f_i we explicitly introduce anisotropy. It implies an anisotropic energy input whose characteristic details will be discussed later. Subtracting (2.4) from the Navier-Stokes equation gives an equation for the *“sub-scale”* velocity $\tilde{u}_i^{(\boldsymbol{r})}$. Its formal solution can be found by time integrating along a Lagrangian path $\boldsymbol{x}(t';\boldsymbol{z},t)$ of a fluid particle which at time $t'=t$ is at the position $\boldsymbol{x}=\boldsymbol{z}$. Also, from Eq. (2.4) we can derive an energy balance equation for the super-scales.

The central approximation of the mean-field theory of reference [18] is that the small scale flow is statistically independent of the smooth large scale one. Therefore, in higher order moments we factorize the $u^{(\boldsymbol{r})}$ from the $\tilde{u}^{(\boldsymbol{r})}$, e.g.

$$\langle\!\langle \tilde{u}^{(\boldsymbol{r})}\tilde{u}^{(\boldsymbol{r})}u^{(\boldsymbol{r})}u^{(\boldsymbol{r})}\rangle\!\rangle \simeq \langle\!\langle \tilde{u}^{(\boldsymbol{r})}\tilde{u}^{(\boldsymbol{r})}\rangle\!\rangle\langle\!\langle u^{(\boldsymbol{r})}u^{(\boldsymbol{r})}\rangle\!\rangle. \tag{2.5}$$

Physically this means that the large scales feel the small ones as a kind of eddy viscosity. Note again that this factorization excludes intermittency effects. Another assumption is that in the time integration along a Lagrangian path of a fluid particle the slow t'-dependence of the super-scales $u^{(\boldsymbol{r})}$ is neglected since the sub-scales $\tilde{u}^{(\boldsymbol{r})}$ fluctuate on a much shorter time scale.

The resulting contributions to the energy balance can be expressed in terms of the structure function tensor $D_{ik}(\boldsymbol{r})$. To simplify the expressions we introduce the second order moment of the super-scale velocity, $R_{ik}^{(\boldsymbol{r})}(\boldsymbol{r}')$, and the time integrated correlation function of the sub-scale eddies, $N_{ik}^{(\boldsymbol{r})}(\boldsymbol{r}')$. Both can be expressed in terms of the structure function tensor:

$$\begin{aligned} R_{ik}^{(\boldsymbol{r})}(\boldsymbol{r}') &\equiv \langle\langle\!\langle u_i^{(\boldsymbol{r})}(\boldsymbol{x},t)u_k^{(\boldsymbol{r})}(\boldsymbol{x}+\boldsymbol{y}+\boldsymbol{r}',t)\rangle\!\rangle\rangle_y^{(\boldsymbol{r})} \qquad (2.6) \\ &= \langle\!\langle u_i u_k\rangle\!\rangle - \frac{1}{2}\langle\langle\langle D_{ik}(\boldsymbol{r}'+\boldsymbol{y}_1+\boldsymbol{y}_2+\boldsymbol{y}_3)\rangle_{y_1}^{(\boldsymbol{r})}\rangle_{y_2}^{(\boldsymbol{r})}\rangle_{y_3}^{(\boldsymbol{r})}, \\ N_{ik}^{(\boldsymbol{r})}(\boldsymbol{r}') &\equiv \int_{-\infty}^{t} dt'\langle\!\langle \tilde{u}_i^{(\boldsymbol{r})}(\boldsymbol{z},t)\tilde{u}_k^{(\boldsymbol{r})}(\boldsymbol{x}(t';\boldsymbol{z},t)+\boldsymbol{r}',t')\rangle\!\rangle. \qquad (2.7) \end{aligned}$$

$N_{ik}^{(\boldsymbol{r})}$ probes the (Lagrangian) dynamics and can be considered as an eddy transport coefficient for the super-scale flow. To obtain a closed set of equations we express $N_{ik}^{(\boldsymbol{r})}$ in terms of equal time and therefore stationary *static* objects like the structure tensor $D_{ik}(\boldsymbol{r})$. This is achieved by continued fraction projector expansion [19, 20]. With the static sub-scale correlation

$$\tilde{C}_{ik}^{(\boldsymbol{r})}(\boldsymbol{x}') \equiv \langle\!\langle \tilde{u}_i^{(\boldsymbol{r})}(\boldsymbol{x},t)\tilde{u}_k^{(\boldsymbol{r})}(\boldsymbol{x}+\boldsymbol{x}',t)\rangle\!\rangle \qquad (2.8)$$

and the frequency matrix

$$\tilde{\Gamma}_{ik}^{(\boldsymbol{r})}(\boldsymbol{x}') \equiv -\langle\!\langle \tilde{u}_i^{(\boldsymbol{r})}(\boldsymbol{z},t)d_{t'}\tilde{u}_k^{(\boldsymbol{r})}(\boldsymbol{x}(t';\boldsymbol{z},t)+\boldsymbol{x}',t')\rangle\!\rangle|_{t'=t} \qquad (2.9)$$

we can write $N_{ik}^{(\boldsymbol{r})}$ in 1-pole approximation as:

$$N_{ik}^{(\boldsymbol{r})}(\boldsymbol{x}') = \tilde{C}_{ij}^{(\boldsymbol{r})}(\boldsymbol{x}')(\tilde{\Gamma}^{(\boldsymbol{r})}(\boldsymbol{x}'))_{jl}^{-1}\tilde{C}_{lk}^{(\boldsymbol{r})}(\boldsymbol{x}').$$

The tensor $\tilde{C}$ and the frequency matrix $\tilde{\Gamma}$ can be expressed in terms of the structure function tensor

$$\begin{aligned} \tilde{C}_{ik}^{(\boldsymbol{r})}(\boldsymbol{x}') &= -\frac{1}{2}\langle\langle D_{ik}(\boldsymbol{x}'+\boldsymbol{y}_1+\boldsymbol{y}_2)\rangle_{y_1}^{(\boldsymbol{r})}\rangle_{y_2}^{(\boldsymbol{r})} + \langle D_{ik}(\boldsymbol{x}'+\boldsymbol{y})\rangle_y^{(\boldsymbol{r})} - \frac{1}{2}D_{ik}(\boldsymbol{x}'), \\ \tilde{\Gamma}_{ik}^{(\boldsymbol{r})}(\boldsymbol{x}') &= \frac{2}{3}\epsilon\delta_{ik} - 2\nu\langle\Delta_y D_{ik}(\boldsymbol{y})\rangle_y^{(\boldsymbol{r})} \\ &\quad +\nu\langle\langle\Delta_{y_1}D_{ik}(\boldsymbol{y}_1+\boldsymbol{y}_2)\rangle_{y_1}^{(\boldsymbol{r})}\rangle_{y_2}^{(\boldsymbol{r})} + \nu\Delta_{x'}\tilde{C}_{ik}^{(\boldsymbol{r})}(\boldsymbol{x}'). \end{aligned}$$

For more details compare with the case of isotropic turbulence in reference [18]. In a general anisotropic case the dissipation matrix elements $\nu\langle\!\langle u_{i|j}^2\rangle\!\rangle$ might be different for different i, j. Here, in the weakly anisotropic case, we assume that the anisotropy corrections are small on the scales where dissipation takes place. Therefore we insert one total dissipation rate per unit mass $\epsilon = \nu \langle\langle u_{i|j} u_{i|j} \rangle\rangle$ (summation implied).

The super-scale energy balance equation consists of three contributions for the losses. $E_d(\boldsymbol{r})$ describes the direct viscous energy dissipation by the super-scale eddies. The other two, $E_t(\boldsymbol{r})$, consisting of a local and a nonlocal part, account for the energy transfer from the large to the small scales. These losses are balanced by the energy input rate $E_{in}(\boldsymbol{r})$ caused by the external forcing:

$$E_d(\boldsymbol{r}) + E_{t,lo}(\boldsymbol{r}) + E_{t,nolo}(\boldsymbol{r}) = E_{in}(\boldsymbol{r}). \tag{2.10}$$

As in [18] the three different contributions can be written:

$$\begin{aligned}
E_d(\boldsymbol{r}) &= \frac{1}{2}\nu \langle\langle \Delta_{y_1} D_{ii}(\boldsymbol{y}_1 + \boldsymbol{y}_2)\rangle_{y_1}^{(\boldsymbol{r})}\rangle_{y_2}^{(\boldsymbol{r})}, && (2.11)\\
E_{t,lo}(\boldsymbol{r}) &= -\frac{1}{2} N_{jk}^{(\boldsymbol{r})}(\boldsymbol{x}' = 0)\partial_{x'_j}\partial_{x'_k} R_{ii}^{(\boldsymbol{r})}(\boldsymbol{x}')|_{\boldsymbol{x}'=0}, && (2.12)\\
E_{t,nolo}(\boldsymbol{r}) &= -\int d^3x' G(x')\partial_{x'_i}\partial_{x'_j}\left\{\partial_{x'_j} N_{lk}^{(\boldsymbol{r})}(\boldsymbol{x}') - \partial_{x'_l} N_{jk}^{(\boldsymbol{r})}(\boldsymbol{x}')\right\}\partial_{x'_k} R_{il}^{(\boldsymbol{r})}(\boldsymbol{x}') \\
&\quad + \int d^3x' G(x')\Delta_{x'}\Big(\partial_{x'_i} N_{lk}^{(\boldsymbol{r})}(\boldsymbol{x}')\Big)\,\partial_{x'_k} R_{il}^{(\boldsymbol{r})}(\boldsymbol{x}'). && (2.13)
\end{aligned}$$

The energy input rate is given by

$$E_{in}(\boldsymbol{r}) = \langle\langle u_i^{(\boldsymbol{r})} f_i^{(\boldsymbol{r})} \rangle\rangle. \tag{2.14}$$

Note that in contrast to the isotropic case all terms in the energy balance (2.10) now depend on the vector $\boldsymbol{r}$, not merely on its absolute value, the scale r.

Eq. (2.10) together with Eqs. (2.11) – (2.14) constitute a set of integro-differential equations for the tensor $D_{ik}(\boldsymbol{r})$. Now, anisotropy is assumed to be small. More precisely, in a SO(3)-decomposition of $D_{ik}(\boldsymbol{r})$ the j-amplitudes are assumed to decrease in magnitude for higher angular wave number j. Then (2.10) can be solved order by order in j, obtaining the structure function amplitudes $d_j(r)$. They will not be universal but depend on the anisotropy of the forcing. However, what we may hope is that the *scaling* of the individual j-amplitudes *is universal*. To analyze this, it is sufficient to focus on the scaling behavior of the various contributions in (2.10).

Scale wise, multiple spatial averages can be reduced to first order ones, e.g. $E_d(\boldsymbol{r}) \sim \frac{\nu}{2} < \Delta_y D_{ii}(\boldsymbol{y}) >_y^{(\boldsymbol{r})}$, and local and nonlocal energy transfer rates scale with the same exponent. Here and in the following "$\sim$" has the meaning of "scale wise equal". Thus the energy balance equation scale wise simplifies to

$$E_{in}(\boldsymbol{r}) \sim \langle \frac{\nu}{2}\Delta_y D_{ii}(\boldsymbol{y})\rangle_y^{(\boldsymbol{r})} + \langle \frac{\alpha}{\epsilon} D_{jl}(\boldsymbol{r}) D_{lk}(\boldsymbol{r}) \partial_{y_j}\partial_{y_k} D_{ii}(\boldsymbol{y})\rangle_y^{(\boldsymbol{r})}. \tag{2.15}$$

Here, ϵ is the mean energy dissipation rate per unit mass, and the constant α takes into account the relative weight of the transport terms, E_t in (2.10). Scale wise this equation can be simplified even further:

$$E_{in}(\boldsymbol{r}) \sim \frac{1}{2}\left(\nu + \frac{\beta}{\epsilon}D(\boldsymbol{r})D(\boldsymbol{r})\right)\Delta D(\boldsymbol{r}), \tag{2.16}$$

where β takes into account the missing constants of proportionality. DD and ΔD stand for the tensorial products of two structure function tensors and of a 2nd order spatial derivative of the structure function tensor, respectively.

2.3 SO(3)-decomposition

Taking into account the full tensorial character of $D_{ik}(\boldsymbol{r})$ (Eq. (2.1)) complicates the resulting equation. Therefore, for simplicity, we assume that the r-scaling behavior remains the same. As we are interested at present in the scaling exponents only, we disregard the tensorial character of the structure function (i.e., drop the index q of $d_{jmq}(r)$) and expand into spherical harmonics:

$$\begin{aligned} D(\boldsymbol{r}) &\simeq d_{00}(r)Y_{00} + \sum_m d_{2m}(r)Y_{2m}(\hat{\boldsymbol{r}}) + \sum_m d_{4m}(r)Y_{4m}(\hat{\boldsymbol{r}}) + ... \\ &\sim \sum_j d_j(r)\sum_m Y_{jm}(\hat{\boldsymbol{r}}). \end{aligned} \tag{2.17}$$

Here, we assume that the scaling behavior of $d_{jm}(r)$ is - for fixed j - the same for all m, and therefore simply write $d_j(r)$. We analogously expand the energy input rate into spherical harmonics:

$$E_{in}(\boldsymbol{r}) = \sum_{j,m} e_{jm}(r)Y_{jm}(\hat{\boldsymbol{r}}) \sim \sum_j e_j(r)\sum_m Y_{jm}(\hat{\boldsymbol{r}}), \tag{2.18}$$

where

$$e_{jm}(r) = \int \mathrm{d}(\cos\theta)\mathrm{d}\varphi\, Y^*_{jm}(\hat{\boldsymbol{r}})E_{in}(\boldsymbol{r}). \tag{2.19}$$

Then we insert the SO(3)-decomposition (2.17) of the structure function and the corresponding expansion (2.18) of the energy input rate into Eq. (2.16).

From now on we only focus on the inertial subrange (ISR), $\eta \ll r \ll L$, where η is the Kolmogorov length, in which the second term on the right hand side of Eq. (2.16) dominates. Thus the energy balance equation reads:

$$\sum_j e_j(r)\sum_m Y_{jm}(\hat{\boldsymbol{r}}) \sim \frac{\beta}{r^2}\Big(\sum_j d_j(r)\sum_m Y_{jm}(\hat{\boldsymbol{r}})\Big)^3. \tag{2.20}$$

Projecting Eq. (2.20) on the different j-sectors and taking into account only the first three j's ($j = 0,\ 2,\ 4$) yields three nonlinear equations for $d_0(r)$, $d_2(r)$ and $d_4(r)$:

$$\begin{aligned}
e_0(r)r^2 &\sim \beta[A_{000,0}(d_0(r))^3 + 3A_{022,0}d_0(r)(d_2(r))^2 + 3A_{044,0}d_0(r)(d_4(r))^2 \\
&\quad +A_{222,0}(d_2(r))^3 + 3A_{224,0}(d_2(r))^2d_4(r) + 3A_{244,0}d_2(r)(d_4(r))^2 \\
&\quad +A_{444,0}(d_4(r))^3], \qquad \text{(2.21.a)} \\
e_2(r)r^2 &\sim \beta[3A_{002,2}(d_0(r))^2d_2(r) + 3A_{022,2}d_0(r)(d_2(r))^2 \\
&\quad +3A_{044,2}d_0(r)(d_4(r))^2 + 6A_{024,2}d_0(r)d_2(r)d_4(r) \\
&\quad +A_{222,2}(d_2(r))^3 + 3A_{224,2}(d_2(r))^2d_4(r) \\
&\quad +3A_{244,2}d_2(r)(d_4(r))^2 + A_{444,2}(d_4(r))^3], \qquad \text{(2.21.b)} \\
e_4(r)r^2 &\sim \beta[3A_{004,4}(d_0(r))^2d_4(r) + 3A_{022,4}d_0(r)(d_2(r))^2 \\
&\quad +3A_{044,4}d_0(r)(d_4(r))^2 + 6A_{024,4}d_0(r)d_2(r)d_4(r) \\
&\quad +A_{222,4}(d_2(r))^3 + 3A_{224,4}(d_2(r))^2d_4(r) \\
&\quad +3A_{244,4}d_2(r)(d_4(r))^2 + A_{444,2}(d_4(r))^3]. \qquad \text{(2.21.c)}
\end{aligned}$$

Here, $A_{j_1j_2j_3,j_4} = \sum_{m_1,m_2,m_3,m_4} \int \mathrm{d}(\cos\theta)\mathrm{d}\varphi\ Y^*_{j_4m_4}Y_{j_1m_1}Y_{j_2m_2}Y_{j_3m_3}$. The $A_{j_1j_2j_3,j_4}$ can have either sign.

To extract the scaling laws for the different $d_j(r)$, Eqs. (2.21.a-c) have to be solved. But before doing so, we have to specify the energy input rate $E_{in}(\boldsymbol{r})$, Eq. (2.14), which depends on the external forcing $f_i^{(\boldsymbol{r})}$.

2.4 Anisotropic forcing

In the isotropic and homogeneous case $E_{in}(\boldsymbol{r}) = E_{in}$ is a scale-independent constant, [18]. The reason is the following. While the super-scale velocity field $u_i^{(r)}$ contains all scales larger than r, the forcing $f_i^{(r)}$ has the outer scale L only. For each $r \leq L$ the complete forcing is included in the same and therefore r-independent way. Of course, $E_{in} = \epsilon$. In the present case, however, the forcing has to provide an anisotropic flow. As a consequence we shall find that $f_i^{(\boldsymbol{r})}$ has to depend on *all* scales r, implying that also the energy input rate will depend on all r.

We will discuss two different classes of anisotropic flows: a general analytic forcing and a non-analytic forcing. For both we can determine the scaling behavior with dimensional arguments.

2.4.1 Analytic forcing

Let us assume that the forcing $f_i(\boldsymbol{x}) \sim a_i\boldsymbol{k}\cdot\boldsymbol{r}\sin(\boldsymbol{k}\cdot\boldsymbol{x})$ and the velocity profile $u_i(\boldsymbol{x}) \sim b_i\boldsymbol{k}\cdot\boldsymbol{r}\sin(\boldsymbol{k}\cdot\boldsymbol{x})$ depend on one input wave number $\boldsymbol{k}$ only. They are analytic in the components of position $\boldsymbol{x}$ and the scale vector $\boldsymbol{r}$. To fulfill the incompressibility condition, $\partial_i f_i = 0$ and $\partial_i u_i = 0$, the vectors a_i and b_i must be chosen as $a_i k_i = b_i k_i = 0$. Then, applying the y-average defined in Eq. (2.2) yields $u_i^{(\boldsymbol{r})} \sim f_i^{(\boldsymbol{r})} \sim [\cos(\boldsymbol{k} \cdot (\boldsymbol{x} + \boldsymbol{r})) - \cos(\boldsymbol{k} \cdot (\boldsymbol{x} - \boldsymbol{r}))]$. Therefore

$$E_{in}(\boldsymbol{r}) \sim \langle\langle (\cos(\boldsymbol{k} \cdot (\boldsymbol{x} + \boldsymbol{r})) - \cos(\boldsymbol{k} \cdot (\boldsymbol{x} - \boldsymbol{r})))^2 \rangle\rangle = 1 - \cos(2kr\xi) \qquad (2.22)$$

with $\xi = \cos\theta$, the projection on the z-axis defined by $\hat{\boldsymbol{k}}$. A power series expansion of $E_{in}(\boldsymbol{r})$ in the variable $r\xi$ inserted into Eq. (2.19) implies (because of $\xi^n \perp Y_{jm}$ for all $n < j$) that $e_{jm} \sim r^j$ plus higher powers.

We now solve Eqs. (2.21.a-c) and extract the power laws for the different $d_j(r)$. Fig.2.1 shows the solutions of the Eqs. (2.21.a-c). In the upper graph (a) the isotropic part of the energy input e_0 is the largest one, and the anisotropy contributions are small corrections. In this case, over the whole calculated range $10^{-4} \leq r/L \leq 1$ the $d_j(r)$ scale as

$$d_j(r) \sim r^{j+2/3}. \qquad (2.23)$$

We can see this scaling behavior easily from Eqs. (2.21.a-c): Since $d_4 \ll d_2 \ll d_0$, the dominating term on the right hand side of Eq. (2.21.a) is $A_{000,0}(d_0)^3$. It is balanced by $e_0 r^2$. Therefore, $d_0 \sim r^{2/3}$. Then, in Eqs. (2.21.b,2.21.c) the leading terms $A_{002,2}(d_0)^2 d_2$ and $A_{004,4}(d_0)^2 d_4$ are balanced by $e_2 r^2 \sim r^4$ and $e_4 r^2 \sim r^6$, respectively. Therefore we expect $d_2 \sim r^{8/3}$ and $d_4 \sim r^{14/3}$. Though for $j = 0$ we recover the mean-field scaling of the isotropic amplitude of the structure function $d_0 \sim r^{2/3}$, as in [18], the result for the $j = 2$ sector is at variance with the experimental finding by Kurien et al. [12], who found a scaling exponent close to 4/3. If, on the other hand, we chose a strongly anisotropic energy input with $e_2 \gg e_0, e_4$ [1], then the r-scaling range with $d_j(r) \sim r^{j+2/3}$ becomes smaller, while at larger values of r a new scaling range $d_j \sim r^{4/3}$ with the *same* exponent 4/3 for *all* j emerges, see Fig.2.1(b). For $j = 2$ this finding is now consistent with the experimental observations by Kurien et al. [12]. However, it is inconsistent with the exponent $2/3$ to be expected for the $j = 0$ amplitude. – In summary, the analytic energy input does not seem to describe the experimental findings. We therefore now explore the option of non-analytic forcing.

2.4.2 Non-analytic forcing

We consider a shear flow with its shear in 3-direction. Then the three f-components are different. We decompose the velocity u_i and the forcing f_i into an isotropic (*iso*) and a (smaller) anisotropic (*an*) part: $u_i = u_i^{(iso)} + u_i^{(an)}$, $f_i = f_i^{(iso)} + f_i^{(an)}$. Then

---

[1] In this case the assumption of weak anisotropy of course breaks down.

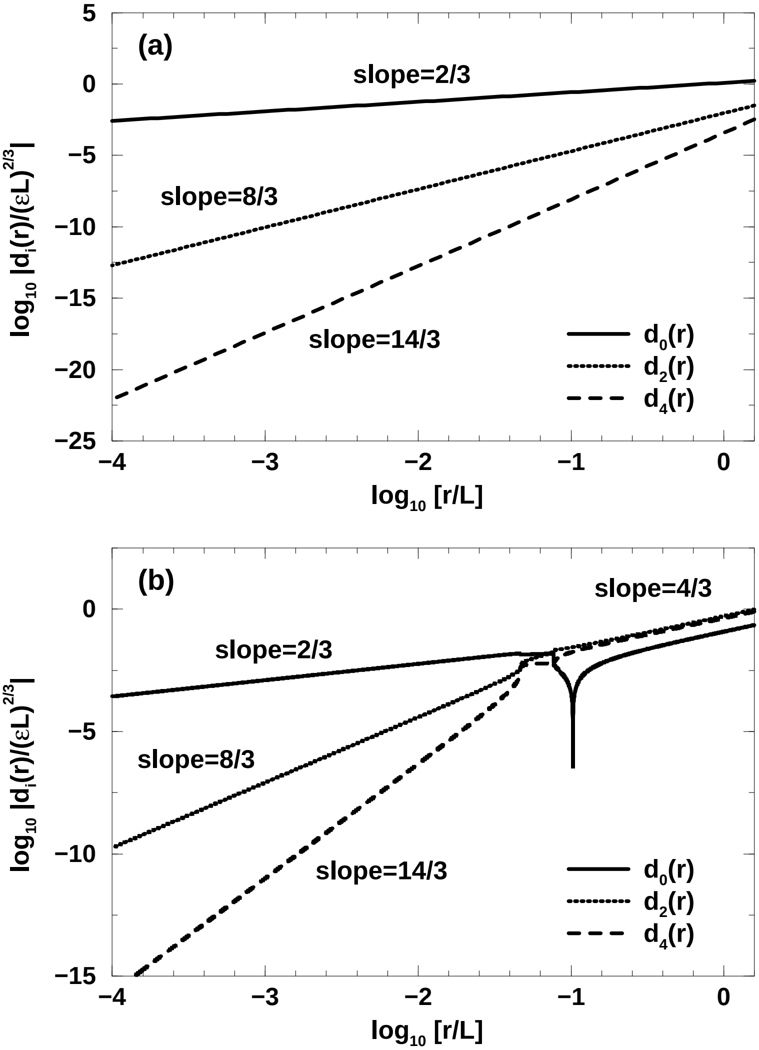

Figure 2.1: Scaling behavior of the amplitudes of the second order structure function $d_0(r)$, $d_2(r)$ and $d_4(r)$, for an analytic forcing. (*a*) Strong isotropic forcing together with weak anisotropy corrections, $e_0/\epsilon = 0.89, e_2/\epsilon = 0.1, e_4/\epsilon = 0.01$; (*b*) Case of strong anisotropic forcing: The first anisotropic sector $j = 2$ dominates the energy input, $e_0/\epsilon = 0.001, e_2/\epsilon = 0.989, e_4/\epsilon = 0.01$. This might already reach the limits of our assumptions regarding *weak* anisotropy. The dip of the d_0-curve originates from a change of sign of $d_0(r)$.

in first order of anisotropy

$$\begin{aligned}\langle\langle u_i^{(\boldsymbol{r})} f_i^{(\boldsymbol{r})}\rangle\rangle &\simeq \langle\langle u_i^{(\boldsymbol{r})} f_i^{(\boldsymbol{r})(iso)}\rangle\rangle + \langle\langle u_i^{(\boldsymbol{r})(iso)} f_i^{(\boldsymbol{r})(an)}\rangle\rangle \\ &= E_{in}^{(iso)} + E_{in}^{(an)}(\boldsymbol{r}). \end{aligned} \tag{2.24}$$

Repeating the arguments at the beginning of Section 2.4 for the isotropic case the first term on the right hand side does not depend on r, i.e., $E_{in}^{(iso)} \sim r^0$. Namely, since $f_i^{(\boldsymbol{r})(iso)}$ has scales of order L only, the smaller scales in the products with $u_i^{(\boldsymbol{r})(iso)}$ or $u_i^{(\boldsymbol{r})(an)}$ cannot contribute irrespective of their degree of isotropy. The second term, however, will depend on r and introduces anisotropy.

Let us determine $E_{in}^{(an)}(\boldsymbol{r})$ by scaling arguments. The flow profile in shear flow is generated by the boundary conditions: One plate is moving with velocity U, the other one is at rest. These boundary conditions have to be mimicked by the forcing f in an infinitely extending flow. The linear mean velocity profile $\frac{U}{L}z$ (and therefore also the corresponding f) has Fourier coefficients on all scales, $u^{(an)}(k) = \frac{U}{L^2}\int_{-L}^{L} dz\ ze^{ikz} = 2iU\left(\frac{\sin kL}{k^2L^2} - \frac{\cos kL}{kL}\right)$. In the case of large k, i.e., $k^{-1} \sim z \ll L$, the second term dominates. We therefore asymptotically find

$$u^{(an)}(k) \sim \frac{\cos kL}{kL} \sim \frac{1}{k} \sim z = r\cos\theta. \tag{2.25}$$

Incidentally, a parabolic velocity profile as in pipe flow, $\frac{U}{L^2}z^2$, gives the same asymptotic scaling, $u^{(an)}(k) \sim \frac{\sin kL}{kL} \sim \frac{1}{k} \sim z$ for large k.

Next, we determine the r-dependence of $f^{(an)}$. From the Navier-Stokes equation we have $\frac{\partial u}{\partial t} = ... + f$. Therefore, the dimension and r-scaling of f must correspond to that of u/τ, where τ is eddy turnover time of eddies of scale r. In the isotropic case the turnover time τ scales like $\tau(r) \sim \frac{r}{u(r)} \sim \frac{r}{r^{1/3}} \sim r^{2/3}$. We use the r-dependence of the anisotropic velocity field $u^{(an)}(r)$ together with that of the isotropic turnover time $\tau(r)$ to estimate the scaling of the anisotropic forcing $f^{(an)}$ in first order. Since $u^{(an)}$ behaves as $u^{(an)} \sim r\cos\theta$ according to Eq. (2.25), we have $f^{(an)} \sim r\cos\theta/r^{2/3} \sim r^{1/3}\cos\theta$. Note that this anisotropic forcing scales as the isotropic velocity $u^{(iso)} \sim r^{1/3}$. Then both factors of $E_{in}^{(an)}(\boldsymbol{r})$ in (2.24) not only contain *all* scales, but also the same power law exponents. We therefore find

$$E_{in}^{(an)}(\boldsymbol{r}) \sim r^{2/3}\cos\theta. \tag{2.26}$$

The forcing still has an additional factor $g(\theta,\varphi)$, which can be chosen such that the incompressibility constraint $\partial_i f_i = 0$ is fulfilled. Knowing now the scaling behavior of the energy input rate, we proceed to expand it into spherical harmonics (see Eq. (2.18)),

$$E_{in}(\boldsymbol{r}) = E_{in}^{(iso)} + r^{2/3}\tilde{E}_{in}^{(an)}(\hat{\boldsymbol{r}}) = \sum_{j,m} e_{jm}(r)Y_{jm}(\hat{\boldsymbol{r}}). \tag{2.27}$$

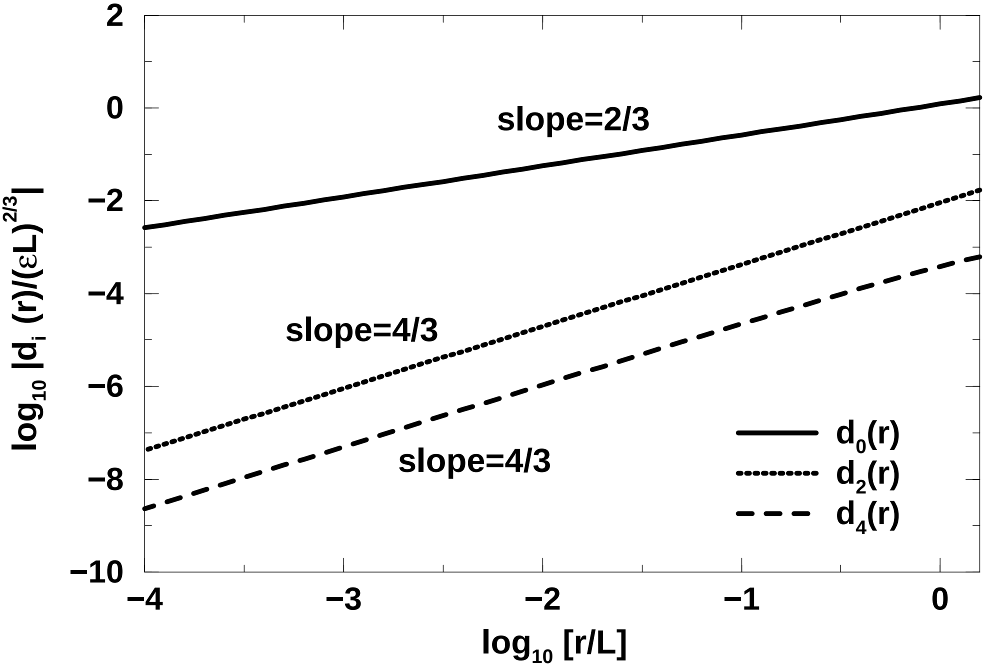

Figure 2.2: Scaling dependence of the amplitudes $d_0(r)$, $d_2(r)$ and $d_4(r)$ of the second order structure function, in case of a non-analytic forcing. The forcing is assumed as predominantly isotropic with small anisotropy corrections, $e_0/\epsilon = 0.89, e_2/\epsilon = 0.1, e_4/\epsilon = 0.01$.

Here, $e_{00}(r)$ equals $E_{in}^{(iso)}$, while for $j > 0$ the input rate amplitudes are $e_{jm}(r) = \int \mathrm{d}(\cos\theta)\mathrm{d}\varphi \; Y^*_{jm}(\hat{\boldsymbol{r}})E_{in}^{(an)}(\boldsymbol{r})$. Here the r- and ξ-dependencies are not coupled as $r\xi$, in contrast to the above treated analytic case. Thus there is no j-dependence of the leading r-power of the input amplitudes e_{jm}. The lowest j-value projection of the anisotropy correction $e_{jm}(r)$, in general $j = 2$, and all the higher ones, have the same power law, here according to (2.26) $\sim r^{2/3}$. The physics behind this decoupling of the r- and ξ-dependence is that a shear profile – in contrast to a single input wave number $\boldsymbol{k}$ – contains *all* wave numbers. The r-dependence is even non-analytic. Hence no expansion in $r\xi$ with only integer powers holds.

From Eqs. (2.21.a-c) and with $d_4 \ll d_2 \ll d_0$, we find that the leading terms in Eqs. (2.21.b,2.21.c) are $(d_0)^2 d_2 \sim r^{8/3}$ and $(d_0)^2 d_4 \sim r^{8/3}$. With $d_0 \sim r^{2/3}$ from Eq. (2.21.a) this leads to $d_2 \sim d_4 \sim r^{4/3}$. The solutions of Eqs. (2.21.a-c) for this non-analytic forcing describing shear flow are shown in Fig.2.2. For $j = 0$ we recover the isotropic scaling of the structure function $d_0(r) \sim r^{2/3}$. However, for *all* higher amplitudes we obtain

$$d_j(r) \sim r^{4/3} \tag{2.28}$$

in a wide range of r. We have shown only the case where the isotropic forcing dominates, $e_0 \gg e_2 \gg e_4$. If the anisotropic contributions to the energy input increase, the r-range of scaling behavior $d_0 \sim r^{2/3}$ and $d_j \sim r^{4/3}$ for all $j \geq 2$ is again shifted towards smaller r as in the case of analytic forcing.

As was argued by L'vov and Procaccia [21–23], in the exact resummation theory of Navier-Stokes turbulence no infrared (IR) divergence occurs if all j-factor scaling exponents ζ^j are bounded by 4/3. Otherwise IR-divergences cannot be excluded. Our results in the non-analytic case therefore exclude IR-divergences while in the previous analytic case they cannot be ruled out. Another possibility how these IR divergences may be controlled, in spite of second order moment exponents being larger than $4/3$, is by limiting the forcing to scales smaller than L, as recently shown in a Kraichnan model type dynamics for a vector field, see [24].

2.5 Summary

Within a variable-scale mean-field theory of the Navier-Stokes equation we have derived the scaling exponents of the different j amplitudes of the SO(3)-decomposition of the second order structure function for weakly anisotropic turbulent flow. The limitation of this approach is its mean-field character. Clearly, intermittency effects cannot be captured, but we consider those to be small for second order moments, to which the method is limited anyhow. In the isotropic sector $j = 0$ we recover the classical scaling behavior $\sim r^{2/3}$. The higher order contributions, i.e., the anisotropic parts of the flow field, can be calculated order by order in Y_{jm}. They yield, for all j, the same mean field scaling $r^{4/3}$ for a non-analytic forcing, whereas the scaling is $r^{j+2/3}$ for an analytic type of forcing. The non-analytic forcing might be more general, and therefore valid for a larger variety of anisotropic flows. Moreover, only the results for the non-analytic forcing are consistent with hitherto experimental measurements for the $j = 0$ and $j = 2$ amplitudes.

Acknowledgments: The work is part of the research program of FOM, which is financially supported by NWO. It was also supported by the German-Israeli Foundation (GIF) and by the European Union (EU) under contract HPRN-CT-2000-00162.

References

[1] A. S. Monin and A. M. Yaglom, *Statistical Fluid Mechanics* (The MIT Press, Cambridge, Massachusetts, 1975).

[2] U. Frisch, *Turbulence* (Cambridge University Press, Cambridge, 1995).

[3] A. Noullez, G. Wallace, W. Lempert, R. B. Miles, and U. Frisch, J. Fluid Mech. **339**, 287 (1997).

[4] S. Grossmann, D. Lohse, and A. Reeh, Phys. Fluids **9**, 3817 (1997).

[5] B. Dhruva, Y. Tsuji, and K. R. Sreenivasan, Phys. Rev. E **56**, R4928 (1997).

[6] S. Chen, K. R. Sreenivasan, M. Nelkin, and N. Cao, Phys. Rev. Lett. **79**, 2253 (1997).

[7] W. van de Water and J. A. Herweijer, J. Fluid Mech. **387**, 3 (1999).

[8] I. Arad, V. L'vov, and I. Procaccia, Phys. Rev. E **59**, 6753 (1999).

[9] I. Arad, B. Dhruva, S. Kurien, V. S. L'vov, I. Procaccia, and K. R. Sreenivasan, Phys. Rev. Lett. **81**, 5330 (1998).

[10] I. Arad, L. Biferale, I. Mazzitelli, and I. Procaccia, Phys. Rev. Lett. **82**, 5040 (1999).

[11] S. Kurien and K. R. Sreenivasan, Phys. Rev. E **62**, 2206 (2000).

[12] S. Kurien, V. S. L'vov, I. Procaccia, and K. R. Sreenivasan, Phys. Rev. E **61**, 407 (2000).

[13] S. Kurien and K. R. Sreenivasan, in *Les Houches Summer School Proceedings* (Springer and EDP-Sciences, ADDRESS, 2001), pp. 1–60.

[14] J. L. Lumley, Phys. Fluids **10**, 855 (1967).

[15] J. C. Wyngaard and O. R. Cote, Quart. J. R. Met. Soc. **98**, 590 (1972).

[16] S. G. Saddoughi and S. V. Veeravalli, J. Fluid Mech. **268**, 333 (1994).

[17] L. Biferale and F. Toschi, Phys. Rev.Lett. **86**, 4831 (2001).

[18] H. Effinger and S. Grossmann, Z. Phys. B **66**, 289 (1987).

[19] S. Grossmann and S. Thomae, Z. Phys. B **49**, 253 (1982).

[20] V. L. D. Daems, S.Grossmann and I. Procaccia, Phys. Rev. E **60**, 6656 (1999).

[21] V. S. L'vov and I. Procaccia, Phys. Rev. E **52**, 3840 (1995).

[22] V. S. L'vov and I. Procaccia, Phys. Rev. E **52**, 3858 (1995).

[23] V. S. L'vov and I. Procaccia, Phys. Rev. E **53**, 3468 (1996).

[24] I. Procaccia and I. Arad, Phys. Rev. E **63**, 056302 (2001).

Chapter 3

Response maxima in modulated turbulence [*]

Isotropic and homogeneous turbulence driven by an energy input modulated in time is studied within a variable-range mean-field theory. The response of the system, observed in the second order moment of the large-scale velocity difference $D(L,t) = \langle\langle(\boldsymbol{u}(x+L) - \boldsymbol{u}(x))^2\rangle\rangle \propto Re^2(t)$, is calculated for varying modulation frequencies ω and weak modulation amplitudes. For low frequencies the system follows the modulation of the driving with almost constant amplitude, whereas for higher driving frequencies the amplitude of the response decreases on average $\propto 1/\omega$. In addition, at certain frequencies the amplitude of the response either almost vanishes or is strongly enhanced. These frequencies are connected with the frequency scale of the energy cascade and multiples thereof.

3.1 Introduction

Many turbulent flows are characterized by time dependent forcing. E.g. the atmosphere of the earth is driven by the heating through the radiation from the sun, the blood flow in the arteries by the heart beats, etc. Also technical flows like the flow in the intake of a combustion engine are periodically forced. Another example are estuaries and adjacent coastal waters, where tidal straining leads to a periodic alternation of stratification and turbulent mixing of saline and fresh water [1]. This results in a periodically varying energy dissipation in the upper water layers with a 12 hour

---

[*] See also A. von der Heydt, S. Grossmann, and D. Lohse, *Response maxima in modulated turbulence*, Phys. Rev. E, in press (2003)

period.

The effect of a periodically increasing and decreasing energy input on turbulent flow depends on the frequency of the driving. This has been studied in reference [2] for a turbulent channel flow where the modulations of the input rate are generated near the wall. It was found that for high frequencies these oscillations are strongly damped with distance from the walls, such that they do not reach the inner part of the logarithmic boundary layer. Another example is Rayleigh-Benard convection: the interaction between the large scale circulating flow and the thermal plumes detaching from the upper and the lower boundary layers acts as a stochastically influenced time-dependent forcing on the turbulent flow in the inner region of the cell, as recently shown in [3–5]. In a von Kármán flow between two coaxial corotating disks [6, 7], the energy input rate is not constant if the disks are kept rotating at constant speed, but is periodically varying with a geometry-dependent frequency due to a coherent vortex precessing around the axis of rotation. In this case it was also shown, that the statistical properties of the turbulent fluctuations are affected by the time dependence of the mean flow. However, the averaged velocity power spectrum still shows Kolmogorov scaling over a broad frequency range, in addition to a low frequency peak corresponding to the oscillation of the mean flow.

These results raise the question how global quantities of a turbulent flow, like e.g. the total energy or the Reynolds number, respond to a time dependent energy input. This problem is the subject of the present chapter. From a more fundamental point of view, studying modulated turbulence will give more insight into the time scales in particular of the turbulent energy cascade.

In a previous study [8], the time evolution of the Reynolds number in a periodically kicked flow was analyzed. If the kicking strength and the kicking frequency are large enough, the Reynolds number grows and saturates on a level, which depends on the frequency and the kicking strength. The theoretical results from [8] have later been verified numerically in reference [9].

In this present chapter, we study a related type of forcing. Rather than periodically kicking the boundary conditions of homogeneous, isotropic turbulence as in [8], we force the flow through a time-dependent modulation of the energy input rate $e_{in}(t)$ on the outer length scale L,

$$e_{in}(t) = e_0(1 + e\sin(\omega t)). \tag{3.1}$$

This means that the flow is stationarily stirred ($\propto e_0$) to maintain the turbulent flow and, in addition, a time-dependent modulation of the forcing ($\propto e_0 e$) is applied, $0 \le e \le 1$. The response of the system to the time-dependent stirring can be observed e.g. in the second order velocity structure function of the flow field, in particular at the outer scale L, $D(L,t) = \langle\!\langle(\boldsymbol{u}(\boldsymbol{x}+\boldsymbol{L},t) - \boldsymbol{u}(\boldsymbol{x},t))^2\rangle\!\rangle$. This $D(L,t)$ is equivalent to a Reynolds number, which we define as $Re = u_{1,rms}L/\nu$. Here, $u_{1,rms}(t)$ is the rms of one component of the velocity, varying with time t. Then, disregarding correlations on scale L,

$$D(L,t) = 2\langle\langle \boldsymbol{u}^2 \rangle\rangle = 6u_{1,rms}^2(t) = \frac{6\nu^2 Re(t)^2}{L^2}. \tag{3.2}$$

The energy put into the system at time t will travel down the energy cascade towards smaller scales and will, on average, be dissipated at time $t+\tau$, i.e., with a mean time delay τ. In other words, the dissipation at time t depends on how much energy has been in the large scales at time $t-\tau$. We approximately describe the relevant time scale τ for the cascade process by the large eddy turnover time τ_L at that time $t-\tau$,

$$\tau \simeq \tau_L = \frac{L}{u_{1,rms}(t-\tau)} = \frac{L}{\sqrt{D(L,t-\tau)/6}}. \tag{3.3}$$

More accurately, the time scale of the energy cascade is given by the sum over the eddy turnover times on all decay steps, $\tau \simeq \sum_n \tau_n$. In this sum, the largest contribution is the largest eddy turnover time τ_L. For K41 scaling the smaller eddies $r_n/L = \delta^n$, where $0 < \delta < 1$, have turnover times $\tau_n = \tau_L \delta^{2n/3}$. Thus $\tau = \tau_L \sum_n \delta^{2n/3} \equiv \tau_L a$. The common choice $\delta = 1/2$ implies $a \simeq 2.7$. Putting into intermittency corrections gives slightly smaller values of a. In this present paper we shall discuss the influence of a by comparing the limiting cases $a = 2.7$ and $a = 1$. Experimentally, in principle the parameter a could be measured by analyzing the positions, heights and widths of the response maxima, thus giving information about the energy cascade time.

If the external modulation period ω^{-1} is much larger than this intrinsic time scale τ, $\omega\tau \ll 1$, the turbulent flow will have time to adjust and will follow the periodic variations of the stirring. If, on the other hand, ω^{-1} is decreased and becomes much smaller than τ, the system can follow less and less, and feels, at small scales, an average time-independent energy input.

We calculate the time dependence of the response $D(L,t) - D_0(L)$ to a periodically modulated energy input rate, Eq. (3.1), within a variable-scale mean-field theory [10] for various driving frequencies ω. Here, $D_0(L)$ is the second order structure function for a stationary energy input rate e_0. In general, the energy flow rate through the system is an intermittently fluctuating quantity. Therefore, the cascade time as well as the response of the system are fluctuating. These fluctuations are neglected by the mean-field theory in the present study. However, on average these fluctuations result in a mean down-scale transport of energy which controls the overall properties of the flow. Therefore, we believe that within this mean-field approach we can grasp the main features of the flow correctly.

The method is explained in the next section. The behavior of the response as a function of the driving frequency ω in the case of weak modulations of the energy input rate is analyzed in Section 3.3. In Section 3.4 we discuss an alternative way to introduce time dependence into the system. The slightly different case of a modulated driving force instead of a modulated energy input rate is presented in Section 3.5. We summarize our results in Section 3.6.

3.2 Method and Model

In reference [10] an energy balance equation for the second order velocity structure function $D(r) = \langle\langle(\boldsymbol{u}(\boldsymbol{x}+\boldsymbol{r}) - \boldsymbol{u}(\boldsymbol{x}))^2\rangle\rangle$ for stationary, homogeneous, and isotropic turbulence has been derived within a variable-range mean-field theory. Here, $\boldsymbol{u}$ is the velocity and the brackets $\langle\langle ... \rangle\rangle$ denote the ensemble average. One of the essentials of this theory is to divide the velocity field into a (spatially averaged) *super-scale* velocity $\boldsymbol{u}^{(r)}$ and a (strongly fluctuating) *sub-scale* velocity $\tilde{\boldsymbol{u}}^{(r)}$. The spatial average is performed over a sphere of variable radius r, and will be denoted as $\boldsymbol{u}^{(r)}(\boldsymbol{x}) \equiv \langle \boldsymbol{u}(\boldsymbol{x}+\boldsymbol{y})\rangle_y^{(r)} \equiv \frac{3}{4\pi r^3}\int_{|\boldsymbol{y}|\le r} d^3y\, \boldsymbol{u}(\boldsymbol{x}+\boldsymbol{y})$.

The energy input rate e_{in}, which in the statistically stationary situation equals the total energy dissipation rate ϵ, is balanced in accordance with the super- and sub-scale decomposition by the energy dissipation rate on all scales larger than r complemented by the energy transfer across scale r from the super- to the sub-scales of r. In a simplified version the derived energy balance equation reads:

$$e_{in} = \epsilon = \frac{3}{2}\left(\nu + \frac{[D(r)]^2}{b^3\epsilon}\right)\frac{1}{r}\frac{d}{dr}D(r), \tag{3.4}$$

where ν is the kinematic viscosity and b the Kolmogorov constant. In the viscous subrange (VSR), where r is smaller than the Kolmogorov length scale η, $r < \eta$, the dissipation term, i.e., the first term on the rhs of Eq. (3.4), is dominating, and therefore the solution of Eq. (3.4) is $D(r) = \epsilon r^2/(3\nu)$. In the inertial subrange (ISR), instead, where $\eta \ll r \ll L$, most of the energy of the eddies is transfered down-scale. This energy transfer rate E_t, which is given by the second term on the rhs of Eq. (3.4), is determined by the decorrelation rate $\tilde{\Gamma}(r)$ of the sub-scale eddies, which itself is mainly governed by the energy dissipation rate ϵ, see [10] for details. Note again that in the stationary case the energy dissipation rate equals the energy input rate, $\epsilon = e_{in}$. In the ISR the second term on the rhs is the leading one. Then the solution of Eq. (3.4) is $D(r) = b(\epsilon r)^{2/3}$. The full energy rate balance equation (3.4) interpolates between these two limits. The Kolmogorov constant b can be calculated within this theory to be $b = 6.3$ which is consistent with the experimental value [11–14].

In our case the flow is not stationary but experiences a modulated energy input rate $e_{in}(t)$. Therefore, e_{in}, the structure function $D(r)$, and the dissipation rate ϵ in Eq. (3.4) will depend on time. Furthermore, an additional term on the rhs of Eq. (3.4) appears, taking into account the non-stationarity of the flow:

$$\begin{aligned} e_{in}(t) &= \frac{3}{2}\left(\nu + \frac{[D(r,t)]^2}{b^3\epsilon(t)}\right)\frac{1}{r}\frac{\partial}{\partial r}D(r,t) \\ &\quad + \frac{1}{2}\frac{\partial}{\partial t}\langle\!\langle \boldsymbol{u}^{(r)}(\boldsymbol{x},t)\cdot\boldsymbol{u}^{(r)}(\boldsymbol{x},t)\rangle\!\rangle. \end{aligned} \tag{3.5}$$

The correlation of the super-scale velocities can be written as

$$\langle\!\langle \boldsymbol{u}^{(r)}(\boldsymbol{x},t)\cdot\boldsymbol{u}^{(r)}(\boldsymbol{x},t)\rangle\!\rangle = \langle\!\langle \boldsymbol{u}^2(\boldsymbol{x},t)\rangle\!\rangle - \frac{1}{2}\langle\langle D(y_1+y_2,t)\rangle_{y_1}^{(r)}\rangle_{y_2}^{(r)}. \tag{3.6}$$

Following the arguments in [10] for the derivation of Eq. (3.4), we neglect multiple spatial averaging, i.e., $\langle\langle D(y_1+y_2,t)\rangle_{y_1}^{(r)}\rangle_{y_2}^{(r)} \simeq \langle D(y,t)\rangle_y^{(r)}$.

In the stationary case the energy dissipation rate $\epsilon = \nu\langle\!\langle \frac{\partial u_i}{\partial x_j}\frac{\partial u_i}{\partial x_j}\rangle\!\rangle$ can be related to the large scale quantities by

$$\epsilon = c_\epsilon \frac{u_{1,rms}^3}{L} = c_\epsilon(D(L))\frac{[D(L)]^{3/2}}{6^{3/2}L}. \tag{3.7}$$

Extending this expression to the time-dependent case, we have to take into account that the energy which is fed into the system on large scales at a time t will be dissipated on small scales at a later time $t+\tau$. We model this as follows: The energy dissipation rate at time t is assumed to depend on the large scale quantities at time $t-\tau$:

$$\epsilon(t) = c_\epsilon(D(L,t-\tau))\frac{[D(L,t-\tau)]^{3/2}}{6^{3/2}L}. \tag{3.8}$$

c_ϵ is a dimensionless function which is approximately constant ($\simeq 1$) for very large Reynolds numbers [15, 16]. In [17–19] it was shown that in general c_ϵ depends on the Reynolds number, and therefore on $D(L)$. We here use an approximation of the expression derived in [17] for high Reynolds numbers:

$$\begin{aligned} c_\epsilon(D(L)) &= \frac{9}{Re} + \sqrt{\left(\frac{6}{b}\right)^3 + \left(\frac{9}{Re}\right)^2} \\ &\simeq \left(\frac{6}{b}\right)^{3/2} + \frac{9}{Re} = \left(\frac{6}{b}\right)^{3/2} + 9\frac{\nu}{L}\sqrt{\frac{6}{D(L)}}. \end{aligned} \tag{3.9}$$

The delay time τ is determined by the implicit time-delay equation (3.3). Assuming that the solution of Eq. (3.4) in the ISR, $D(r) = b(\epsilon r)^{2/3}$, is valid up to $r = L$, we can write $D(r) = \left(\frac{r}{L}\right)^{2/3} D(L)$. Within our model, where we connect small and large scale quantities at different times, the structure function on scale $r < L$ at time t will depend on the large scale structure function at an earlier time $t-\tau$, i.e., we introduce $D(r,t) = \left(\frac{r}{L}\right)^{2/3} D(L, t-\tau)$ into Eq. (3.5). After multiplying with r, Eq. (3.5) can be integrated from $r = 0$ up to the outer length scale $r = L$:

$$\begin{aligned} \frac{1}{4}\frac{d}{dt}[D(L,t) - \alpha D(L,t-\tau)] &= -\frac{[D(L,t-\tau)]^{3/2}}{Lb^{3/2}} \\ &\quad -\frac{3\nu D(L,t-\tau)}{2L^2} + e_{in}(t), \end{aligned} \tag{3.10}$$

where $\alpha = \frac{27}{44}$ originates from the integration. In [10] it has been shown that, in the isotropic and homogeneous case, e_{in} is independent of the scale r as the forcing is assumed to act on the largest scale L only. In the stationary case the lhs of Eq. (3.10) vanishes, and together with Eqs. (3.8) and (3.9), Eq. (3.10) corresponds to $\epsilon = e_{in}$. Eq. (3.10) contains only large scale quantities. Effects of fluctuations in the energy input rate on the statistical properties of the turbulent flow as observed in [6] would influence the scaling behavior of $D(r,t)$ on intermediate scales r and therefore lead to different values of the factor α, but the structure of Eq. (3.10) would remain the same.

Using Eq. (3.2), we express the second order structure function $D(L,t)$ in Eq. (3.10) in terms of the Reynolds number $Re(t)$:

$$\begin{aligned} \frac{L^2}{\nu}\frac{d}{dt}[Re^2(t) - \alpha Re^2(t-\tau)] &= -\frac{2}{3}\left(\frac{6}{b}\right)^{3/2}[Re^2(t-\tau)]^{3/2} - 6Re^2(t-\tau) \\ &\quad +\frac{2}{3}\frac{e_0 L^4}{\nu^3}(1 + e\sin\omega t). \end{aligned} \tag{3.11}$$

Here, we have inserted the time-dependent energy input rate, Eq. (3.1). In the case a of constant energy input rate, i.e., $e = 0$, Eq. (3.11) simplifies to

$$0 = -\frac{2}{3}\left(\frac{6}{b}\right)^{3/2} Re_0^3 - 6Re_0^2 + \frac{2}{3}\frac{L^4}{\nu^3}e_0, \tag{3.12}$$

relating the stationary Reynolds number Re_0 to the stationary input rate,

$$\frac{L^4}{\nu^3}e_0(Re_0) = c_\epsilon(Re_0)Re_0^3.$$

Introducing the reduced Reynolds number $R(t) \equiv Re(t)/Re_0$ and the non-dimensional time t/τ_L^0 as t (analogously for τ and ω), Eq. (3.11) becomes

$$\begin{aligned} \frac{d[R^2(t) - \alpha R^2(t-\tau)]}{dt} &= -\frac{2}{3}\left(\frac{6}{b}\right)^{3/2}[R^2(t-\tau)]^{3/2} - \frac{6}{Re_0}R^2(t-\tau) \\ &\quad +\left(\frac{2}{3}\left(\frac{6}{b}\right)^{3/2} + \frac{6}{Re_0}\right)(1 + e\sin\omega t). \end{aligned} \tag{3.13}$$

Here, $\tau_L^0 = \frac{L}{u^0_{1,rms}}$ is the large eddy turnover time of the stationary flow. $R(t)$ is of order one. The delay time τ in units of the time scale τ_L^0 is given by

$$\tau = \frac{a}{R(t-\tau)}. \tag{3.14}$$

Eq. (3.13) describes the time evolution of $R^2(t)$, which is the square of the Reynolds number of a flow exposed to a modulated energy input rate (Eq. (3.1)), normalized by the square of the Reynolds number of a flow where only a constant, time-independent, forcing is applied.

3.3 Response of turbulent flow to energy input rate modulations

3.3.1 General trend

In the present study we shall restrict ourselves to the case of weak amplitude modulation, i.e., e in Eq. (3.1) is small. Then we expect that also the oscillating response

$$\Delta(t) \equiv R^2(t) - 1 \tag{3.15}$$

has a small amplitude, and we can linearize Eq. (3.13). The time delay τ is approximated by a time-independent constant which in our time units τ_L^0 is simply a. This approximation is justified as long as $|\Delta| \ll 1$. In Section 3.3.3 we shall discuss the limits of this approximation. We first consider $a = 1$ which means that the cascade time τ is taken as the large eddy turnover time τ_L^0. The resulting equation of motion for the response $\Delta(t)$,

$$\begin{aligned} \frac{d}{dt}[\Delta(t) - \alpha\Delta(t-\tau)] &= -\left(\left(\frac{6}{b}\right)^{3/2} + \frac{6}{Re_0}\right)\Delta(t-\tau) \\ &\quad + \left(\frac{2}{3}\left(\frac{6}{b}\right)^{3/2} + \frac{6}{Re_0}\right) e \sin\omega t, \end{aligned} \tag{3.16}$$

can be solved analytically. The solution to the linear equation (3.16) can be calculated using the ansatz:

$$\Delta(t) = eA(\omega)\sin(\omega t + \phi). \tag{3.17}$$

Here, $A(\omega)$ is the amplitude, and ϕ is the phase shift of the response which also depends on ω. Inserting this expression into Eq. (3.16) gives the explicit solution of the linear response equation (3.16):

$$\begin{aligned}\Delta(t) &= \frac{\frac{2}{3}\left(\frac{6}{b}\right)^{3/2} + \frac{6}{Re_0}}{\omega}\, e \\ &\times \frac{-\cos\omega t + \alpha\cos\Big(\omega(t+\tau)\Big) + \frac{\left(\frac{6}{b}\right)^{3/2}+\frac{6}{Re_0}}{\omega}\sin\Big(\omega(t+\tau)\Big)}{1+\alpha^2+\left(\frac{\left(\frac{6}{b}\right)^{3/2}+\frac{6}{Re_0}}{\omega}\right)^2 - 2\alpha\cos\omega\tau - 2\frac{\left(\frac{6}{b}\right)^{3/2}+\frac{6}{Re_0}}{\omega}\sin\omega\tau}.\end{aligned} \tag{3.18}$$

In the following, we set the Kolmogorov constant $b = 6$ for simplicity, which is near to the calculated value 6.3 [10] and to the experimental value in the range $6-9$ [11–14]. To recover the expressions for a general b one has to replace in the following results the terms $(1+\frac{6}{Re_0})$ and $(\frac{2}{3}+\frac{6}{Re_0})$ by $((6/b)^{3/2}+\frac{6}{Re_0})$ and $(\frac{2}{3}(6/b)^{3/2}+\frac{6}{Re_0})$, respectively. The mean amplitude of the response is determined by the energy input rate $(\frac{2}{3}+\frac{6}{Re_0})e$, i.e., the last term on the rhs of Eq. (3.16). The time derivative on the lhs of Eq. (3.16) leads to a mean decrease of the amplitude as $1/\omega$. Due to the two terms in Eq. (3.16) containing the time delay $\tau = a$, corresponding terms in the second fraction of the solution (3.18) appear, $\propto \alpha$ and $\propto (1+\frac{6}{Re_0})/\omega$, respectively, which, by the periodic dependence on $\omega\tau$ induce a periodic variation of the amplitude with the frequency ω. For low frequencies the terms $\propto (1+6/Re_0)/\omega$, originating from the first term on the rhs of Eq. (3.16), dominate, whereas for high frequencies the terms $\propto \alpha$, due to the second term on the lhs of Eq. (3.16), become more important. The latter, in particular, lead to a periodic variation of the response amplitude up to very high frequencies.

The linear response $\Delta(t) \propto e$ of the flow (with $Re_0 = 10^4$) is plotted in Fig.3.1 for four different modulation frequencies. Also the modulation of the energy input rate, $e_{in}(t)/e_0 - 1$ is plotted in Fig.3.1. The deviation of the Reynolds number from its stationary value Re_0, $\Delta(t) = (Re^2(t) - Re_0^2)/Re_0^2$, oscillates with the same frequency as the driving, for all frequencies ω. The amplitude A of this oscillation depends on the frequency. For the two small modulation frequencies, $\omega = 10^{-3}$ and $\omega = 10^{-1}$, the amplitude of the response $\Delta(t)$ is nearly the same, about two thirds of the amplitude e of the driving. For higher frequencies, the amplitude A of the response decreases. In the case of $\omega = 10$ we observe a phase shift between the forcing and the resulting response. Fig.3.2 shows the amplitude $A(\omega)$ as a function of the driving frequency for $Re_0 = 10^4$. For low frequencies the amplitude remains constant, and is two thirds, whereas for large frequencies the amplitude of the response $\Delta(t)$ decreases $\propto 1/\omega$. In addition to this decrease we note certain frequencies for which the response amplitude becomes large or very small. The distance between two maxima or two minima of the amplitude is nearly constant, see the inset of Fig.3.2. This periodic behavior in the ω-dependence of the response amplitude is due to the time delay τ. We shall explain this in the next section.

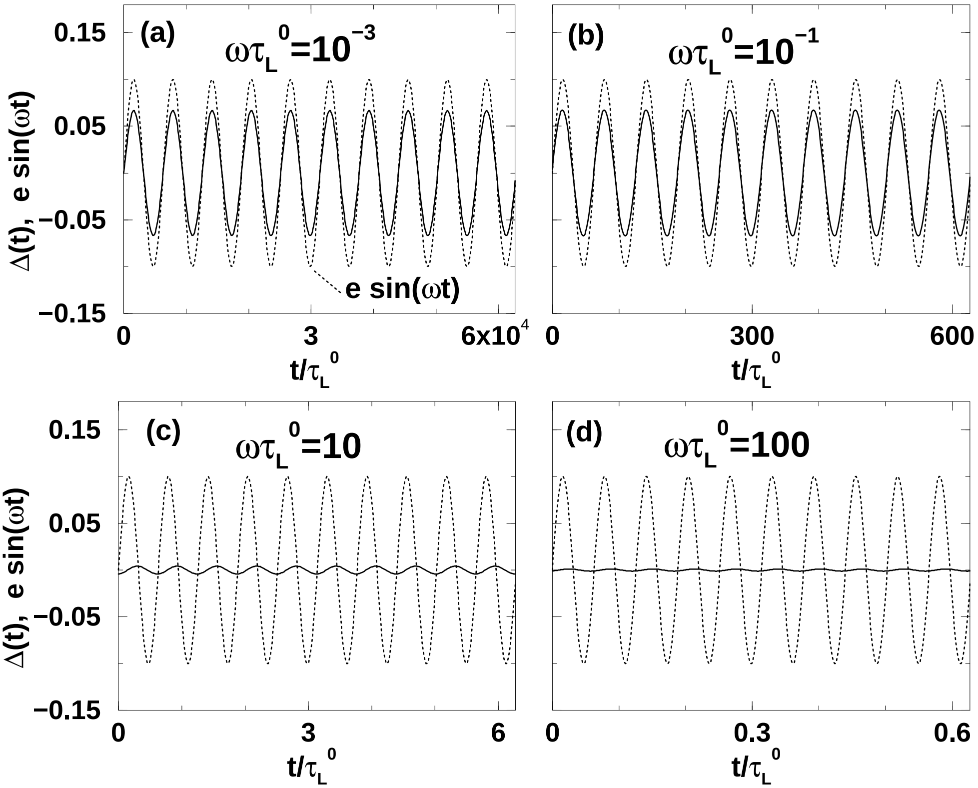

Figure 3.1: Response $\Delta(t)$ (solid lines) for four different modulation frequencies ω, the time dependent part of the energy input rate, $e_{in}(t)/e_0 - 1$ (dotted lines). The modulation amplitude is 10% of the constant input rate, $e = 0.1$, and the Reynolds number of the stationary system is chosen as $Re_0 = 10^4$. (a) $\omega\tau_L^0 = 10^{-3}$, (b) $\omega\tau_L^0 = 0.1$, (c) $\omega\tau_L^0 = 10$, (d) $\omega\tau_L^0 = 100$.

There are three time scales in the solution (3.18) of Eq. (3.16): The large eddy turnover time, by definition 1, the time delay $\tau = a$, which represents the cascade time, and the time scale of the external modulation $1/\omega$. If the modulation time scale is much larger than the large eddy turnover time, $1/\omega \gg 1$, i.e., if the driving frequency is very small, then the solution (3.18) can be approximated by

$$\Delta(t) \simeq e\frac{2}{3}\sin\Big(\omega(t+\tau)\Big). \tag{3.19}$$

We conclude $A = 2/3$, while the phase $\phi = \omega\tau$ is linear in ω for small frequencies.

If, on the other hand, the modulation frequency becomes very large, i.e, the time scale of the driving is much smaller than 1, we see from Eq. (3.18) that the amplitude

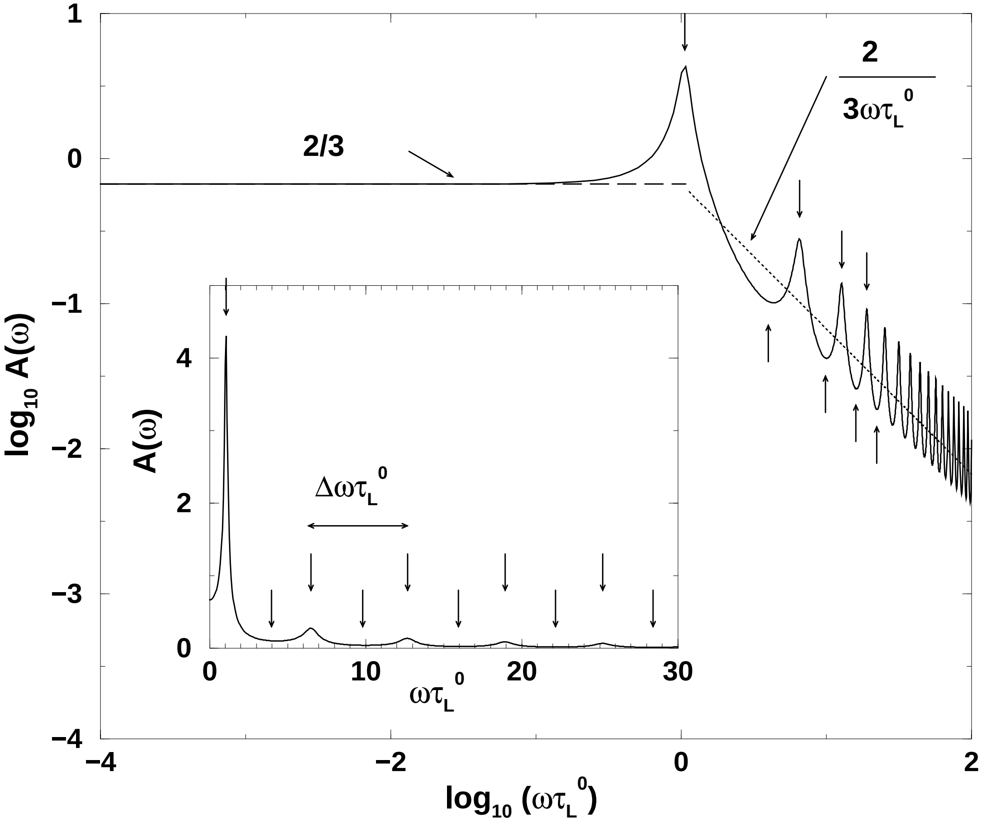

Figure 3.2: Amplitude A of the response $\Delta(t)$ as a function of the driving frequency ω (log-log-scale) for weak modulations ($e = 0.1$) of the input rate e_{in}, and $Re_0 = 10^4$. The time scale of the energy cascade is set to $\tau = a = 1$. The dashed line denotes the low frequency limit of the oscillation amplitude, $2/3$, and the dotted line corresponds to the mean trend of the high frequency limit, $\frac{3}{3\omega\tau_L^0}$. Inset: linear-scale-plot of the response amplitude versus frequency. The small arrows indicate the frequencies ω_r (in units of τ_L^0) of the response extrema calculated from the extrema of the denominator in Eq. (3.18). The horizontal arrow denotes the frequency distance $\Delta\omega$ (in units of τ_L^0) between two frequencies for which the amplitude is maximal (or minimal). It is $\Delta\omega \simeq 2\pi/\tau$ for high frequencies.

of Δ decreases as $\propto 1/\omega$:

$$\Delta(t) \simeq e\frac{(\frac{2}{3}+\frac{6}{Re_0})}{\omega}\frac{\Big[-\cos\omega t + \alpha\cos\Big(\omega(t+\tau)\Big)\Big]}{1+\alpha^2-2\alpha\cos\omega\tau}. \tag{3.20}$$

The mean trend $\propto \frac{(\frac{2}{3}+\frac{6}{Re_0})}{\omega} \simeq \frac{2}{3\omega}$ of this high frequency limit is also plotted in

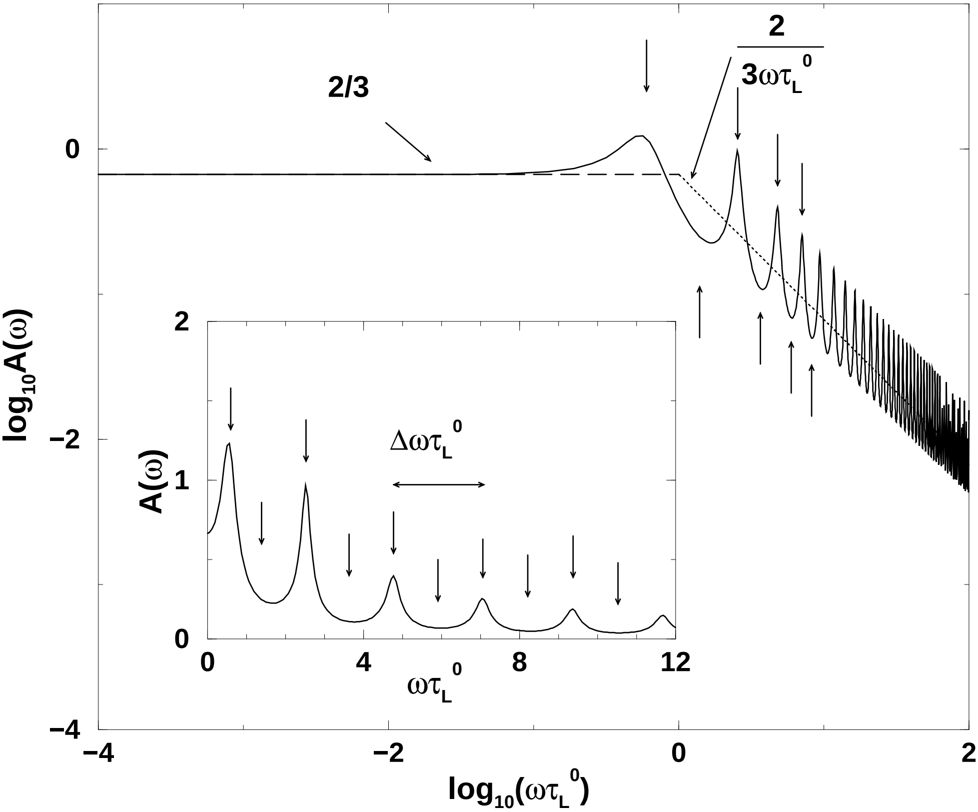

Figure 3.3: Same as Fig.3.2 but with a cascade time scale $\tau = a = 2.7$ different from the large eddy turnover time τ_L^0. Note the shift of the response maxima, the less pronounced height and greater width of the first, and the more pronounced second response peak.

Fig.3.2. The crossover between the regimes of Eq. (3.19) and (3.20) takes place at $\omega_{cross} \simeq 1$. This can be seen in Fig.3.2. The crossover frequency is not changed by taking into account the cascade time $\tau = a \neq 1$, as can be seen in Fig.3.3 which shows the response amplitude as a function of frequency for $a = 2.7$.

We have considered here only the case, where the Kolmogorov constant $b = 6$. For a general b, the crossover frequency is at $\omega_{cross} \simeq (6/b)^{3/2}$, as can be seen from the solution (3.18). This means, that the crossover from the regime of constant amplitude to the regime of $1/\omega$-decay takes place at a smaller frequency if b is larger. The positions of the response maxima, however, are only slightly shifted by a different b.

In conclusion, as long as the modulation frequency of the energy input rate is smaller than 1, i.e., the large eddy turnover time is shorter than the period of the forcing, the system has time to follow the periodic modulations with an almost constant amplitude. For higher frequencies instead, the oscillations become too fast for the system to follow, and therefore, the response becomes weaker and weaker, and phase shifted. Then the system experiences the fast modulation more and more as a constant average energy input, and the oscillations of the response vanish as $1/\omega$. This high frequency behavior has also been found for spin systems driven by an oscillating magnetic field [20].

3.3.2 Response maxima

In Fig.3.2 we have seen that there are certain frequencies for which the amplitude of the response becomes large or very small. Mathematically, these response extrema originate from the minima and maxima of the denominator in Eq. (3.18),

$$N(\omega) = \omega\Big[1 + \alpha^2 + \left(\frac{1 + \frac{6}{Re_0}}{\omega}\right)^2 - 2\alpha\cos\omega\tau - 2\frac{1 + \frac{6}{Re_0}}{\omega}\sin\omega\tau\Big]. \qquad (3.21)$$

We calculate the extrema of $N(\omega)$ numerically. The first few of them are indicated by the small arrows in Fig.3.2. The lowest frequency is near to $\omega_{r1} \simeq \pi/(3\tau) \simeq 1$. There, the first and strongest maximum of the response can be observed, where the amplitude becomes as high as $A \simeq 4.2$. Note, that this frequency is nearly equal to the crossover frequency ω_{cross} between the low and high frequency regimes of Eq. (3.19) and (3.20) only in this particular case, where $a = 1$. If we assume an energy cascade time $\tau = a = 2.7$ the frequencies of the maxima are shifted towards smaller frequencies. The height of the first maximum is decreased, i.e., $A \simeq 1.2$, whereas the height of the following maxima is slightly increased, see Fig.3.3. For very large frequencies, $\omega \gg 1$, we can estimate the frequencies of the response extrema also analytically. Then the two terms in the denominator $\propto (1 + \frac{6}{Re_0})/\omega$ can be neglected, and the extrema of $N(\omega)$ can be approximated by the extrema of $\cos\omega\tau$,

$$\omega_r(n) \simeq n\frac{\pi}{\tau}, \qquad n = 0, \pm 1, \pm 2, ... \,. \qquad (3.22)$$

Now the amplitude of Δ is at maximum for frequencies $\omega_r(n)$ with even n, and at minimum for $\omega_r(n)$ with odd n. The distance between two maximum (or minimum) amplitudes is $2\pi/\tau$ as indicated by the horizontal arrow in the inset of Fig.3.2. For the first maxima and minima at moderate frequencies this estimate is an approximation only; also their distances are not yet constant as they are for high frequencies.

In the high frequency limit, the oscillation of the response at the frequencies ω_r of maximum or minimum amplitude is phase shifted by $\phi_r(m) = (2m + 1)\pi/2$, $m = \pm 1, \pm 3, ...$:

$$\Delta(t) = e\frac{(\frac{2}{3} + \frac{6}{Re_0})}{\omega_r}\frac{(-1 \pm \alpha)\cos\omega_r t}{(1 \mp \alpha)^2} \propto \sin(\omega_r t + \phi_r). \qquad (3.23)$$

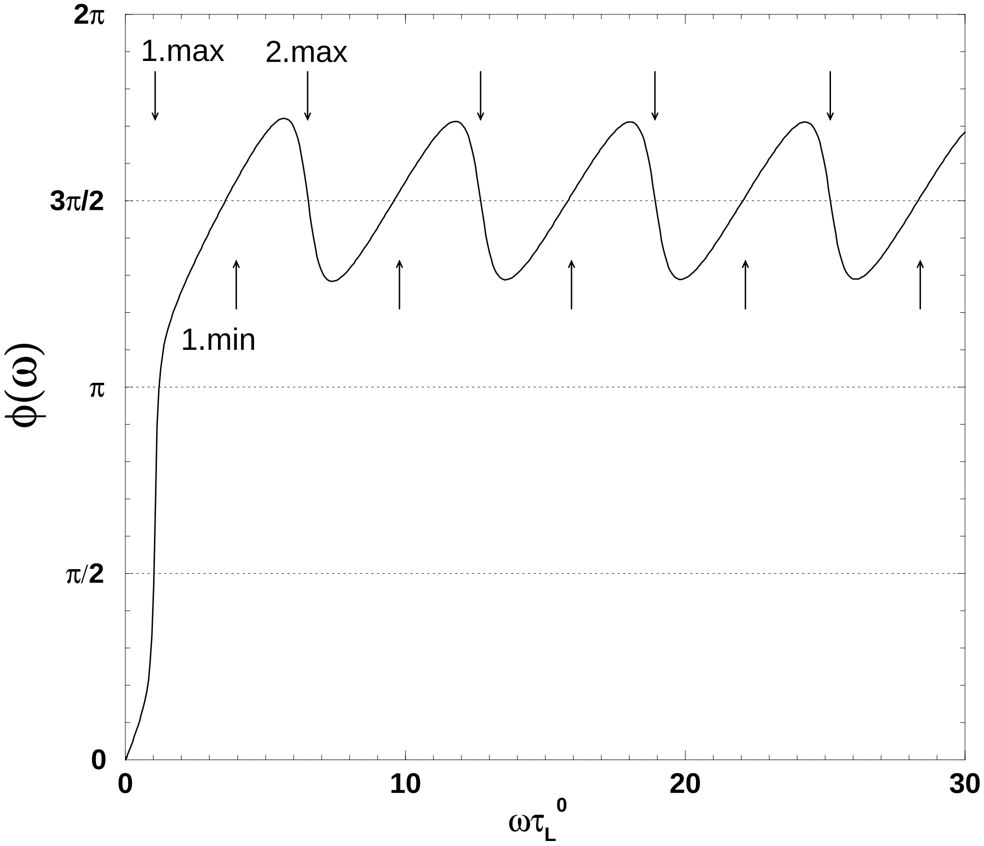

Figure 3.4: (a) Phase shift $\phi(\omega)$ as a function of the modulation frequency ω for weak modulation strength $e = 0.1$, and $Re_0 = 10^4$. The upper (lower) arrows indicate the frequencies of maximum (minimum) amplitude of the response. For small ω the phase $\phi(\omega) \propto \omega\tau$ behaves linearly.

The prefactor $(-1 \pm \alpha)$ is always negative, i.e., at the response extrema we have $\Delta(t) \propto -\cos\omega_r t = \sin(\omega_r t + \phi_r)$. In Fig.3.4 the phase shift $\phi(\omega)$, calculated from the solution (3.18), is shown as a function of the driving frequency ω for all frequencies. As the phase shift starts with $\phi(\omega = 0) = 0$ and changes continuously with increasing frequency, we find that only $m = 1$ is possible for the phase shift ϕ_r at the response extrema. The frequencies of the maximum and minimum amplitudes of Δ are indicated by arrows. The only exception is the first maximum, where the approximation for ω_r, Eq. (3.22) does not yet hold. There, the phase shift is near to $\pi/2$, corresponding to $m = 0$. Another phase shift in this model is the one between the response $\Delta(t)$ and the energy dissipation rate $\epsilon(t)$. According to Eq. (3.8) the dissipation rate is phase shifted by $-\omega\tau$ with respect to the response $\Delta(t)$, i.e., this shift is linearly growing with increasing frequency ω. At the response maxima and minima the phase shift is $-\omega_r\tau \simeq -n\pi$.

The physics behind these response extrema can be explained as follows: The time delay τ can be regarded as the (average) time which the input energy needs before it is dissipated at small scales. In the case of maximum amplitude of the response the time delay τ is a multiple jT of the period $T = 2\pi/\omega$ of the forcing, whereas for the frequencies of minimum amplitude the delay τ has an additional $T/2$. Therefore, at the extrema of the response, the energy dissipation rate and the response are either in phase (maxima) or anti-phased (minima). In the latter case the oscillation of the response is strongly reduced. If, on the other hand, the driving frequency is such that the response and the dissipation rate are in phase, the transport of energy through the system is very effective and leads to an enhanced oscillation. At the response maxima as well as at the minima the phase shift between energy input rate and response is $\phi_r = 3\pi/2$.

3.3.3 Quality of the approximation for the delay τ

In the above calculations we made an approximation for the time scale τ of the cascade process. In the linearized model, we assumed τ to be constant, $\tau = \tau_0 = a$. Now we check a posteriori the quality of this approximation. The solution (3.18) of the linearized equation (3.16) is used to compute the “correct” delay time τ step by step: The next approximation for τ is

$$\tau_1(t) = \frac{a}{\sqrt{1+\Delta(t)}}, \tag{3.24}$$

where the delay in Eq. (3.14) is still neglected. Further steps are:

$$\begin{aligned} \tau_2(t) &= \frac{a}{\sqrt{1+\Delta(t-\tau_1)}}, \\ \tau_3(t) &= \frac{a}{\sqrt{1+\Delta(t-\tau_2)}}, \quad \text{etc.} \end{aligned} \tag{3.25}$$

In Fig.3.5 $\tau_0 = a$, τ_1, τ_2, and τ_3 are plotted for different frequencies. For ω = 0.01, the difference between τ_1, τ_2, and τ_3 is not visible. The variation of the $\tau_i(t)$, (i = 1,2,3), is largest at the frequency where the amplitude of Δ is maximum, i.e., at $\omega \simeq \frac{1}{\tau_0}$. For all other frequencies, including at the response maxima, the variation of the $\tau_i(t)$ is much smaller than τ_0 and $1/\omega$. At these frequencies it seems reasonable to approximate τ by the constant $\tau_0 = a$. In Eq. (3.16) the delay τ enters into two terms, in $\propto \partial_t\Delta(t-\tau)$ on the lhs, and in $\propto \Delta(t-\tau)$ on the rhs. We calculate the relative error of these terms if $\tau = \tau_0$ instead of $\tau = \tau_i$ ($i = 1, 2, 3$) is employed, using the

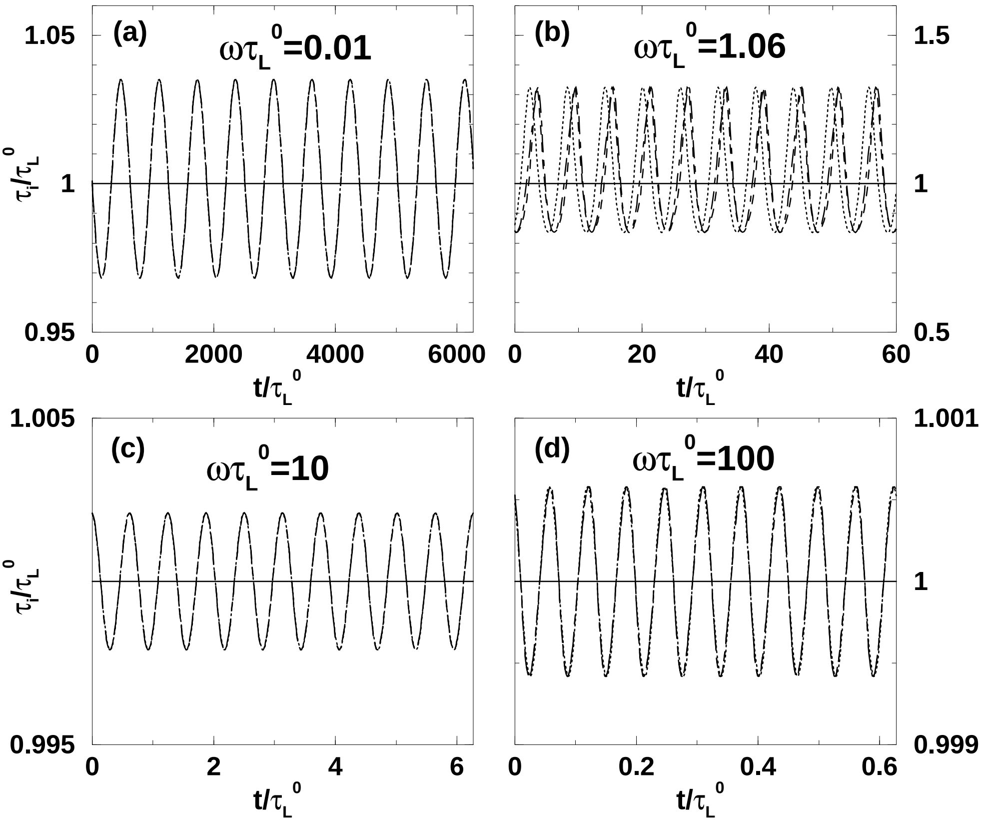

Figure 3.5: Successive approximations of the delay time τ: First, constant approximation $\tau_0 = a$ (solid lines); second, time dependent approximation τ_1 (dotted lines); third approximation τ_2 (dashed lines); fourth approximation τ_3 (dashed dotted lines) for the delay time τ, see Eqs. (3.24,3.25). (a) $\omega\tau_L^0 = 0.01$. (b) $\omega\tau_L^0 = 1.06$. (c) $\omega\tau_L^0 = 10$. (d) $\omega\tau_L^0 = 10^2$. In (a), (c) and (d) the time dependent $\tau_i(t)$ for $i = 1, 2, 3$ are indistinguishable.

solution (3.18) for Δ:

$$\delta_1(\tau_i) = \sqrt{\frac{\int_0^{2\pi/\omega}[\cos(\omega(t-\tau_0)+\phi) - \cos(\omega(t-\tau_i)+\phi)]^2 dt}{\int_0^{2\pi/\omega}\cos^2(\omega(t-\tau_0)+\phi)\, dt}}, \tag{3.26}$$

for the term on the lhs, and

$$\delta_2(\tau_i) = \sqrt{\frac{\int_0^{2\pi/\omega}[\sin(\omega(t-\tau_0)+\phi) - \sin(\omega(t-\tau_i)+\phi)]^2 dt}{\int_0^{2\pi/\omega}\sin^2(\omega(t-\tau_0)+\phi)\, dt}}, \tag{3.27}$$

for the term on the rhs. The errors δ_1 and δ_2 are summarized in table 3.1 for the

	$\delta_1(\tau_1)$	$\delta_1(\tau_2)$	$\delta_1(\tau_3)$
$\omega\tau_L^0 = 0.01$	2.9×10^{-4}	2.9×10^{-4}	2.9×10^{-4}
$\omega\tau_L^0 = 1.06$	0.15	0.22	0.23
$\omega\tau_L^0 = 10$	0.016	0.016	0.016
$\omega\tau_L^0 = 100$	0.046	0.046	0.046

	$\delta_2(\tau_1)$	$\delta_2(\tau_2)$	$\delta_2(\tau_3)$
$\omega\tau_L^0 = 0.01$	1.7×10^{-4}	1.7×10^{-4}	1.7×10^{-4}
$\omega\tau_L^0 = 1.06$	0.22	0.11	0.12
$\omega\tau_L^0 = 10$	0.013	0.013	0.013
$\omega\tau_L^0 = 100$	0.036	0.036	0.036

Table 3.1: Relative errors δ_1, δ_2 according to Eqs. (3.26) and (3.27) made in the two relevant terms of Eq. (3.16) by using the constant time delay $\tau_0 = a$ instead of the higher order approximations $\tau_i(t)$ for τ.

four chosen frequencies of Fig.3.5. As expected, the errors are largest for the frequency with maximum response amplitude, $\omega = 1.06$, where it becomes up to 23%. For $\omega = 10$ and beyond it is between 1 and 5%. If one would allow for a time dependence of τ in Eq. (3.16) the response maxima would probably become broader, possibly less pronounced. However, within this mean field theory we anyhow can make only approximate statements about the frequencies and the values of the amplitudes at the response maxima. Namely, in the mean-field approach the effects of the fluctuations on the structure function are neglected. Therefore we believe that even with this approximation for the delay time τ we can qualitatively predict the basic features of the system, which are the decrease of the amplitude of the response for high modulation frequencies, and the existence of response maxima at certain frequencies due to the finite time needed by the energy cascade process. The validity of the approximation for τ will improve for smaller amplitudes e of the modulation. However, for smaller e the total amplitude eA of the response will decrease as well and finally the amplitude of the response maxima and minima will become so small that, in experiments or numerical simulations, the fluctuations will be larger than the maxima and minima.

3.4 An alternative argument to introduce the time-delay

The energy balance equation (3.4) and the expression for the energy dissipation rate ϵ, Eq. (3.7), hold for stationary systems. The time dependence of the quantities in these equations in Section 3.2 has been introduced a posteriori by arguments based on the picture of the energy cascade. It was not derived from the Navier-Stokes equation, but is a modeling ansatz. Therefore, there are several arguments to introduce this time dependence. We want to discuss here another way of arguments which leads to a slightly different equation for the response. The idea is to start from an equation which is already integrated over all scales, i.e., does not depend on the scale r any more in contrast to Eq. (3.4) in Section 3.2. The total energy per unit mass of the flow is $E \simeq 3u_{1,rms}^2/2$. It is basically determined by the energy of the large scales. The change with time of this energy equals the dissipation rate and the energy input rate:

$$\frac{d}{dt}E(t) = -\epsilon(t) + e_{in}(t). \tag{3.28}$$

As the energy needs a time τ to travel down the eddy cascade before it is dissipated, ϵ at time t may be expressed with Eq. (3.8) and $E = \frac{1}{4}D(L)$ by the total energy E at time $t - \tau$:

$$\epsilon(t) = c_\epsilon(E(t-\tau)) \left(\frac{2}{3}\right)^{3/2} \frac{[E(t-\tau)]^{3/2}}{L}.$$

Together with the approximation for c_ϵ, Eq. (3.9), we get:

$$\begin{aligned} \frac{d}{dt}E(t) &= -\frac{[4E(t-\tau)]^{3/2}}{b^{3/2}L} \\ &\quad -6\frac{\nu}{L^2}E(t-\tau) + e_{in}(t). \end{aligned} \tag{3.29}$$

As in Section 3.2 we express the energy E by the Reynolds number, $E = \frac{3\nu^2}{2L^2}Re^2$, write the energy input in terms of the stationary Reynolds number Re_0, Eq. (3.12), and introduce the reduced Reynolds number, $R(t) = Re(t)/Re_0$. Then, in time units of τ_L^0:

$$\begin{aligned} \frac{d}{dt}R^2(t) &= -\frac{2}{3}\left(\frac{6}{b}\right)^{3/2}[R^2(t-\tau)]^{3/2} \\ &\quad -\frac{6}{Re_0}R^2(t-\tau) \\ &\quad +\left(\frac{2}{3}\left(\frac{6}{b}\right)^{3/2} + \frac{6}{Re_0}\right)(1 + e\sin\omega t). \end{aligned} \tag{3.30}$$

The only difference between this equation and the previous one, derived in Section 3.2 (Eq. (3.13)), is that here the term $\propto dR^2(t-\tau)/dt$ is missing.

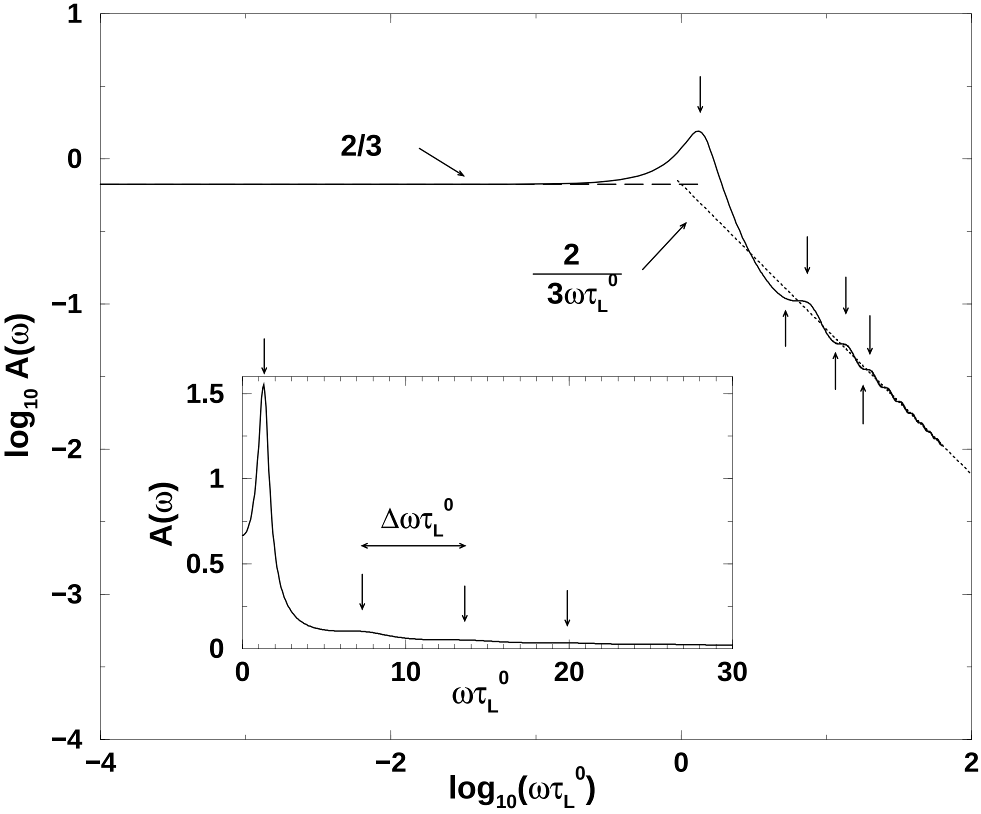

Figure 3.6: Amplitude A of the response $\Delta(t)$ as a function of the driving frequency ω (log-log-scale) for weak modulations ($e = 0.1$) of the energy input rate e_{in}, and $Re_0 = 10^4$ calculated from Eq. (3.30) in linear approximation. The dashed line denotes the low frequency limit of the oscillation amplitude, 2/3, and the dotted line corresponds to the mean trend of the high frequency limit, $\frac{2}{3\omega\tau_L^0}$. Inset: linear-scale-plot of the response amplitude versus frequency. The small arrows indicate the frequencies of maximum amplitude ω_r (in units of τ_L^0) calculated from the minima of the denominator in Eq. (3.31). The horizontal arrow denotes the frequency distance $\Delta\omega$ (in units of τ_L^0) between two frequencies for which the amplitude is maximal (or minimal). It is $\Delta\omega \simeq 2\pi/\tau$ for high frequencies.

If we solve Eq. (3.30) within the same linear approximation as employed in Section 3.3 for Eq. (3.13), we find the same features for the response, see Fig. 3.6.

The solution of the linearized equation obtained from Eq. (3.30) reads:

$$\Delta(t) = e\frac{(\frac{2}{3} + \frac{6}{Re_0})}{\omega} \frac{\left[-\cos\omega t + \frac{1+\frac{6}{Re_0}}{\omega} \sin\Big(\omega(t+\tau)\Big)\right]}{1 + (\frac{1+\frac{6}{Re_0}}{\omega})^2 - 2\frac{1+\frac{6}{Re_0}}{\omega} \sin\omega\tau}. \tag{3.31}$$

Here we have again set $b = 6$ for simplicity. The response maxima are also observed, but they are less pronounced and slightly shifted. The amplitude at the first (and strongest) maximum has only a value of $A_E \simeq 1.6$. In the linear response solution (3.18) of the previous model the terms originating from the second term on the lhs of Eq. (3.16) were responsible for the strong variation of the amplitude at high frequencies. These terms are missing in the present model. Therefore, we observe weaker amplitude maxima and minima at high frequencies in this model, cf. Fig.3.6. If we take the extended cascade time $\tau = a > 1$ into account, e.g. $a = 2.7$, the response maxima are shifted towards smaller frequencies as discussed in Section 3.3.2. However, in this model, the heights of all maxima including the first one is then slightly increased. At the response maxima the energy cascade time scale τ and the period of the driving modulation are not multiples of each other as they are in the previous model, i.e., the response and the energy dissipation rate are not exactly in phase. If one would observe the response maxima in experiments or numerical simulations, one could distinguish between the two models by studying the ratio between the frequencies of the response maxima and the cascade time scale τ. The phase shift ϕ between the energy input rate and the response becomes negative and oscillates around $-\pi/2$ for higher frequencies. At the response extrema it is near to $\phi_r \simeq -\pi/2$. Note that in the previous model the phase shift was always positive.

The two arguments to introduce the time delay are similar and are based on the same physical idea of a finite time lapse of the cascade process. However, we tend to prefer the first one, Section 3.2, because it introduces the time dependence at an earlier stage. Eq. (3.4) still resolves the scales r and it is therefore closer to the Navier-Stokes equation than Eq. (3.28).

3.5 Response of turbulent flow to a modulated driving force

In the previous sections we have studied the effect of a modulated energy input rate on turbulent flow. However, the energy input rate may not be a quantity which can be easily controlled in experiments. In some experiments it is more convenient to modulate the driving force instead. Then the resulting energy input rate as well as the total energy of the system can be considered as a response of the system. Therefore, in this section, we show how to treat this slightly modified case within the variable-range mean-field theory and what differences we expect in these two different response functions.

The derivation of Eq. (3.10) for the response of the system in terms of the structure function $D(L,t)$ remains the same as explained in Section 3.2. The energy input rate $e_{in}(t)$ in that equation is given by $e_{in}(t) = \langle\langle u_i^{(r)}(\boldsymbol{x},t) f_i^{(r)}(\boldsymbol{x},t)\rangle\rangle$. To introduce a modulated forcing instead of a modulated energy input rate, we therefore assume:

$$\begin{aligned} e_{in}(t) &\simeq D(L,t)^{1/2} f(t) \\ &= D(L,t)^{1/2} f_0 (1 + e_f \sin\omega t) \end{aligned} \tag{3.32}$$

Here, f_0 is the strength of the (stationary) forcing and e_f the amplitude of the modulation. As has been discussed in Section 3.2, we express the response in terms of the Reynolds number $Re(t)$ and relate the stationary Reynolds number Re_0 with the stationary forcing strength f_0, similar to Eq. (3.12). Then we introduce the reduced Reynolds number $R(t) = \frac{Re(t)}{Re_0}$ and the dimensionless time $\tilde{t} = t/\tau_L^0$. The tilde is dropped in the following. The analogous equation to (3.13) becomes:

$$\begin{aligned} \frac{d[R^2(t) - \alpha R^2(t-\tau)]}{dt} &= -\frac{2}{3}[R^2(t-\tau)]^{3/2} - \frac{6}{Re_0} R^2(t-\tau) \\ &\quad + (R^2(t))^{1/2}\left(\frac{2}{3} + \frac{6}{Re_0}\right)(1 + e_f \sin\omega t), \end{aligned} \tag{3.33}$$

where b is set to $b = 6$. We again assume small modulation amplitudes, i.e., $e_f \ll 1$, and linearize Eq. (3.33) in $\Delta(t) \equiv R^2(t) - 1$. As before, the time delay τ is approximated by the time-independent constant a. With the same ansatz Eq. (3.17) as in Section 3.3.1 for modulated energy input rate, the linearized equation can be solved analytically, and the solution reads:

$$\begin{aligned} \Delta(t) &= e_f \frac{(\frac{2}{3} + \frac{6}{Re_0})}{\omega}\Big[-\cos\omega t + \alpha\cos\left(\omega(t+\tau)\right) \\ &\quad + \frac{1 + \frac{6}{Re_0}}{\omega}\sin\left(\omega(t+\tau)\right) - \frac{(\frac{2}{3} + \frac{6}{Re_0})}{2\omega}\sin\omega t\Big] \\ &\quad \times \Big[1 + \alpha^2 + \left(\frac{1 + \frac{6}{Re_0}}{\omega}\right)^2 + \left(\frac{(\frac{2}{3} + \frac{6}{Re_0})}{2\omega}\right)^2 - 2\alpha\cos\omega\tau \\ &\quad - 2\frac{1 + \frac{6}{Re_0}}{\omega}\sin\omega\tau + \frac{(\frac{2}{3} + \frac{6}{Re_0})}{\omega}\left(\alpha\sin\omega\tau - \frac{1 + \frac{6}{Re_0}}{\omega}\cos\omega\tau\right)\Big]^{-1}. \end{aligned} \tag{3.34}$$

This solution is very similar to the solution (3.18) for a modulated energy input rate, but it contains some additional terms in both the numerator and the denominator. These terms only slightly modify the frequency dependence of the response $\Delta(t)$. In Fig.3.7 the amplitude $A(\omega)$ of the response Δ is plotted as a function of driving

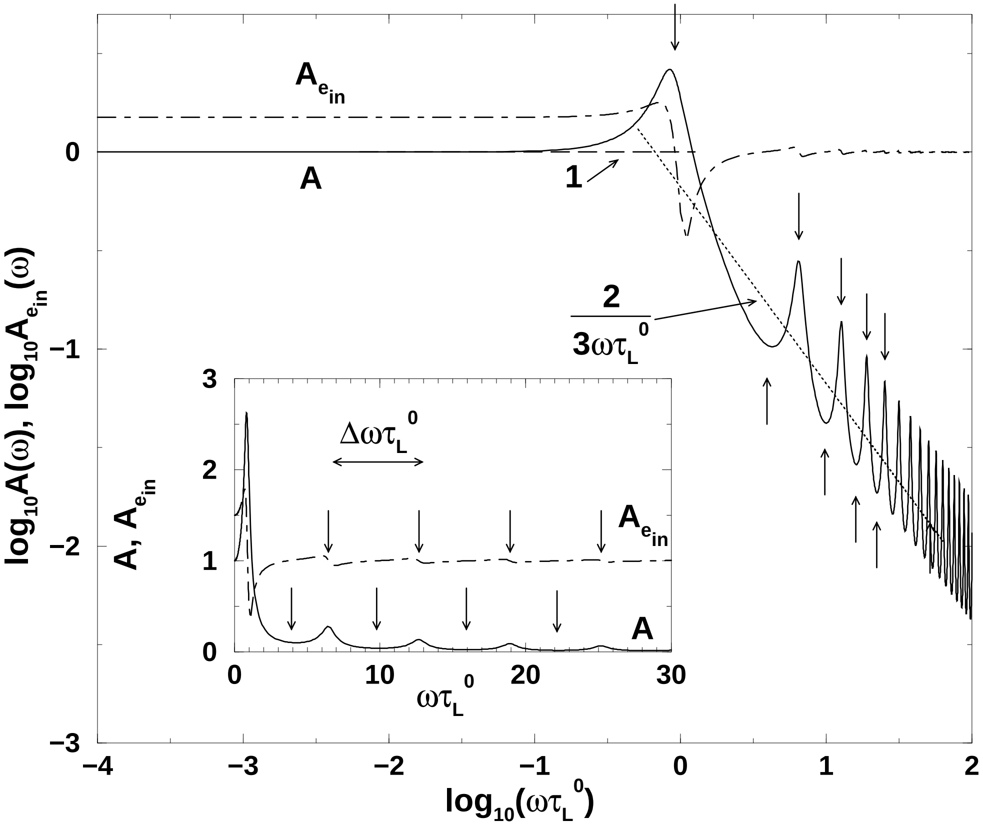

Figure 3.7: Amplitude A of the response $\Delta(t)$ as a function of the driving frequency ω (log-log-scale) for weak modulations ($e_f = 0.1$) of the driving force f, and $Re_0 = 10^4$. The time scale of the energy cascade is set to $\tau = a = 1$. The dashed line denotes the low frequency limit of the oscillation amplitude, 1, and the dotted line corresponds to the mean trend of the high frequency limit, $\frac{2}{3\omega\tau_L^0}$. The dashed-dotted line represents the amplitude of the resulting energy input rate $e_{in}(t)$. Inset: linear-scale-plot of the response amplitude (solid line) and the energy input amplitude (dashed-dotted line) versus frequency. The small arrows indicate the frequencies ω_r (in units of τ_L^0) of the response extrema calculated from the extrema of the denominator in Eq. (3.34). The horizontal arrow denotes the frequency distance $\Delta\omega$ (in units of τ_L^0) between two frequencies for which the amplitude is maximal (or minimal). It is $\Delta\omega \simeq 2\pi/\tau$ for high frequencies.

frequency for $Re_0 = 10^4$. As for the modulated energy input rate we note that the amplitude remains constant for low frequencies and decreases as $\propto 1/\omega$ for high frequencies. Also the response maxima and minima can be observed. Quantitatively, the low frequency limit for a modulated forcing is different from the modulated energy input rate case. For low driving frequencies, $\omega \ll 1/\tau$, we can approximate Eq. (3.34) by:

$$\Delta(t) \simeq e_f \frac{\frac{2}{3\omega}(\frac{1}{\omega}\sin(\omega(t+\tau)) - \frac{1}{3\omega}\sin\omega t)}{(\frac{1}{\omega})^2 + (\frac{1}{3\omega})^2 - \frac{2}{3\omega^2}\cos\omega\tau}. \tag{3.35}$$

The terms $6/Re_0 \ll 1$ have been omitted here for simplicity. In the limit $\omega\tau \to 0$, with $\sin\omega\tau \to 0$ and $\cos\omega\tau \to 1$, the amplitude A of the response (cf. Eq. (3.17)) becomes equal to one instead of two thirds (cf. Eq. (3.19)) for a modulated energy input rate. The frequencies of the response maxima and minima are determined by the extrema of the denominator of the solution (3.34). They are slightly shifted as compared to the case with modulated energy input rate (Eq. (3.18)). The amplitude at the first maximum is smaller than in the case with modulated energy input rate, namely $A_E \simeq 2.7$. However, in the limit of very high driving frequencies, $\omega \gg \frac{1}{\tau}$, Eq. (3.34) can be approximated by Eq. (3.20), i.e., the response amplitudes of both cases become identical.

It was pointed out in the beginning of this section that, if we modulate the driving force, the energy input rate is not a controlled quantity, but can be considered as well as a response of the system. This has been measured in a recent experimental study by Cadot et al. [21]. Within the mean-field theory the energy input rate for a modulated driving force can be calculated as:

$$\frac{e_{in}(t)}{e_{in,0}} = \sqrt{1+\Delta(t)} \quad (1 + e_f \sin\omega t), \tag{3.36}$$

where $e_{in,0} = D_{L,0}^{1/2} f_0$ is the stationary energy input rate for constant forcing without modulation. In order to extract the amplitude of the energy input rate, we fit it by a function of the form $\frac{e_{in}(t)}{e_{in,0}} = 1 + e_f A_{e_{in}} \sin(\omega(t+\phi))$. This is justified as long as the modulation amplitude e_f is small, i.e., $e_f \ll 1$, because then $\Delta(t)$ is of the same order of magnitude as e_f and Eq. (3.36) can be approximated by

$$\frac{e_{in}(t)}{e_{in,0}} - 1 \simeq \frac{1}{2}\Delta(t) + e_f \sin\omega t + O(\Delta^2). \tag{3.37}$$

The amplitude $A_{e_{in}}$ of the energy input rate is included in Fig.3.7 as a dashed-dotted line. For low driving frequencies, $\omega \ll \frac{1}{\tau}$, the amplitude $A_{e_{in}}$ is nearly constant and is $3/2$, whereas for high frequencies it decreases and finally saturates at one. Also the response maxima can be observed in the energy input rate: At the same frequencies, where the response Δ shows amplitude maxima, we observe a maximum directly followed by a minimum in the amplitude of the energy input rate.

In conclusion, if the driving force instead of the energy input rate is modulated, the general behavior of the response in terms of the second order structure function on the largest scale remains the same, including the response maxima and minima. For low driving frequencies, the amplitude of the response becomes equal to the amplitude of the forcing. In addition, the energy input rate can be regarded as a different measure for the response of the system, which also shows the response maxima at frequencies connected with the energy cascade time scale τ.

3.6 Conclusions

We calculated the response of isotropic and homogeneous turbulence to a weak modulation of the energy input rate e_{in} within a mean-field theory. For low frequencies the system follows the input rate modulation whereas for high frequencies the amplitude of the response decreases $\propto 1/\omega$. Due to the intrinsic time scale of the system, the eddy turnover time τ, which also characterizes the energy transport time down the eddy cascade, there are certain frequencies, $\omega_r \simeq n\frac{\pi}{\tau}$, where the amplitude of the response is either increased or decreased. At these frequencies the phase shift ϕ between the energy input rate and the response is $\phi_r \simeq 3\pi/2$. The response extrema occur when the eddy turnover time is an even or odd multiple of half the modulation period $T/2 = \pi/\omega$, respectively. In the case of response maxima, the energy dissipation rate and the response of the system are in phase. This can be understood as a very effective transport of energy through the system. At the amplitude minima, instead, the response of the system is strongly reduced. Then, the energy dissipation rate and the response are exactly anti-phased.

In the mean-field approach the fluctuations of the energy flow rate through the system and of the large eddy turnover time are neglected. In experiment or numerical simulation the fluctuations are however present. They may lead to broader and less pronounced response maxima, i.e., partly wash out the response maxima and minima.

With increasing modulation amplitude e of the energy input rate the response maxima are expected to become more significant due to the better signal to fluctuation ratio. But remember that for higher modulation amplitudes e, the time scale of the eddy cascade, which enters into our model as a time delay, becomes time dependent. This as well could lead to less pronounced response maxima as discussed in Section 3.3.3.

A way to check if the characteristic feature of the response maxima and minima can still be well identified under the influence of fluctuations, would be to perform numerical simulations of the Navier-Stokes equation with a modulated driving. However, as not only high Reynolds numbers are needed to achieve fully developed, isotropic and homogeneous turbulence, but also the response as a function of time for a wide range of frequencies has to be calculated, the computational effort would be too high. Therefore, numerical simulations within two dynamical cascade models of turbulence, the GOY shell model [22–28] and the reduced wave vector set approximation (REWA) [29–31], were performed [32], see Chapter 4. These models take into account the fluctuations. The basic trend of the frequency dependence of the response amplitude as calculated within the mean-field model can be reproduced in both numerical models. We also clearly find the main maximum in both models although it is of course washed out by the fluctuations. The higher maxima and minima however seem to be completely washed out.

Also a recent experimental study of modulated turbulence by Cadot et al. [21] showed evidence for the existence of the response maxima. This experiment may be comparable with our study of a modulated driving force as discussed in Section 3.5. The response maxima were measured in the amplitude of the energy input rate. In addition, a constant response amplitude for low driving frequencies and a $1/\omega$-decay of the velocity response amplitude for large frequencies has been observed. This is in agreement with the $1/\omega$-decay of the energy response amplitude which we have found in the mean-field model. The velocity response $(u(t) - u_0)/u_0 = \Delta_u(t)$, where $u(t)$ is the measured velocity modulus and u_0 the (stationary) mean velocity, is connected to the energy response $\Delta(t)$ which we have calculated in this chapter by $1 + \Delta(t) = u(t)^2/u_0^2 = [1 + \Delta_u(t)]^2 \simeq 1 + 2\Delta_u(t) + O(\Delta_u^2)$. As only small modulation amplitudes are considered the term $+O(\Delta_u^2)$ will be negligible because $\Delta_u \ll 1$. Therefore, a $1/\omega$-decay of the amplitude of Δ_u is in agreement with a $1/\omega$-decrease of the amplitude of Δ.

We hope that the present work will stimulate even more experimental and numerical studies on the role of the energy cascade time scale in modulated turbulence.

Acknowledgments: We thank R. Pandit and B. Eckhardt for very helpful discussions. The work is part of the research program of the Stichting voor Fundamenteel Onderzoek der Materie (FOM), which is financially supported by the Nederlandse Organisatie voor Wetenschappelijk Onderzoek (NWO). This research was also supported by the German-Israeli Foundation (GIF) and by the European Union under contract HPRN-CT-2000-00162.

References

[1] T. P. Rippeth, N. R. Fisher, and J. H. Simpson, J. Phys. Oceanogr. **31**, 2458 (2001).

[2] A. Scotti and U. Piomelli, Phys. Fluids **13**, 1367 (2001).

[3] X. L. Qiu, S. H. Yao, and P. Tong, Phys. Rev. E **61**, R6075 (2000).

[4] X. L. Qiu and P. Tong, Phys. Rev. E **64**, 036304 (2001).

[5] X. L. Qiu and P. Tong, Phys. Rev. Lett **87**, 094501 (2001).

[6] R. Labbé, J. F. Pinton, and S. Fauve, Phys. Fluids **8**, 914 (1996).

[7] S. Aumaître, S. Fauve, and J. F. Pinton, Eur. Phys. J. B **16**, 563 (2000).

[8] D. Lohse, Phys. Rev. E **62**, 4946 (2000).

[9] J. O. Hooghoudt, D. Lohse, and F. Toschi, Phys. Fluids **13**, 2013 (2001).

[10] H. Effinger and S. Grossmann, Z. Phys. B **66**, 289 (1987).

[11] A. S. Monin and A. M. Yaglom, *Statistical Fluid Mechanics* (The MIT Press, Cambridge, Massachusetts, 1975).

[12] K. R. Sreenivasan, Phys. Fluids **7**, 2778 (1995).

[13] K. R. Sreenivasan and R. A. Antonia, Ann. Rev. of Fluid Mech. **29**, 435 (1997).

[14] S. B. Pope, *Turbulent Flows* (Cambridge University Press, Cambridge, 2000).

[15] K. R. Sreenivasan, Phys. Fluids **27**, 1048 (1984).

[16] K. R. Sreenivasan, Phys. Fluids **10**, 528 (1998).

[17] D. Lohse, Phys. Rev. Lett. **73**, 3223 (1994).

[18] S. Grossmann, Phys. Rev. E **51**, 6275 (1995).

[19] G. Stolovitzky and K. R. Sreenivasan, Phys. Rev. E **52**, 3242 (1995).

[20] M. Rao, H. Krishnamurthy, and R. Pandit, Phys. Rev. B **42**, 856 (1990).

[21] O. Cadot, J. H. Titon, and D. Bonn, *Experimental observation of resonances in modulated turbulence*, Preprint, submitted to J. Fluid Mech. (2002).

[22] E. B. Gledzer, Sov. Phys. Dokl. **18**, 216 (1973).

[23] M. Yamada and K. Ohkitani, J. Phys. Soc. Jpn. **56**, 4210 (1987).

[24] M. Yamada and K. Ohkitani, Prog. Theor. Phys. **79**, 1265 (1988).

[25] K. Ohkitani and M. Yamada, Prog. Theor. Phys. **81**, 329 (1989).

[26] M. H. Jensen, G. Paladin, and A. Vulpiani, Phys. Rev. A **43**, 798 (1991).

[27] L. Kadanoff, D. Lohse, J. Wang, and R. Benzi, Phys. Fluids **7**, 617 (1995).

[28] L. Biferale, Ann. Rev. Fluid Mech. **35**, 441 (2003).

[29] J. Eggers and S. Grossmann, Phys. Fluids A **3**, 1958 (1991).

[30] S. Grossmann and D. Lohse, Z. Phys. B **89**, 11 (1992).

[31] S. Grossmann and D. Lohse, Phys. Fluids **6**, 611 (1994).

[32] A. von der Heydt, S. Grossmann, and D. Lohse, *Numerical simulations of modulated turbulence*, Preprint, submitted to Phys. Rev. E (2003).

Chapter 4

Numerical simulations of modulated turbulence [*]

Numerical simulations of fully developed turbulence driven by a modulated energy input rate or driving force are performed within two dynamical cascade models, the GOY shell model and a reduced wave vector set approximation of the Navier-Stokes equation (REWA). The frequency behavior of the system response is studied and compared with predictions from a variable-range mean-field theory, which excludes turbulent fluctuations. In agreement with the mean-field approach we find a constant response amplitude for low driving frequencies and a $1/\omega$-decay of the amplitude for high frequencies. In the mean-field theory, the finite cascade time scale had lead to an oscillating behavior of the response amplitude as a function of the driving frequency. In the simulations of both models we observe the main maximum. The higher maxima and minima are completely washed out by fluctuations.

4.1 Motivation

Many realistic turbulent flows are subject to modulated driving forces, as e.g. the atmosphere of the earth driven by the periodic heating of the sun or the pulsed flow through a pipeline. Three dimensional turbulence is characterized by an energy cascade from the outer length scale, where the forcing acts, to the dissipative scale, where most of energy is dissipated, see e.g. [1, 2]. The down-cascading of energy

---

[*] See also A. von der Heydt, S. Grossmann, and D. Lohse *Numerical simulations of modulated turbulence*, Preprint, submitted to Phys. Rev. E (2003)

from large to small scales takes a characteristic time τ. In a statistically stationary flow the energy dissipation rate equals the energy input rate. In a situation with time dependent energy input, on the other hand, this statement will only hold on *average,* whereas the energy dissipation at a certain time t is expected to depend on the energy input at an *earlier* time due to the finite time delay of the energy transfer.

In a previous work [4] the effect of an energy input rate modulated in time,

$$e_{in}(t) = \epsilon_0(1 + e \sin \omega t), \tag{4.1}$$

with a modulation amplitude $e \ll 1$ and a modulation frequency ω, has been studied within a variable-range mean-field theory [5]. The response of the system can be observed in the second order velocity structure function of the flow field at the outer length scale L, $D_L(t) = \langle\!\langle(\boldsymbol{u}(\boldsymbol{x} + \boldsymbol{L}, t) - \boldsymbol{u}(\boldsymbol{x}, t))^2\rangle\!\rangle = 6u_{1,rms}$, which is equivalent to the Reynolds number $Re(t) = u_{1,rms}(t)L/\nu$ of the flow and the total energy $E(t) = \langle\!\langle \boldsymbol{u}^2 \rangle\!\rangle/2$ of the system. Here, $u_{1,rms}$ is the rms of one velocity component and ν is the viscosity. The response follows the oscillation of the energy input rate with almost constant modulation amplitude at low frequencies ω of the energy input rate, whereas the response amplitude strongly decreases ($\propto 1/\omega$) at higher frequencies. The finite energy transfer time τ plays a crucial role in this theory. This time τ is the average time the energy stays within the system while it is transported by the interaction cascade from the large eddies towards the small eddies, where it is finally dissipated. This intrinsic time scale of the system is a multiple a of order 1 of the large eddy turnover time τ_L, corresponding to the sum over the eddy turnover times on all scales. τ^{-1} determines the frequency at which the crossover takes place between the regime of constant response amplitude and decreasing amplitude. In addition, it leads to an oscillating behavior of the system response with driving frequency ω, where the maxima and minima are at frequencies connected to the inverse of the energy transfer time τ. In the limit of large frequencies ω, the extrema of the response can be estimated to be at frequencies $\omega_r \simeq n\frac{\pi}{\tau}$, $n = 1, 2, 3, ...$

Recent experiments on modulated turbulence in a cylinder between two counter rotating disks [6] revealed evidence for the proposed response maxima. In accordance with the predictions from the mean-field theory [4], for small frequencies a constant response amplitude was measured. For large driving frequencies a $1/\omega$-decay of the velocity response amplitude was observed, again in agreement with the prediction from our mean-field approach. Note here, that both the velocity response as well as the energy response are the same up to a factor of two, in linear order, cf. Section 3.6. In the experiments the amplitude of the driving force rather than that of the energy input rate is modulated. Since the energy input rate is not a controlled quantity any more it can serve to measure the response of the system. Of course, also within the mean-field theory we can account for a modulated driving *force,* see [4]. The main features, the $1/\omega$-decay of the energy response amplitude for high frequencies and

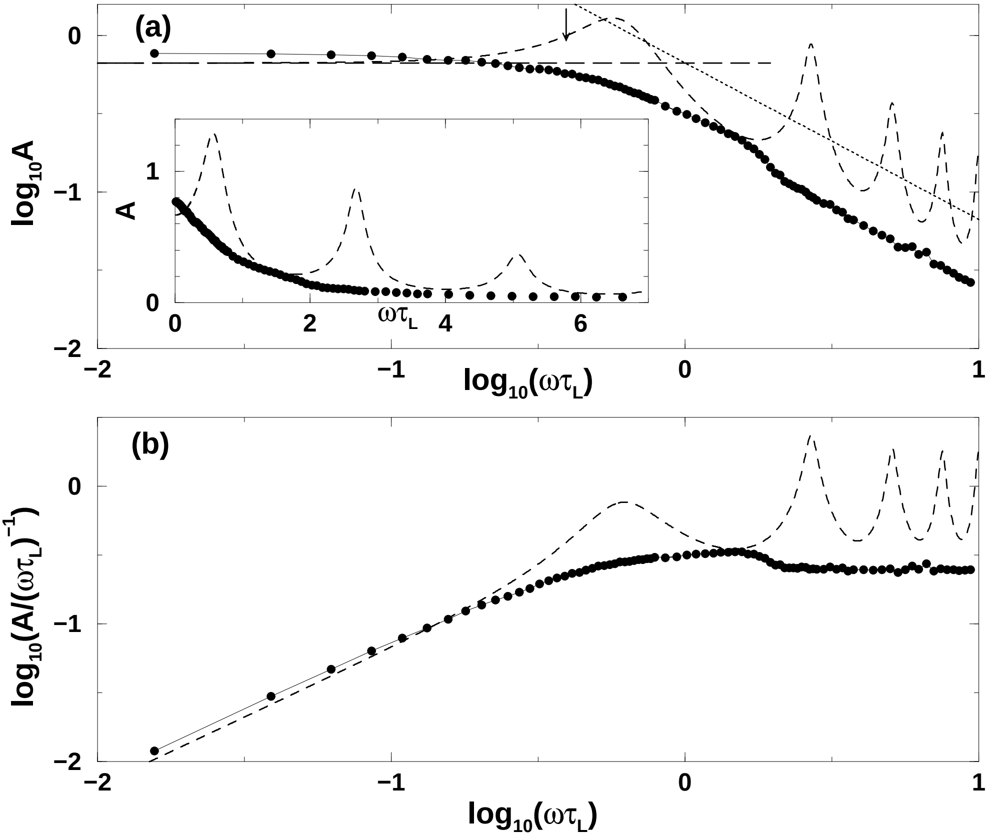

Figure 4.1: Response amplitude A as a function of the driving frequency ω for a modulated energy input rate $e_{in} = \epsilon_0(1 + e \sin \omega t)$ calculated within the GOY shell model (full dots), see Section 4.2.2. The modulation amplitude is set to $e = 0.2$, and the cascade time delay turned out to be $\tau/\tau_L = a = 2.54$. The stationary Reynolds number is $Re_0 = 7.1 \cdot 10^4$, the viscosity $\nu = 1.01875 \cdot 10^{-4}$, and the large eddy turnover time $\tau_L = 15.57$. Time and length units are set by ν, k_0 and F_0 in GOY. Our findings are compared with the response amplitude as calculated within the mean-field model with the same e and τ (dashed lines). (a) Log-log plot of the amplitude A versus frequency. The long-dashed line denotes the low frequency limit of the mean-field theory, $A \simeq 2/3$, and the dotted line the high frequency limit, $A \propto 2/(3\omega)$. The arrow denotes $\omega\tau_L = 1/a \simeq 0.39$. Near to this frequency the crossover takes place in GOY. Inset: linear scale plot of the response amplitude. (b) Log-log plot of the amplitude compensated by the asymptotic amplitude, i.e., $A/(\omega\tau_L)^{-1}$ versus frequency. A clear maximum is observed in GOY at a frequency near to the maximum of the mean-field amplitude.

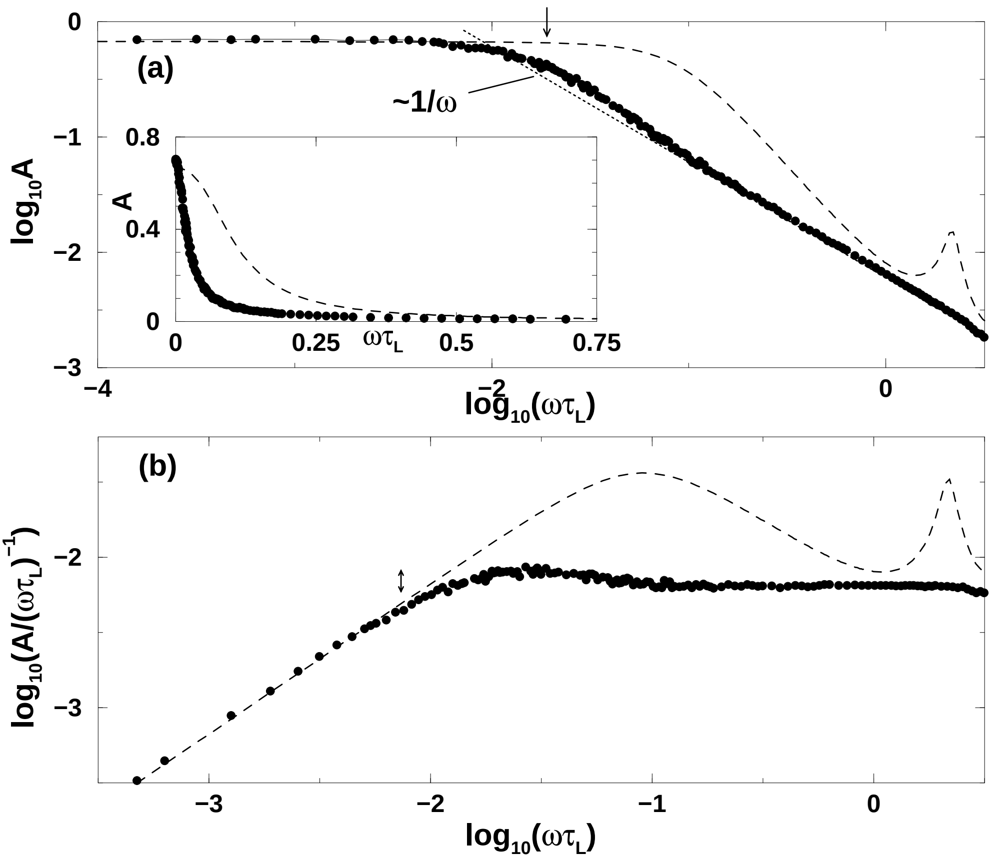

Figure 4.2: Response amplitude A as a function of the driving frequency ω for a modulated energy input rate $e_{in} = \epsilon_0(1 + e \sin \omega t)$ calculated within the REWA model (full dots), see Section 4.3.2. The modulation amplitude is set to $e = 0.3$, and the cascade time scale results to be $\tau/\tau_L = a = 2.94$. The Kolmogorov constant is found to be $b = 83.5$ in this simulation instead of $b_{exp} = 6 - 9$. The stationary Reynolds number is $Re_0 = 1.2 \cdot 10^5$, the viscosity $\nu = 5 \cdot 10^{-5}$, and the large eddy turnover time $\tau_L = 0.063$. Times are measured in units of $L_0^{2/3} \epsilon_0^{-1/3}$ in REWA. The result is compared with the response amplitude as calculated within the mean-field model with the same e, τ, and b (dashed lines). (a) Log-log plot of the amplitude A versus frequency. The dotted line is $\propto 1/\omega$. The arrow indicates the mean-field crossover frequency $\omega_{cross}^{MF} \tau_L = (6/b)^{3/2} = 0.019$. Inset: linear scale plot of the response amplitude. (b) Log-log plot of the compensated amplitude, i.e., $A/(\omega\tau_L)^{-1}$ versus frequency. A clear maximum is observed in REWA at a frequency near to the first maximum of the mean-field amplitude. The arrow indicates the height of the maximum, i.e., a deviation from the $1/\omega$-decay by a factor of 1.4 in REWA.

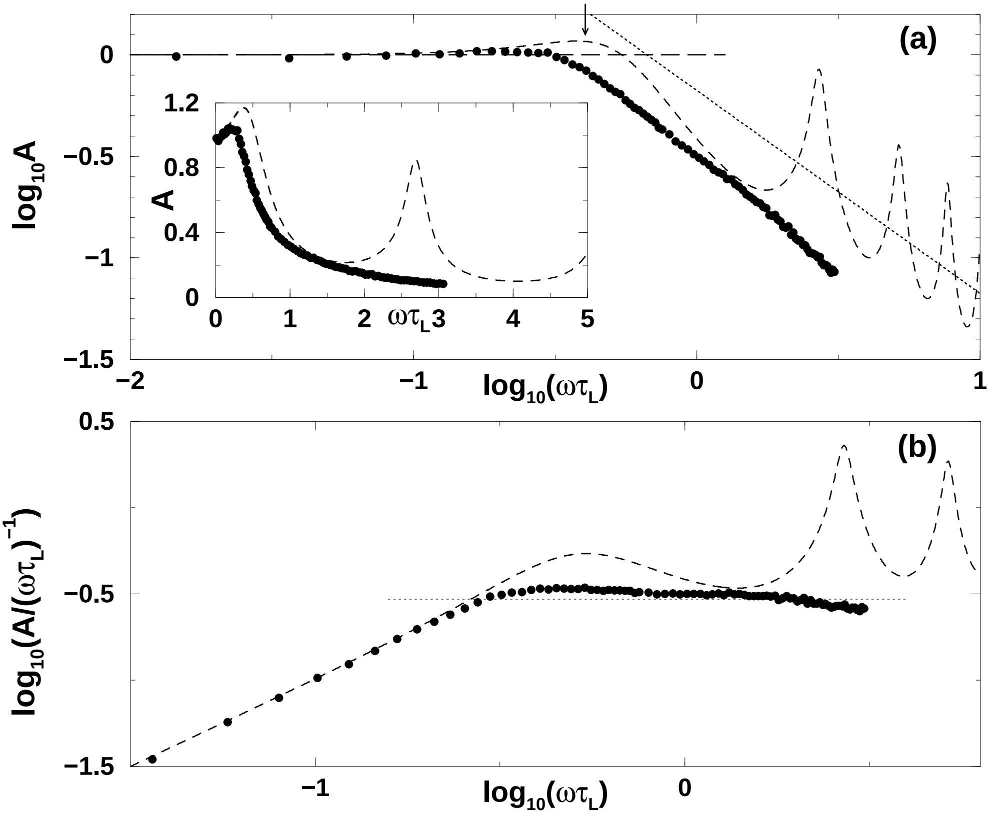

Figure 4.3: Response amplitude A as a function of the driving frequency ω for a modulated driving force $F = F_0(1 + e\sin\omega t)$ calculated within the GOY shell model (full dots), see Section 4.2.3. The modulation amplitude is set to $e_f = 0.2$, and the cascade time scale is found to be $\tau/\tau_L = a = 2.48$. The stationary Reynolds number is $Re_0 = 8.6 \cdot 10^4$, the viscosity $\nu = 1.01875 \cdot 10^{-4}$, and the large eddy turnover time $\tau_L = 14.5$. The result is compared with the response amplitude as calculated within the mean-field model with the same e and τ (dashed lines). (a) Log-log plot of the amplitude A versus frequency. The long-dashed line denotes the low frequency limit of the mean-field theory, $A \simeq 1$, and the dotted line the high frequency limit, $A \propto 2/(3\omega\tau_L)$. The arrow denotes $\omega\tau_L = 1/a \simeq 0.40$. Near to this frequency the crossover takes place in GOY. Inset: linear scale plot of the response amplitude. (b) Log-log plot of the compensated amplitude, i.e., $A/(\omega\tau_L)^{-1}$ versus frequency. The dotted line denotes $A/(\omega\tau_L)^{-1} \propto$ const.

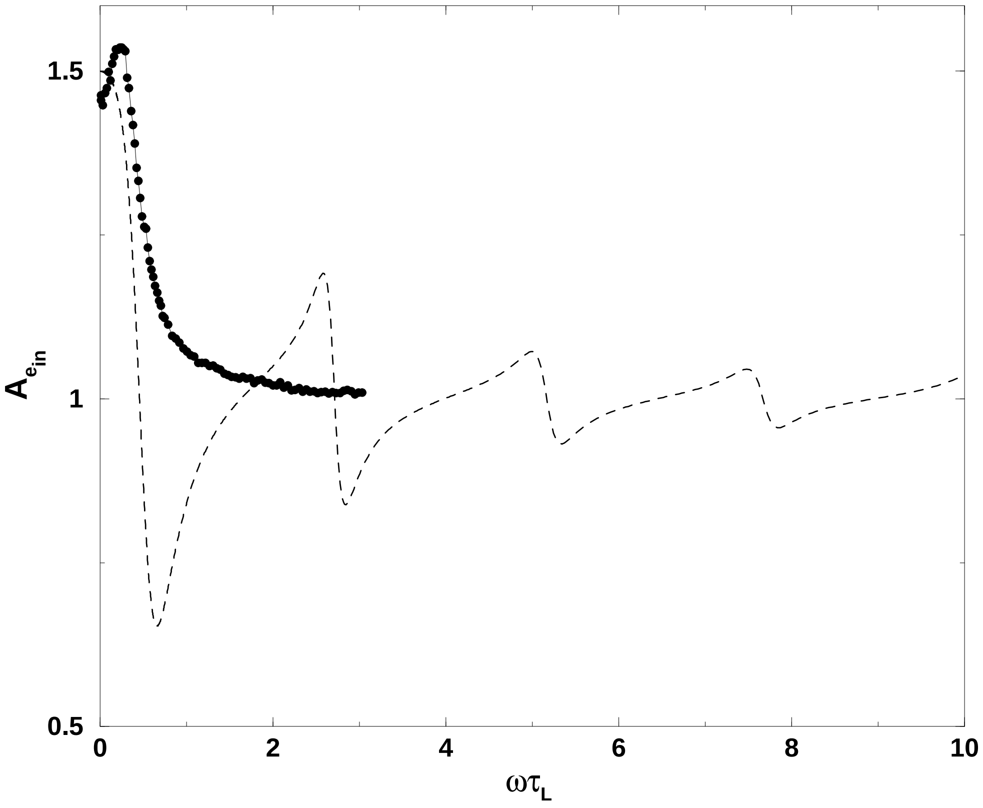

Figure 4.4: Linear scale plot of the energy input amplitude $A_{e_{in}}$ as a function of the driving frequency ω for a modulated driving force $F = F_0(1 + e \sin \omega t)$ calculated within the GOY shell model (full dots), see Section 4.2.3. For the parameters see Fig.4.3. The result is compared with the response amplitude as calculated within the mean-field model with the same e and τ (dashed line). The mean-field amplitude as well as the GOY amplitude start for low ω with $A_{e_{in}} \simeq 1.5$ and merge at $A_{e_{in}} \simeq 1$ for high frequencies. The GOY amplitude shows only the first main maximum.

the constant response amplitude for low frequencies, pertain. The response maxima are only slightly shifted in comparison with the case of a modulated energy input rate. In the case of a modulated driving force, as in the experiments, the energy input rate as a response of the system, also shows maxima in addition to the mentioned mean features. These are at the same frequencies as the maxima of the total energy response amplitude.

In the mean-field approach, the (intermittent) fluctuations of the energy and, in particular, of the cascade time τ are not present. In experiments and numerical simulations these fluctuations are of course present, and they may lead to broader and less pronounced response maxima and minima. Therefore, in this chapter we shall study the frequency dependence of the response to a modulated energy input rate into a system where turbulent fluctuations are included. In particular, we shall address the question whether the response maxima and minima can still be well identified in the presence of fluctuations. Furthermore, we not only consider a modulated energy input rate, but also discuss the slightly different case of a modulated driving force in order to compare with the above mentioned experiments.

An appropriate way to numerically study the problem of modulated turbulence would be a direct numerical simulation of the Navier-Stokes equation for this specific time-dependent energy input rate. However, as we need high Reynolds numbers to achieve fully developed, isotropic, and homogeneous turbulence and, in addition, need the response of the system as a function of time for a wide range of driving frequencies, the computational demands would be too high. Therefore, we first study the problem within a dynamical cascade model of turbulence, the Gledzer-Ohkitani-Yamada (GOY) shell model [7–14]. With this model large Reynolds numbers and enough statistics within a reasonable computing time for each driving frequency can be achieved. The GOY model has been successfully used in a study about decaying and kicked turbulence [15]. In addition, to be even closer to a numerical Navier-Stokes simulation and to distinguish between real effects and artifacts of the turbulence model, we follow another approach. We calculate the response of the system to a modulated energy input rate within a reduced wave vector set approximation (REWA), [16–18], where the Navier-Stokes equation is solved on a reduced, geometrically scaling subset of wave vectors. This method is much closer to the Navier-Stokes dynamics than the GOY-model, as it contains (i) much more modes than GOY, (ii) it solves the Navier-Stokes equation for those modes and not only a model equation, and (iii) it is three dimensional.

Our main results are summarized in Figs. 4.1, 4.2, 4.3, and 4.4. In Figs.4.1 and 4.2, the amplitude A of the energy response is shown as a function of the driving frequency for both the GOY model (Fig.4.1) and the REWA simulation (Fig.4.2) with a modulated energy input rate. This is compared with the results of the mean-field model with the corresponding parameters, i.e, the same modulation amplitude e and time scale τ. In Figs.4.3 and 4.4 the results from the GOY model solutions are shown for a modulated driving force and compared with the mean-field model. In all cases we observe a constant amplitude for low driving frequencies and a $1/\omega$-decay for high frequencies. This can in particular be observed in the compensated plots (parts b of all three figures), where A, compensated by its asymptotic amplitude, i.e., $A/(\omega\tau_L)^{-1}$, is plotted versus frequency. The $1/\omega$-decay of the response means, that for fast modulation no response is detectable any more. The remaining dissipation rate is that of the stationary system itself.

In the mean-field approach, a sequence of response maxima is present for both types of forcing, starting at a frequency $\omega \propto 1/\tau$. In the simulations, this main maximum can also be observed, although it is weaker and broader, i.e., it is "washed out" by fluctuations. The higher order maxima and minima are not visible in the simulations, but are completely washed out by fluctuations. On the other hand, we emphasize that the turbulent fluctuations in the GOY model are strongly overestimated due to the extreme mode reduction in this model. In the REWA simulation, an artificially large Kolmogorov constant b, indicating that still the fluctuations are stronger than in the Navier-Stokes dynamics, is found. Using such large b in the mean-field approach also leads to a considerable weakening of the first maximum and a shrinking of the higher order maxima and minima towards very small amplitudes.

These results will be explained and discussed in detail in this chapter, which is organized as follows. In the next section we study the modulated turbulence within the GOY shell model. Before calculating the response of the system to a modulated energy input rate as well as a modulated forcing in Section 4.2.2 and 4.2.3 we briefly introduce the model and study its stationary properties in Section 4.2.1. In Section 4.3 we present our findings on modulated turbulence within the reduced wave vector set approximation. We summarize our results in Section 4.4.

4.2 Modulated turbulence in the GOY shell model

4.2.1 Stationary properties

The GOY shell model consists of a set of coupled ODEs for one-dimensional complex velocity modes u_n [7–14]. These modes u_n correspond to velocity *differences* $|\boldsymbol{u}(\boldsymbol{x}+\boldsymbol{r}_n)-\boldsymbol{u}(\boldsymbol{x})|$ on scale r_n. N modes are taken into account, $n = 1, 2, ..., N$, one complex velocity mode per cascade level n, defined by the wave numbers $k_n = \lambda^n k_0$ which are equally spaced on a logarithmic scale, here, $\lambda = 2$. The model equations read:

$$\begin{aligned}\left(\frac{d}{dt} + \nu k_n^2\right) u_n &= i(ak_n u_{n+1}^* u_{n+2}^* + bk_{n-1} u_{n-1}^* u_{n+1}^* \\ &\quad + ck_{n-2} u_{n-1}^* u_{n-2}^*) + F\delta_{n,1}, \qquad (4.2)\end{aligned}$$

where $n = 1, ..., N$, $a = 1$, $b = -1/4$, and $c = -1/2$. These are the traditional parameters. We impose boundary conditions on the u_n, i.e., $u_n = 0$ for $n < 1$ or $n > N$. We use $N = 14$ shells, a viscosity of $\nu = 1.01875 \cdot 10^{-4}$, and $k_0 = 2^{-4}$. The forcing acts on the largest scale, i.e., the first shell, $n = 1$. F is constant, $F = F_0 = (1 + i) \cdot 10^{-2}$. Together with ν and k_0 this sets the time and length units as well as the Reynolds number. Eqs. (4.2) are integrated using a fourth order Runge-Kutta scheme with adaptive step size [19].

With the above chosen parameters the GOY dynamics is chaotic [14]. The system is forced on large scales while most of the energy is dissipated on small scales. It reaches a steady state, in which the velocities are stochastically fluctuating. In this sense the system has similar properties as three dimensional Navier-Stokes turbulence. The scaling behavior of structure functions and dissipation has been extensively studied in [11–14, 20–22]. The deviations from K41 scaling due to intermittency observed in the GOY model are very similar to experimental values. Most of the previous studies have been done with 22 or more shells. As we use here only 14 shells in order to reduce the computational effort we explicitly check some scaling properties of, e.g. the structure functions and the energy spectrum in a simulation with constant, stationary forcing $F = F_0$ in Eq. (4.2). $N = 14$ then turns out to be sufficient.

The Reynolds number of the system can be defined as follows. An outer length scale L is given by the smallest wave number k_1, $L = 1/k_1$. A typical velocity U is the velocity on that scale, $\langle\langle |u_1|^2 \rangle\rangle_t^{1/2}$. The average $\langle\langle ... \rangle\rangle_t$ is taken over time. With these length and velocity scales the Reynolds number of the present simulation is $Re_0 = \frac{UL}{\nu} = 8.6 \cdot 10^4$. The simulated time interval is several hundreds of large eddy turnover times $|k_1 u_1|^{-1}$.

For the second order structure function we use the following method. In [11] it has been suggested to study the scaling of

$$\Sigma_{n,q} = \langle\langle |\Im(u_n u_{n+1} u_{n+2} + \left(\frac{1-\epsilon}{\lambda}\right) u_{n-1} u_n u_{n+1})|^{q/3} \rangle\rangle, \tag{4.3}$$

instead of the pure moments of the velocity $s_{n,q} = \langle\langle |u_n|^q \rangle\rangle$ in order to eliminate the period 2 and period 3 oscillations which are an artifact of the GOY model. The second order quantity $\Sigma_{n,2}$, corresponding to the second order structure function, is shown in Fig.4.5 as a function of wave number index $n = \log_2(k_n/k_0)$. One clearly observes an inertial subrange (ISR) between shell 2 and 9, where the second order structure function shows scaling with an exponent near to the K41 value 2/3, i.e., $\Sigma_{n,2} \propto k_n^{-0.71}$ corresponding to $\propto r^{0.71}$ for the structure function. The scaling exponent is not equal to the K41 value, because the model shows intermittency corrections. The higher wave numbers, i.e., smaller scales, $n = 12-14$ belong to the viscous subrange (VSR), where dissipation takes place. In this range the viscosity term is dominant and the velocity decays rapidly with k_n, in fact more than exponentially [21, 22]. The external forcing of the flow acts on shell $n = 1$, therefore the stirring subrange (SSR) contains the first shell only. The spectrum, which is obtained by fast Fourier transforming (FFT) a time series of the velocity $u(t) = \sum_n \langle\langle Re(u_n(t)) \rangle\rangle$ and raising it to the power two, can be compared to the energy spectrum under the assumption of the Taylor hypothesis. This spectrum is shown in Fig.4.6 for $N = 14$. We observe about one frequency decade of (nearly) Kolmogorov scaling, where the energy decays as $\propto f^{-5/3}$ with frequency f. For $N = 14$ the Kolmogorov scaling range is not yet

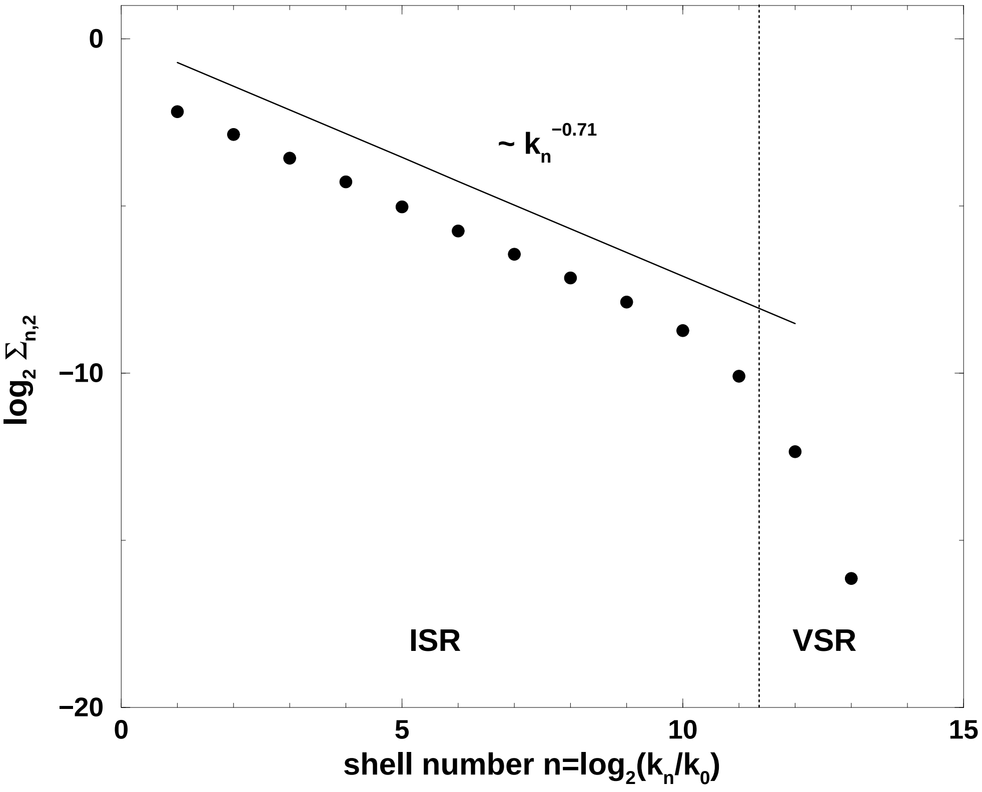

Figure 4.5: Second moment $\Sigma_{n,2} = \langle\langle|\Im(u_n u_{n+1} u_{n+2} + \left(\frac{1-\epsilon}{\lambda}\right) u_{n-1} u_n u_{n+1})|^{2/3}\rangle\rangle$ (full dots) corresponding to the second order velocity structure function as a function of wave number $k_n = 2^n k_0$, averaged over a long time interval (t=1400τ_L) and with a stationary, constant forcing, $F = F_0$. Between shell 2 and 9 ISR-scaling behavior, $\Sigma_{n,2} \propto k_n^{-0.71}$ (solid line) is observed, whereas the shells 12-14 form the VSR. $\Sigma_{14,2}$ is zero by definition. The dotted line indicates the middle of the crossover region between the ISR and the VSR.

well developed. For less shells this region becomes even narrower and the spectrum shows strong peaks at some intrinsic frequencies. When reducing the number of shells even more, the velocities relax to a stationary value without any fluctuations, i.e., the chaotic behavior of the system is lost.

In conclusion, the GOY model with $N = 14$ shells exhibits an inertial subrange scaling, although the ISR for the frequency spectrum is only narrow, but the spectrum in k-space has a scaling range of about three orders of magnitude. This seems acceptable for our goal to study the response of the system to a modulated driving, because we are only interested in global quantities like the total energy $E(t)$ but do not need information on scale resolved quantities.

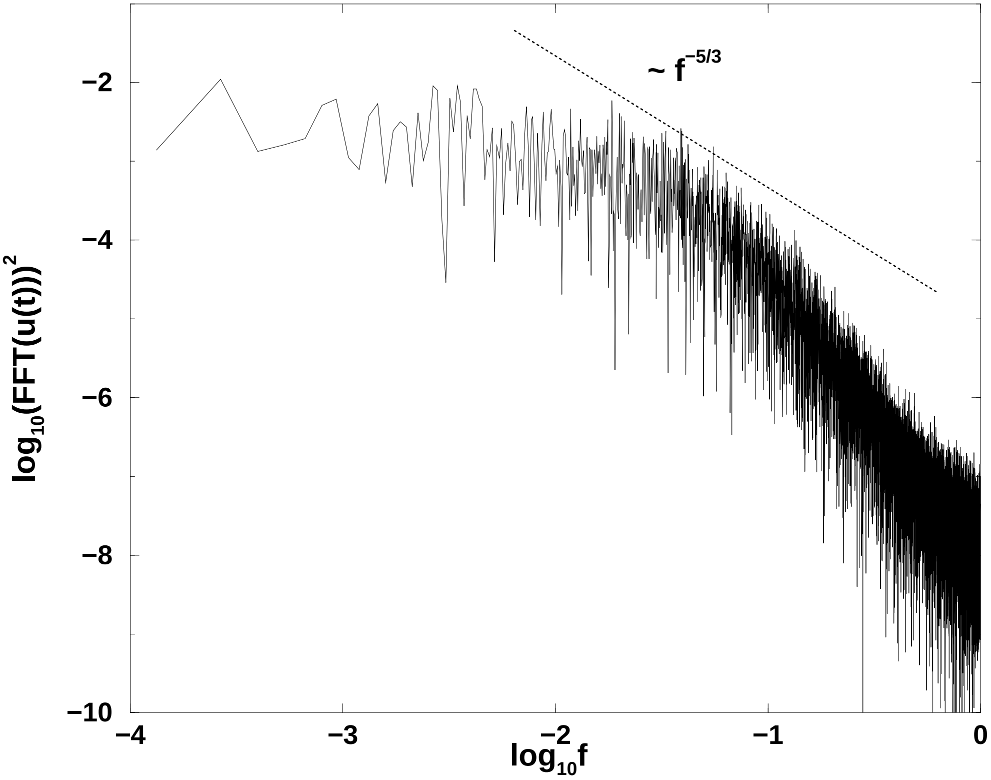

Figure 4.6: Energy frequency spectrum of the GOY-system with a stationary, constant forcing $F = F_0$. The spectrum is obtained by fast Fourier transforming (FFT) an actual time series of the velocity $u(t) = \sum_n \langle\langle Re(u_n(t))\rangle\rangle$. About one frequency decade of Kolmogorov scaling $\propto f^{-5/3}$ is observed. In k-space the scaling regime of the spectrum is more extended, i.e., about three decades, as has been already shown in Fig.4.5.

Time scales of the GOY model

The time scales in the model have been determined as follows. For each shell n an eddy turnover time τ_n is defined by [11]:

$$\tau_n = \frac{1}{|u_n k_n|}. \tag{4.4}$$

This is also considered as the time scale for the turbulent energy transfer through the nth level. The time scale relevant for the energy loss on level n due to viscosity is defined as

$$\tau_n^d = \frac{1}{\nu k_n^2}. \tag{4.5}$$

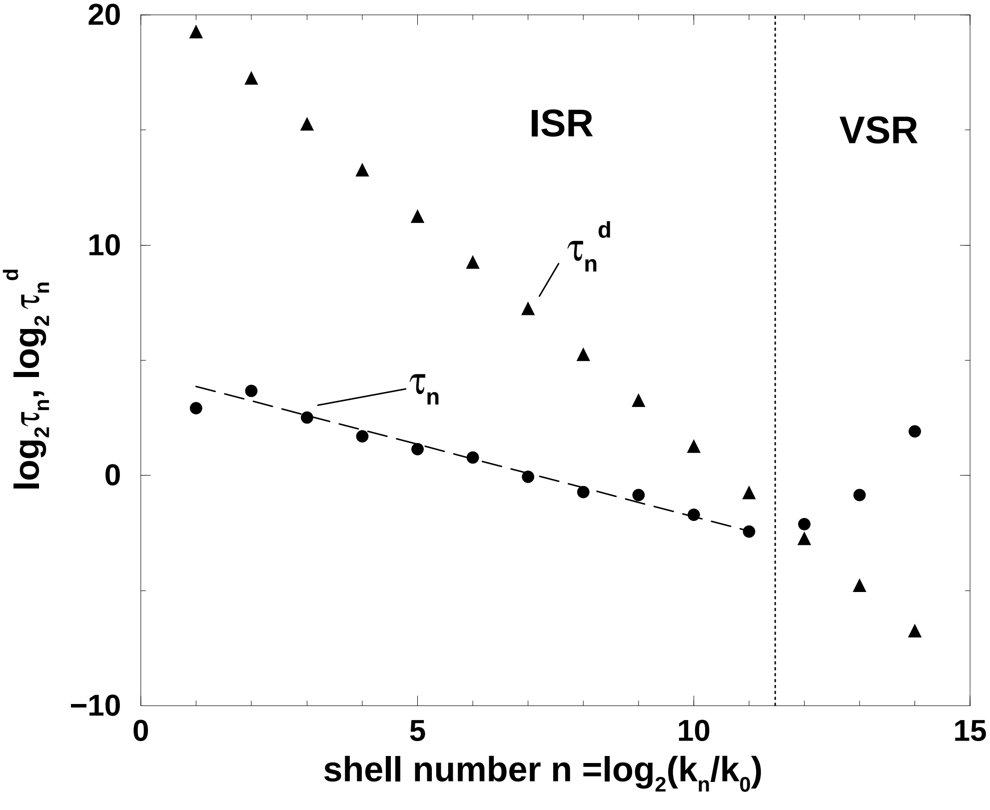

Figure 4.7: Characteristic time scales of the turbulent energy transfer τ_n (full dots) and of the viscous dissipation τ_n^d (full triangles) as functions of the level number n in the GOY system. The dashed line is a linear fit of $\log_2 \tau_n$, $n = 2, ..., 11$, and gives $\tau_n^{fit} = 22.46 \cdot 2^{-0.63n}$. The shown τ_n and τ_n^d are obtained by averaging over 1400 large eddy turnover times. The dotted line indicates the middle of the crossover region between the ISR and the VSR.

Both time scales are shown in Fig.4.7.

In the ISR between shell 2 and 9, where the energy transfer times are the relevant time scales for the dynamics, the decrease of the τ_n with n is near to $\tau_n \propto 2^{-2n/3}$ (dashed line in Fig.4.7) as expected for the turnover times of eddies of sizes $r_n/L \propto (1/2)^n$. In this range the dissipation time scales τ_n^d are much larger than the τ_n, meaning that the turbulent energy transfer is much faster than the viscous dissipation, and therefore the dominant process. In the VSR instead $\tau_n^d < \tau_n$, i.e., on average the energy is dissipated by viscosity before it can be transferred to smaller scales.

The largest eddy's turnover time is in general defined by the velocity on the outer length scale L, i.e., on the length scale of the forcing, which in this case is $1/k_1$.

However, in this model, the time τ_1 is disturbed due to finite size effects. Therefore, we extrapolate from the turnover times of the other shells. A linear fit in Fig.4.7 for $\log_2 \tau_n$ with $n = 2, ..., 11$ leads to $\tau_n^{fit} = 22.46 \cdot 2^{-0.63n}$. Without intermittency one would have $\tau_n \propto 2^{-2n/3}$; the small deviation corresponds to the intermittent scaling of $u_n \propto k_n^{0.37}$ or an intermittency correction of $\delta\xi = \xi_1 - 1/3 = 0.04$. The extrapolation for $n = 1$ yields for the large eddy turnover time $\tau_L = \tau_1^{fit} = 14.5$. The time scale corresponding to the energy transfer time τ used in the mean-field model [4] is the sum over the eddy turnover times of all energy-input and inertial-range shells, i.e., here $\tau \simeq \sum_{n=1}^{11} \tau_n \simeq 35.9$. The factor $\tau/\tau_L = a$ between the transfer time and the large eddy turnover time is then $a = 2.48$.

Constant energy input rate

Until now, we have considered a constant forcing $F = F_0$. The resulting energy input rate $e_{in}(t) = \langle\langle u_1^*(t) F_0 \rangle\rangle$ then fluctuates around its mean value because of the $u_1^*(t)$-fluctuations. In the mean-field theory [5] the energy input rate e_{in} is constant instead. For closer comparison we also consider another type of forcing in the GOY-model: $F(t) = \epsilon_0 u_1(t)/|u_1(t)|^2$. This forcing $F(t)$ fluctuates as $u_1(t)$. Then the energy input rate is $e_{in} = \langle\langle u_1^* F \rangle\rangle = \epsilon_0 = const$ by definition. The ISR-scaling behavior as well as the energy spectrum then turn out to be similar to the previously discussed ones with the constant forcing $F = F_0$. The energy transfer time τ is slightly larger in this case, namely $\tau = 39.5$, and the large eddy turnover time is $\tau_L = \tau_1^{fit} = 15.57$. Again, the large eddy turnover time is extrapolated from $\tau_2, ..., \tau_{11}$. This leads to the factor $\tau/\tau_L = a = 2.54$ between the total time delay of the energy cascade and the large eddy turnover time. In the following sections we will study the time-dependent cases where either the energy input rate e_{in}, i.e., $F = \epsilon_0 \frac{u_1}{|u_1|^2}$ (Section 4.2.2) or the forcing $F = F_0$ is modulated (Section 4.2.3).

4.2.2 Modulated energy input rate

In this section we apply a modulated energy input rate to the GOY model, i.e., we set the forcing $F = F(t)$ in equation (4.2) as

$$F(t) = \epsilon_0 \frac{u_1}{|u_1|^2}(1 + e \sin \omega t) \tag{4.6}$$

with a modulation amplitude $e = 0.2$. Then, the resulting energy input rate e_{in} is

$$\begin{aligned} e_{in}(t) &= \langle\langle u_1^*(t) F(t) \rangle\rangle, \\ &= \epsilon_0 (1 + e \sin \omega t), \end{aligned} \tag{4.7}$$

and has a prescribed modulation amplitude $e\epsilon_0$ by definition. The total energy of the system

$$E(t) = \frac{1}{2}\sum_{n=1}^{14}\langle\langle u_n^*(t)u_n(t)\rangle\rangle, \tag{4.8}$$

is calculated for a wide range of driving frequencies ω in order to study the frequency behavior of the response. The brackets $\langle\langle ... \rangle\rangle$ denote the ensemble average. This ensemble average is performed as follows. From a long stationary simulation we collect an ensemble of 1500 starting configurations which we then let evolve according to Eqs.(4.2) but now including the modulation of the forcing $F(t)$, Eq.(4.6), and average over these 1500 time series. To ensure that the different realizations can be considered as statistically independent, the time delay between the successive starting configurations for the different realizations is chosen to be about 100 large eddy turnover times. The adaptive step size routine controlling the Runge-Kutta integration algorithm for ODEs does not produce the same time steps for all time series. To overcome this, we have calculated also the same number of equidistant time steps by spline interpolation for all time series.

The oscillating response of the system $\Delta(t)$ is then studied in terms of the ratio between the energy $E(t)$ with modulated energy input and the energy $E_0(t)$ without modulation, namely

$$E^{norm}(t) = \frac{E(t)}{E_0(t)} = 1 + \Delta(t). \tag{4.9}$$

E and E_0 both are averaged over 1500 realizations. In spite of the averaging not only E but also E_0 still contains (weak) fluctuations. Therefore, we write $E_0(t)$, as E_0 is still slightly fluctuating around its mean value. Accordingly, the energy input rate e_{in} is normalized by its stationary value, $e_{in}^{norm}(t) = \frac{e_{in}(t)}{\epsilon_0} = 1 + e\sin\omega t$.

In Fig.4.8 the input rate $e_{in}^{norm}(t)$ and the energy $E^{norm}(t)$ are plotted for four different driving frequencies. For the two low frequencies where $\omega\tau_L \ll \tau_L/\tau = 1/a \simeq$0.39, the energy follows the oscillation of the energy input rate with almost constant, but smaller amplitude. For higher frequencies the amplitude of the deviationsof the normalized energy from its stationary value 1 strongly decreases, and a phase shift with respect to the energy input becomes visible. The same behavior of the energy has been observed in the mean-field theory [4].

To quantitatively access the frequency behavior of the response amplitude, we calculated time series of the total energy $E(t)$ for 85 different driving frequencies varying over almost 3 decades between $0.012 \le \omega\tau_L \le 9.3$. The chosen frequencies are approximately equally spaced on a logarithmic scale. The normalized energy $E^{norm}(t)$ is fitted by a function of the form

$$E^{norm}(t) = E_{const} + eA\sin(\omega t + \Phi), \tag{4.10}$$

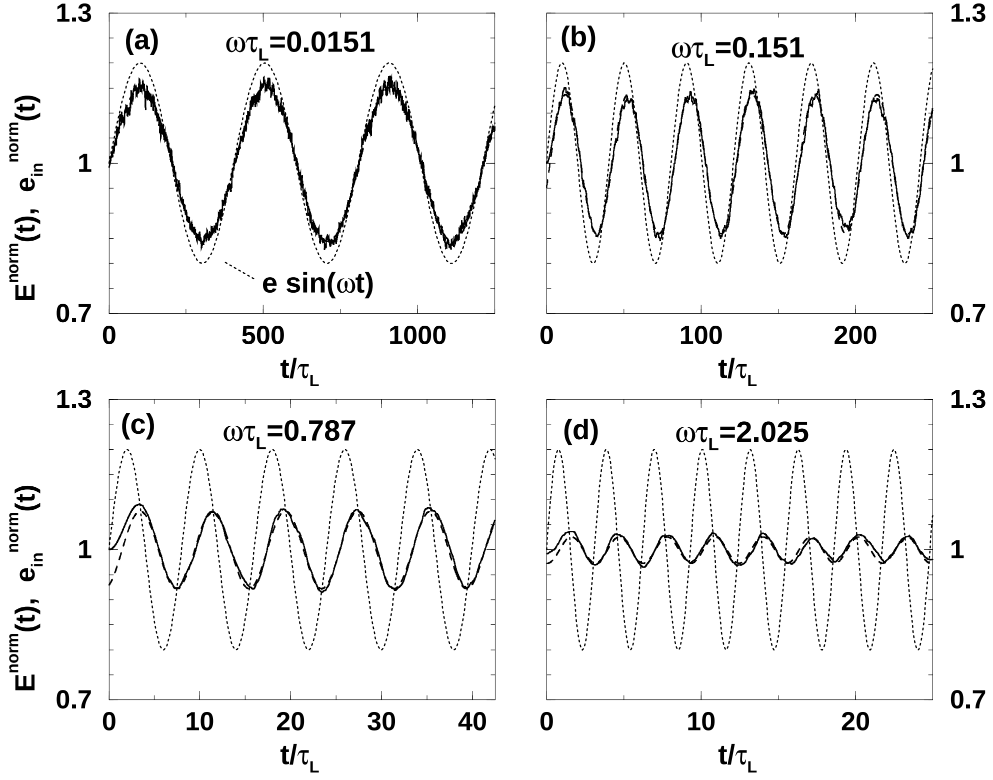

Figure 4.8: Energy input rate $e_{in}^{norm} = e_{in}/\epsilon_0$ (dotted lines) and energy content E^{norm} (solid lines) for four different modulation frequencies ω calculated in the GOY model. The energy input rate e_{in} is modulated with a modulation amplitude of 20% of the constant energy input rate ϵ_0, $e = 0.2$, according to Eq.(4.7). Also included is the fit according to Eq.(4.10) for the energy E^{norm} (dashed lines, indistinguishable from the solid lines). (a) $\omega\tau_L = 0.0151$, (b) $\omega\tau_L = 0.151$, (c) $\omega\tau_L = 0.787$, (d) $\omega\tau_L = 2.025$.

with three free parameters: E_{const}, the amplitude A, and the phase shift Φ. E_{const} is near to 1 for all frequencies, i.e., $E_{const} = 1.0022 \pm 0.0032$. The fits (4.10) are included in Fig.4.8 as dashed lines but they are mostly indistinguishable from the solid lines for the energy itself.

Fig.4.1 of Section 4.1 shows the amplitude A, resulting from the fitting procedure, as a function of the dimensionless frequency $\omega\tau_L$. A is almost constant for low frequencies and has a value of about $\frac{2}{3}$. For higher frequencies the amplitude decreases as $\propto 1/\omega$. The same features have been observed in the mean-field calculations, see dashed lines. The long-dashed line in Fig.4.1 represents the low frequency limit of the mean-field theory, $A \simeq 2/3$, and the dotted line the high frequency limit, $A \propto 2/(3\omega\tau_L)$.

The crossover between the regime of constant amplitude and the one of $1/\omega$-decay of the energy response takes place at $\omega_{cross}\tau_L \simeq 1/a$ $\simeq$0.39, which is indicated by the arrow in Fig.4.1. In the mean-field approach this crossover is always at $\omega\tau_L =$ 1, independent of the factor a between the large eddy turnover time and the total time scale of the energy transfer. In experiments [6] the crossover frequency has been used to measure the energy cascade time scale. The present simulations confirm that this frequency gives the correct order of magnitude for the energy transfer time.

Response maxima, as observed in the mean-field model at frequencies connected with the inverse energy transfer time, are difficult to be identified in Fig.4.1a. There is some structure visible at $\omega\tau_L \simeq 0.31$ and $\omega\tau_L \simeq 1.57$. In Fig.4.1b, where the amplitude A compensated by the asymptotic amplitude $(\omega\tau_L)^{-1}$, i.e., $A/(\omega\tau_L)^{-1}$ is plotted versus frequency, this structure becomes more evident, and we see a clear maximum at a frequency of about $\omega\tau_L \simeq 1.57$. This maximum probably corresponds to the mean-field maximum. Of course, the maximum in GOY is broadened and weakened due to the large fluctuations, and the higher order maxima and minima are apparently washed out completely. As in the mean-field theory no fluctuations are included, the energy cascade time τ is considered to be constant. However, in the GOY model this assumption is not true, as can clearly be seen in Fig.4.9. Here, a time series of the cascade time $\tau(t) = \sum_{n=1}^{11} \tau_n(t)$ is plotted, computed within the GOY-shell model with non-modulated forcing $F = \epsilon_0 \frac{u_1}{|u_1|^2}$. The inset shows the probability distribution of τ/τ_L. This distribution has its maximum at $\tau/\tau_L = 2.39$, almost at the mean cascade time $a = 2.54$, and a width (FWHM/2) of about $0.46a$. The width is almost half the size of the mean which indicates that the transfer time fluctuates strongly and therefore we have to expect that the response maxima are more or less washed out. However, these strong fluctuations are considered as an artifact of the GOY-model and not as a feature of real turbulence. The GOY-model contains only one velocity mode per cascade level instead of infinitely many modes in real turbulence. This one-mode approximation leads to an overestimation of the fluctuation strength. In order to confirm this, we performed another simulation with more modes per level within the reduced wave vector set approximation (REWA) of the Navier-Stokes equation. This will be presented in Section 4.3.

4.2.3 Modulated driving force

In this section we present further results within the GOY model based on a non-fluctuating driving force F_0 which is regularly modulated as was ϵ_0 in the previous section. This case may be more comparable to the experimental method in reference [6], because there the driving force is modulated. What cannot be modeled with GOY

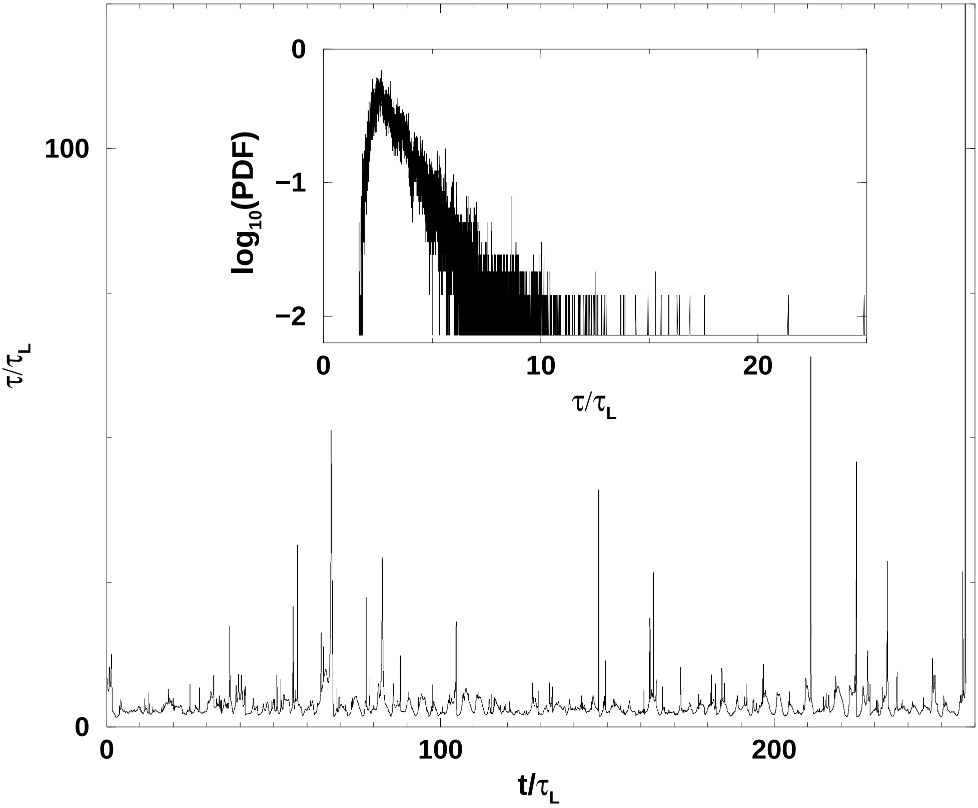

Figure 4.9: Time series of the cascade time $\tau(t)$ for non-modulated forcing $F = \epsilon_0 u_1/|u_1|^2$ in the GOY model. Strong fluctuations are observed. Inset: Probability distribution of τ/τ_L. The mean is $a = 2.54$, and the width FWHM/2=$0.46a$ giving about 50% fluctuations.

is the spatial inhomogeneity in the experiments [6].

In equations (4.2) we now apply a forcing

$$F = F(t) = F_0(1 + e_f \sin \omega t), \tag{4.11}$$

with a modulation amplitude of $e_f = 0.2$. As in Section 4.2.2 we calculate the ensemble averaged time series of the energy input rate $e_{in}(t)$, see first line of equation (4.7), and the total energy of the system $E(t)$ cf. equation (4.8) for 89 different frequencies between $0.0144 \leq \omega\tau_L \leq 3.04$, again logarithmically equally distributed. The normalized energy $E^{norm}(t)$ and energy input rate $e_{in}^{norm}(t)$ are then fitted by a function according to equation (4.10), with the parameters E_{const}, A, Φ, and $e_{in,const}$, $A_{e_{in}}$, $\Phi_{e_{in}}$, respectively.

The amplitudes A and $A_{e_{in}}$ are plotted in Figs.4.3 and 4.4 of Section 4.1, respectively, as a function of the dimensionless frequency $\omega\tau_L$. Also in this case of a modulated force, the response amplitude is almost constant for small frequencies, namely $A \simeq 1$, and decreases as $1/\omega$ for high frequencies, see Fig.4.3a (full dots). Again, the long-dashed line represents the low frequency limit of the mean-field theory for A (which is $A \simeq 1$ in this case) as well as the dotted line the high frequency limit. As in the previous section, the crossover frequency between the two regimes is determined by the energy transfer time, i.e., $\omega_{cross}\tau_L \simeq 1/a \simeq 0.40$ (as $a = 2.48$ in this case), which is marked by the small arrow in Fig.4.3a. The amplitude of the energy input rate $A_{e_{in}}$ starts with a value of about 1.5 for low frequencies and merges towards 1 for high frequencies, see Fig.4.4. This indicates that at very large frequencies the velocity is not oscillating any more as it only feels a mean constant force. The oscillations of the energy input rate are then only a consequence of the oscillation of the driving force F. In the mean-field theory we have observed the same trend for both amplitudes. The corresponding mean-field results are inlcuded as dashed lines.

Both amplitudes A and $A_{e_{in}}$ show a maximum at a frequency near to the crossover frequency $\omega\tau_L \simeq \tau_L/\tau = a^{-1} = 0.40$. In the compensated plot Fig.4.3b, where $A/(\omega\tau_L)^{-1}$ is plotted as a function of frequency, a clear deviation from the dotted line representing $A \propto 1/\omega$ can be observed. At this frequency, the mean-field theory predicts a first maximum for the energy response amplitude (Fig.4.3a) and a maximum directly followed by a minimum for the energy input rate, see Fig.4.4. This frequency is connected to the energy transfer time τ. In the mean-field model further maxima of the energy response and wiggles of the energy input rate are observed at multiples of this frequency. However, in the GOY model all further maxima and minima are washed out presumably because of the strong fluctuations. The fluctuations of the energy cascade time scale are found to be similar as in the case of a fluctuating force shown in Fig.4.9 in the previous section.

4.3 Modulated turbulence in the reduced wave vector set approximation

As was pointed out in the introduction of this chapter a full numerical simulation of the Navier-Stokes equation for modulated turbulence at high Reynolds numbers is still not possible or requires low Reynolds numbers. Therefore, we first have considered the GOY shell model. This model correctly describes many features of turbulence, however, due to the one-mode approximation in each cascade level, it contains various artifacts. Namely, it strongly overestimates the strength of the fluctuations. The aim of this section is to study the problem of modulated turbulence within another model, the reduced wave vector set approximation (REWA) [16–18], which is much closer to the Navier-Stokes equation than the GOY model and contains much more modes per cascade level. Of course, as compared to full numerical simulations of the Navier-Stokes equation, it still contains a mode reduction in order to make the computational effort reasonable for the desired high Reynolds numbers. The present approximation has been introduced and extensively studied in [16–18] . Here, we use it together with a time-dependent driving. For completeness we briefly explain the approximation before we present the results with modulated driving.

4.3.1 The reduced wave vector set approximation

The velocity field $\boldsymbol{u}(\boldsymbol{x},t)$ is Fourier transformed into plane waves,

$$\boldsymbol{u}(\boldsymbol{x},t)=\sum_{\boldsymbol{p}}\boldsymbol{u}(\boldsymbol{p},t)e^{i\boldsymbol{p}\cdot\boldsymbol{x}}. \tag{4.12}$$

Periodic boundary conditions are applied on a periodicity volume $(2\pi L_0)^3$. The wave vectors $\boldsymbol{p}$ are given by $\boldsymbol{p}=(p_i)=(n_i L_0^{-1})$, with $n_i=0,\pm1,\pm2,....$ In order to efficiently deal with the large number of modes involved, the reduced wave vector set approximation selects a limited number of modes by admitting only a geometrically scaling subset $K=\bigcup_l K_l$ of wave vectors, i.e., $\boldsymbol{u}(\boldsymbol{x},t)=\sum_{\boldsymbol{p}\in K}\boldsymbol{u}(\boldsymbol{p},t)e^{i\boldsymbol{p}\cdot\boldsymbol{x}}$. On this subset $K=\{\boldsymbol{p}_n^{(l)},n=1,...,N,\ l=0,...,l_{max}\}$ the Navier-Stokes equation for incompressible flow,

$$\begin{aligned}\frac{d}{dt}u_i(\boldsymbol{p}_n^{(l)}) &= -iM_{ijk}(\boldsymbol{p}_n^{(l)})\sum_{\boldsymbol{q}_1,\boldsymbol{q}_2\in K,\boldsymbol{q}_1+\boldsymbol{q}_2=\boldsymbol{p}_n^{(l)}}u_j(\boldsymbol{q}_1)u_k(\boldsymbol{q}_2)\\ &\quad -\nu(\boldsymbol{p}_n^{(l)})^2u_i(\boldsymbol{p}_n^{(l)})+f_i(\boldsymbol{p}_n^{(l)}),\end{aligned} \tag{4.13}$$

together with the continuity equation,

$$\boldsymbol{p}_n^{(l)}\cdot\boldsymbol{u}(\boldsymbol{p}_n^{(l)})=0, \tag{4.14}$$

is solved. M_{ijk} is the coupling matrix, $M_{ijk}(\boldsymbol{p})=\frac{1}{2}(p_jP_{ik}^{\perp}(\boldsymbol{p})+p_kP_{ij}^{\perp}(\boldsymbol{p}))$, where $P_{ij}^{\perp}(\boldsymbol{p})$ is the orthogonal projector to $\boldsymbol{p}$. The subset K consists of a basic subset $K_0=\{\boldsymbol{p}_n^{(0)},n=1,...,N\}$ together with its scaled replicas $\boldsymbol{p}_n^{(l)}=2^l\boldsymbol{p}_n^{(0)}$, $l=1,...,l_{max}$. In the present simulation we take $N=74$ wave vectors $\boldsymbol{p}_n^{(0)}$,

$$\begin{aligned}K_0= \quad &\{\pm(2,2,2),\pm(-1,2,2),\pm(-2,1,1),\pm(3,0,0),\\ &\pm(4,1,1),\pm(4,-2,1),\pm(-3,3,3),\pm(-5,1,1),\\ &\pm(4,4,1),\pm(3,3,0),\pm(1,1,10),\pm(-10,5,5)\\ &+\text{permutations}\}\end{aligned} \tag{4.15}$$

These wave vectors $\bigcup_l K_l$ are chosen such that they span a wide range of length scales, but still dynamically interact to a good degree. For the Navier-Stokes equation this means that as many Navier-Stokes interactions $\boldsymbol{p}=\boldsymbol{q}_1+\boldsymbol{q}_2$ as possible between the wave vectors in K are allowed for. The largest eddies of the order L_0 are represented by the wave vectors in K_0, whereas the subsets K_l contain wave vectors of smaller and smaller eddies. The choice of the smallest eddies, i.e., the value of l_{max}, depends on the kinematic viscosity ν. l_{max} and ν are adjusted such that the velocity amplitudes $\boldsymbol{u}(\boldsymbol{p}_n^{(l_{max})}, t)$ of the smallest eddies are almost zero. In this simulation, ν is chosen as $\nu = 5 \cdot 10^{-5}$ and the number of levels as $l_{max} + 1 = 9$.

To maintain the turbulent flow we apply a forcing as in [16–18]:

$$\boldsymbol{f}(\boldsymbol{p}, t) = \begin{cases} \epsilon_0 \frac{\boldsymbol{u}(\boldsymbol{p},t)}{\sum_{\boldsymbol{q} \in K_{in}} |\boldsymbol{u}(\boldsymbol{q},t)|^2} (1 + e \sin \omega t), & \text{for } \boldsymbol{p} \in K_{in} \\ 0, & \text{for } \boldsymbol{p} \notin K_{in}. \end{cases} \tag{4.16}$$

The subset K_{in} of K_0 by choice contains the wave vectors with the three smallest lengths. K_{in} contains 14 vectors, namely

$$K_{in} = \{\pm(2,2,2), \pm(-1,2,2), \pm(-2,1,1), \text{+permutations}\}. \tag{4.17}$$

In reference [17] it has been shown that the statistics of the solution the equation of motion do not depend on the particular choice of K_0. This forcing corresponds to the same type of forcing, which has already been applied to the GOY model in Section 4.2.2. It enforces the energy input rate to be modulated:

$$e_{in} = \langle\langle \sum_{\boldsymbol{p}_n^{(l)} \in K} \boldsymbol{u}^*(\boldsymbol{p}_n^{(l)}) \cdot \boldsymbol{f}(\boldsymbol{p}_n^{(l)}) \rangle\rangle = \epsilon_0 (1 + e \sin \omega t). \tag{4.18}$$

Eqs.(4.13) are a set of $3N(l_{max} + 1)$ coupled ODEs for the complex mode amplitudes $u_i(\boldsymbol{p}_n^{(l)})$ which is numerically solved within the Burlisch-Stoer integration scheme with adaptive step size [19]. Length scales are measured in units of L_0 and time scales in units of $L_0^{2/3} \epsilon_0^{-1/3}$. A Reynolds number can be defined as follows: The wave length λ of the smallest wave vector gives an external length scale $L = 2\pi/\sqrt{6}$, and a typical velocity on that scale is determined by the rms of one velocity component, $u_{1,rms}$. Then, in our case, the Reynolds number is $Re = \frac{u_{1,rms} L}{\nu} = 1.234 \cdot 10^5$ because from the simulations we obtain $u_{1,rms} = 2.405$.

The main features of fully developed turbulence as irregular velocity signals, characteristic scaling of structure functions, etc. are well described within this approximation, as has been shown in [16, 17, 23]. The REWA solutions show small scale intermittency, which is produced by the competition between down-scale energy transport and viscous dissipation on the small scales [17, 23]. Other mechanisms leading to intermittency in turbulence as e.g. nonlocal interactions between wave vectors are underestimated in this approximation [24]. The down-scale energy transport in the REWA fluid is less effective than in real turbulence, because in this approximation the larger wave vectors are more and more thinned out [25]. This is in contrast to the case of the complete set of wave vectors (e.g. in full grid simulations) where the density of states increases $\propto p^2$, whereas in the reduced wave vector set K the number of admitted wave vectors decreases as $1/p$ [18]. In reference [25] it has been shown that this reduced energy transport leads to an overestimation of the Taylor Reynolds number of the system as well as the Kolmogorov constant b, defined by $D(r) = b(\epsilon r)^{2/3}$, by roughly one order of magnitude for our choice of N. In the present simulation we obtain $b = 83.5$ instead of $b = 6 - 9$ as in experiments [26–28]. Since $D(L)$ is the energy density $\propto \langle\langle \boldsymbol{u}^2 \rangle\rangle$ of the fluctuations in the fluid system, the large b value indicates that even in the REWA approximation the strength of the fluctuations is highly overestimated. The large Kolmogorov constant will change the relevant time scales in the system, as will be shown in Section 4.3.2.

The characteristic time scale for the turbulent energy transfer on scale l can be estimated as [17]:

$$\tau(l) = \frac{1}{p^{(l)} u_{rms}^{(l)}}, \tag{4.19}$$

where $p^{(l)}$ denotes the mean wave number on scale l, i.e., it is the mean inverse eddy size in K_l. As in the GOY model, Eq.(4.5), the time scale of viscous dissipation is $\tau_d = 1/\nu(p^{(l)})^2$. Again, in the ISR $\tau(l) > \tau_d$, whereas in the VSR $\tau_d > \tau(l)$. From a simulation with stationary forcing, i.e., $e = 0$ in Eq. (4.16), the time delay of the energy down-transport τ_{sum} is then estimated by the sum of all $\tau(l)$ in the ISR, $\tau_{sum} = \sum_{l \in ISR} \tau(l) \simeq$0.186. The largest of these $\tau(l)$, on the largest scale, $\tau(0) = 0.0632$ can be regarded as a large eddy turnover time τ_L. Thus, $\tau_{sum} = 2.94\tau_L$ and the factor between the cascade time scale and the large eddy turnover time is $\tau_{sum}/\tau_L = a = 2.94$.

As we have seen in the GOY model, Fig.4.9, the energy transfer time is strongly fluctuating. We attributed these strong fluctuations to the one-mode per level approximation of the GOY model. Fig.4.10 shows a time series of the energy transfer time $\tau_{sum}(t)$ (use Eq.(4.19) with $u^{(l)}(t)$) in the present reduced wave vector set approximation (REWA), and, in the inset, the distribution of this time scale. Clearly, the fluctuations are much weaker than in the GOY model though presumably still larger than in full simulations; and they are zero in the mean-field approximation. The distribution is centered around $\tau_{sum}/\tau_L = a$ with a width (FWHM/2) of about $0.02a$. In a test calculation within the REWA model, where only 38 modes per level (instead of 74 in the present simulation) were used, we observed a even larger b=153 together with stronger fluctuations in the energy transfer time, which had about 5.5% fluctuations. This indicates that the size of fluctuations is growing with decreasing number of wave vectors per cascade level.

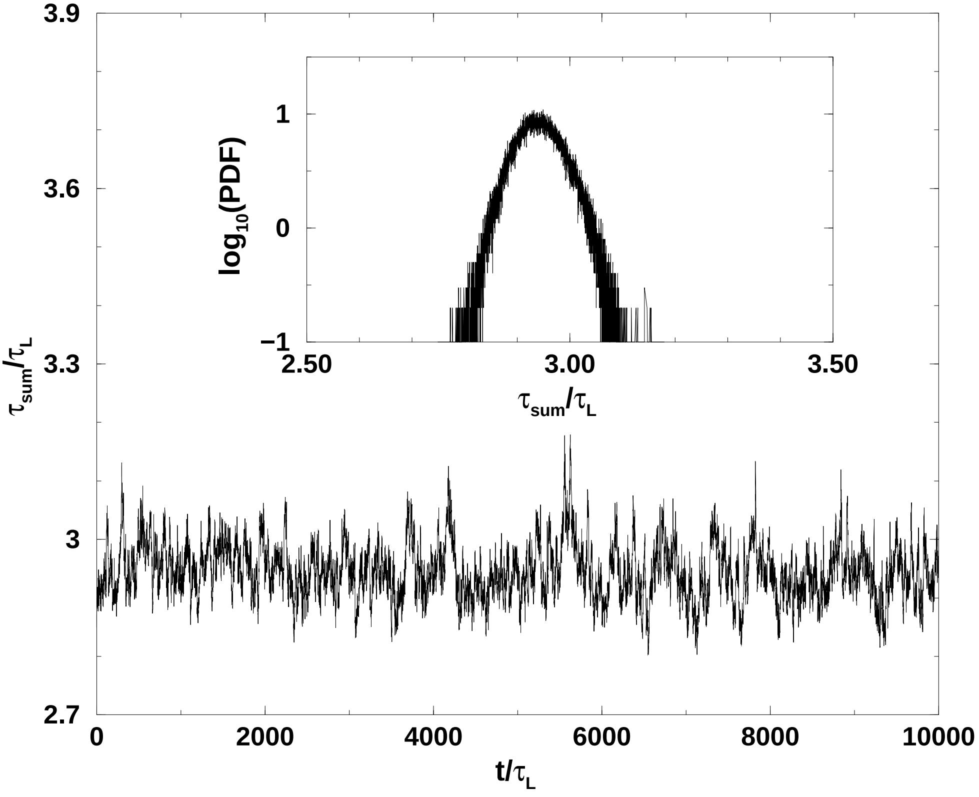

Figure 4.10: Time series of the cascade time $\tau_{sum}(t)$ in REWA. Inset: Probability distribution of τ_{sum}/τ_L. The fluctuations are considerably smaller than in the GOY model. Note the different scales in this figure and Fig.4.9. The mean is $\tau_{sum}/\tau_L = a = 2.94$, and the width FWHM/2=$0.02a$ giving about 2% fluctuations.

4.3.2 Modulated energy input rate

The response of the system to a modulated driving force, cf. Eq.(4.16), is calculated now in terms of the total energy of the system

$$E(t) = \frac{1}{2} \langle\langle \sum_{l=0}^{l=l_{max}} \sum_{\boldsymbol{p} \in K_l} |\boldsymbol{u}(\boldsymbol{p}, t)|^2 \rangle\rangle. \tag{4.20}$$

The modulation amplitude of the energy input rate e_{in} (Eq.(4.18)) is chosen as $e = 0.3$. The average is performed as follows. We average over 25 to 30 realizations, which are obtained from Eqs.(4.13) with different starting values. The delay between the different starting values is one driving period. For the higher frequencies the period $2\pi/\omega$ becomes too small to ensure statistical independence of the different realizations. Then, we chose the delay between the successive starting values for the different realizations to be several driving periods such that it is at least $60\tau_{sum}$. The response is calculated for 150 (approximately equally spaced on a logarithmic scale) frequencies between $0.00016 \leq \omega\tau_L \leq 3.0$. The energy is normalized by E_0, calculated from a stationarily forced solution with $e = 0$ and averaged as E. The oscillating response $\Delta(t)$ of the system is defined in the same way as for the GOY model, see Eq.(4.9). Then, as for the GOY calculations, the averaged signals $E^{norm}(t)$ are fitted with Eq.(4.10). The fit parameter E_{const} is again near to 1 for all frequencies, $E_{const} = 1.0064 \pm 0.0065$. In Fig.4.11 the time averaged responses and the normalized energy input rates are plotted for four different driving frequencies. Also the fits according to Eq.(4.10) are included as dashed lines but are indistinguishable from the solid lines for the energy signal itself.

We observe in Fig.4.11 for REWA the same features as in Fig.4.8 for the GOY model and in Fig.3.1 in Chapter 3 for the mean-field model. For the two lower frequencies the response amplitude remains almost constant and is about $2/3$ of the amplitude of the energy input rate, whereas for the two higher frequencies the response amplitude strongly decreases. This trend becomes more clear in Fig.4.2a in Section 4.1, where the amplitude of the response – determined from the fit (4.10) – is shown as a function of the driving frequency (full dots). For low driving frequencies $A \simeq 2/3$, whereas for high frequencies the amplitude decreases as $1/\omega$. The crossover between the regime of constant amplitude and the one of $1/\omega$-decay takes place at $\omega_{cross}\tau_L \simeq 0.011$, i.e., at a much smaller frequency than expected from the original case of the mean-field theory in which the crossover was at $\omega^{MF}_{cross}\tau_L = 1$ with $b = 6$. We understand this as follows. In Section 4.3.1 it was mentioned that the Kolmogorov constant in the REWA simulation is $b = 83.5$ instead of $b = 6 - 9$ as in the experiments. In the figures of the mean-field approach [4] we have set $b = 6$. The mean-field solution for a general b revealed that the crossover frequency decreases with increasing b while the positions of the response maxima are left unchanged. For $b = 83.5$ the mean-field crossover frequency is at $\omega^{MF}_{cross}\tau_L = (6/b)^{3/2} \simeq 0.019$ in close agreement to what we observe in the REWA simulations. The response amplitude calculated from the mean-field model with $b = 83.5$ is included in Fig.4.2a as dashed line. Apart from the changed crossover frequency we observe that, in the mean-field calculations, the first response maximum at $\omega\tau_L \simeq 0.1$ is considerably smaller and broadened as compared to the case with $b = 6$, given as the dashed line in Fig.4.1a. In agreement with this, our REWA simulations (with a value $b = 83.5$) show a broad maximum in the response amplitude at $\omega\tau_L \simeq 0.028$. This means it occurs at a similar frequency as the mean-field model. The maximum becomes more

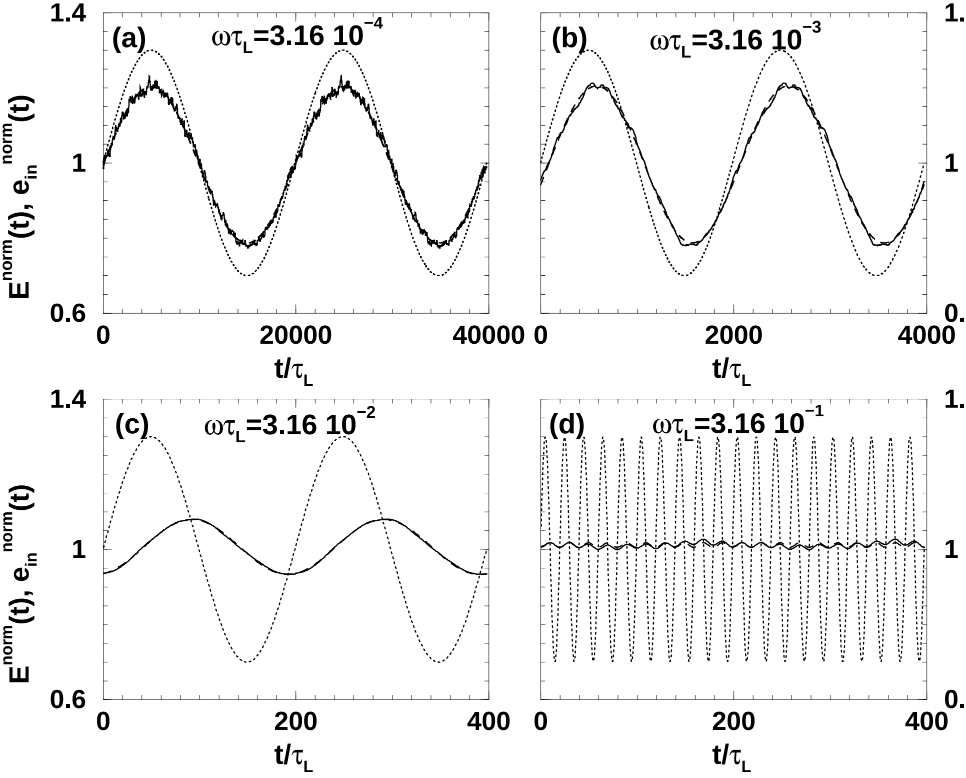

Figure 4.11: Energy input rate $e_{in}^{norm} = 1 + e \sin \omega t$ (dotted lines) and energy E^{norm} (solid lines) for four different modulation frequencies ω as calculated in the REWA simulation. The energy input rate is modulated with a modulation amplitude of 30% of the constant energy input rate, i.e., $e = 0.3$ in Eq.(4.16). Also included is the fit to the energy data cf. Eq.(4.10) as dashed lines but these are in all cases indistinguishable from the solid lines. The averaged time series of E^{norm} are repeated once for better visibility. (a) $\omega\tau_L = 3.16 \cdot 10^{-4}$, (b) $\omega\tau_L = 3.16 \cdot 10^{-3}$, (c) $\omega\tau_L = 3.16 \cdot 10^{-2}$, (d) $\omega\tau_L = 0.316$. For larger $\omega\tau_L$ the energy is indistinguishable from 1 on this scale. The crossover to the $1/\omega$-decay regime is in this simulation at $\omega\tau_L \simeq 0.011$ between the frequencies of (b) and (c).

clear in the compensated plot, Fig.4.2b, where $A/(\omega\tau_L)^{-1}$ is shown as a function of frequency. There, we observe a deviation from the $1/\omega$-decay of the amplitude by a factor 1.4 at the maximum in the REWA simulations. The mean-field maximum has a height of 2.8. The subsequent maxima and minima in the mean-field model occur at frequencies where the amplitude is already very small ($A \leq 10^{-2}$) because the crossover to the $1/\omega$-regime takes place at a much smaller frequency whereas the response maxima stay at the same frequencies as for a smaller b. Therefore, the higher order maxima are not visible in the REWA simulations. The cascade time shows about 2% fluctuation ins REWA as shown in Fig. 4.10. However, at small response amplitudes these fluctuations are already large enough to wash out the higher order response maxima.

In conclusion, the REWA system reproduces qualitatively the features of modulated turbulence as predicted by the mean-field model including the first response maximum. The latter is considerably weakened due to the large Kolmogorov constant in REWA. Another consequence of the large b is, that the crossover between constant amplitude and $1/\omega$-decay is shifted towards smaller frequencies, and therefore the higher order maxima and minima are already at very small amplitudes where the fluctuations in the cascade time scale are finally large enough to wash them out. We cannot clarify, at present, how close the response in direct numerical simulations – which lead to an order of magnitude smaller b – will come to the mean-field features, but we expect a clearly visible first maximum at least.

4.4 Conclusions

We have simulated the response of modulated turbulence within two numerical models. Namely, we have used the GOY shell model and the reduced wave vector set approximation of the Navier-Stokes equation (REWA). The results are compared with predictions from a mean-field theory. For a modulated energy input rate this mean-field theory had predicted a constant response amplitude for low frequencies and a $1/\omega$-decay for high driving frequencies. In addition, at certain frequencies connected with the energy cascade time scale, a sequence of maxima and minima of the response amplitude is observed.

Both numerical models well reproduce the basic trend, i.e., the constant amplitude for small ω and the $1/\omega$-decrease for large ω. The main response maximum can be observed in both numerical models, although it is weakened due to fluctuations. The higher order maxima and minima as predicted by the mean-field theory cannot be identified in the simulations. Obviously, they are strongly washed out by fluctuations. In the GOY model the large fluctuations are explicitly visible in a broad cascade time distribution. We attribute these fluctuations to the strong mode reduction in the model, i.e., they are an artifact of the model properties and not a feature of real turbulence. In the reduced wave vector set approximation of the Navier-Stokes equation these fluctuations are much weaker, and, we believe, more realistic for real turbulence, as more modes are taken into account. However, due to an overestimated Kolmogorov constant b in REWA the higher order maxima are considerably reduced, and therefore washed out by the fluctuations although being smaller than the GOY-fluctuations. Therefore, we believe, that in real turbulence, with a realistic Kolmogorov constant and only narrow fluctuations of the energy transfer time the first maximum should be clearly observable and possibly also the higher order extrema in the response. Thus, the predictions of the mean-field model, which excludes *all* fluctuations, might be quite reasonable for real turbulence. To further study the response maxima numerically, it is necessary to perform full numerical simulations of the Navier-Stokes equation, as then all relevant time scales including their fluctuations are reproduced realistically, which turned out to be essential for the observation of the response maxima.

Recent experiments on modulated turbulence [6] revealed evidence for the response maxima. These experiments may be more comparable to the case of a modulated *force* instead of a modulated energy input rate. We have studied this case also within the mean-field model and have found basically the same behavior of the energy response as for a modulated energy input rate. In addition, the amplitude of the energy input rate showed “wiggles” at the same frequencies where the energy response had maxima. In the experiments the response maxima were measured in the energy input rate, which can be regarded as a response of the system as well in this case. Also the constant amplitude for low driving frequencies and the $1/\omega$-decay of the velocity response – which in leading order is corresponding to a $1/\omega$-decay of the energy response as well – have been observed in the experiments. Here, we have studied the case of a modulated driving force within the GOY shell model. Also in this simulation, the response amplitude behaves basically as in the mean-field model, i.e., it decreases as $1/\omega$. The energy response amplitude as well as the amplitude of the energy input rate show the main maximum. Due to the above mentioned large fluctuations all higher order maxima are washed out in the GOY model.

There are two regimes in the frequency behavior of the response amplitude, namely a constant amplitude at low ω and a decreasing amplitude at high ω. The present simulations give further confidence that the crossover frequency between these two regimes gives the correct order of magnitude of the cascade time scale, i.e., in experiments it can be used to measure this time scale as suggested in reference [6].

Both models in the present study were able to reproduce the main features of the frequency behavior of the response amplitude in modulated turbulence as predicted by the mean-field model, however, both also have their shortcomings, which prevent us from correctly predicting the behavior of real turbulence in all quantitative details. Therefore, we believe, that it is worth to further study modulated turbulence numerically as well as experimentally.

Acknowledgments: The work is part of the research program of the Stichting voor Fundamenteel Onderzoek der Materie (FOM), which is financially supported by the Nederlandse Organisatie voor Wetenschappelijk Onderzoek (NWO). This research was also supported by the German-Israeli Foundation (GIF) and by the European Union under contract HPRN-CT-2000-00162.

References

[1] S. B. Pope, *Turbulent Flows* (Cambridge University Press, Cambridge, 2000).

[2] U. Frisch, *Turbulence* (Cambridge University Press, Cambridge, 1995).

[3] R. Labbé, J. F. Pinton, and S. Fauve, Phys. Fluids **8**, 914 (1996).

[4] A. von der Heydt, S. Grossmann, and D. Lohse, Phys. Rev. E, in press (2003).

[5] H. Effinger and S. Grossmann, Z. Phys. B **66**, 289 (1987).

[6] O. Cadot, J. H. Titon, and D. Bonn, *Experimental observation of resonances in modulated turbulence*, Preprint, submitted to J. Fluid Mech. (2002).

[7] E. B. Gledzer, Sov. Phys. Dokl. **18**, 216 (1973).

[8] M. Yamada and K. Ohkitani, J. Phys. Soc. Jpn. **56**, 4210 (1987).

[9] M. Yamada and K. Ohkitani, Prog. Theor. Phys. **79**, 1265 (1988).

[10] K. Ohkitani and M. Yamada, Prog. Theor. Phys. **81**, 329 (1989).

[11] L. Kadanoff, D. Lohse, J. Wang, and R. Benzi, Phys. Fluids **7**, 617 (1995).

[12] L. Biferale, Ann. Rev. Fluid Mech. **35**, 441 (2003).

[13] M. H. Jensen, G. Paladin, and A. Vulpiani, Phys. Rev. A **43**, 798 (1991).

[14] T. Bohr, M. H. Jensen, G. Paladin, and A. Vulpiani, *Dynamical Systems Approach to Turbulence* (Cambridge University Press, Cambridge, 1998).

[15] J. O. Hooghoudt, D. Lohse, and F. Toschi, Phys. Fluids **13**, 2013 (2001).

[16] J. Eggers and S. Grossmann, Phys. Fluids A **3**, 1958 (1991).

[17] S. Grossmann and D. Lohse, Z. Phys. B **89**, 11 (1992).

[18] S. Grossmann and D. Lohse, Phys. Fluids **6**, 611 (1994).

[19] W. Press, S. Teukolsky, W. Vetterling, and B. Flannery, *Numerical Recipes* (Cambridge University Press, Cambridge, 1986).

[20] R. Benzi, L. Biferale, and G. Parisi, Physica D **65**, 163 (1993).

[21] N. Schörghofer, L. Kadanoff, and D. Lohse, Physica D **88**, 40 (1995).

[22] L. Kadanoff, D. Lohse, and N. Schörghofer, Physica D **100**, 165 (1997).

[23] S. Grossmann and D. Lohse, Physica A **194**, 519 (1993).

[24] S. Grossmann, D. Lohse, and A. Reeh, Phys. Rev. Lett. **77**, 5369 (1996).

[25] S. Grossmann and D. Lohse, Phys. Rev. E **50**, 2784 (1994).

[26] A. S. Monin and A. M. Yaglom, *Statistical Fluid Mechanics* (The MIT Press, Cambridge, Massachusetts, 1975).

[27] K. R. Sreenivasan, Phys. Fluids **7**, 2778 (1995).

[28] K. R. Sreenivasan and R. A. Antonia, Ann. Rev. of Fluid Mech. **29**, 435 (1997).

Chapter 5

How Snapping Shrimp Snap: Through Cavitating Bubbles [*]

The snapping shrimp (Alpheus heterochaelis) produces a loud snapping sound by an extremely rapid closure of its snapper claw. It was commonly believed that the sound is generated when the two claw surfaces hit each other. We show that the sound, in fact, originates from the collapse of a cavitation bubble. During the rapid snapper claw closure a high-velocity water jet is emitted from the claw with a speed exceeding cavitation conditions. Hydrophone measurements in conjunction with time-controlled high-speed imaging of claw closure demonstrate that the sound is emitted at the cavitation bubble collapse. A model for the bubble dynamics based on a Rayleigh-Plesset type equation quantitatively accounts for the time dependence of the bubble radius and for the emitted sound. One of the functions of the snapping is to stun or even to kill prey animals. Here we have thus shown that snapping shrimp indeed possess an effective acoustic weapon based on a collapsing cavitation bubble.

5.1 Introduction

The oceans may be deep, but they are not at all quiet [1]. Listening to the sounds in the oceans one would hear the sound of waves, produced by tides, winds and thunderstorms, and of falling rain, hail and snow. In addition, one can hear biological sounds of fish, dolphins, whales and snapping shrimp. The latter, in particular, produce

---

[*] See also M. Versluis, B. Schmitz, A. von der Heydt, and D. Lohse, *How Snapping Shrimp Snap: Through Cavitating Bubbles*, Science **289**, 2114 (2000)

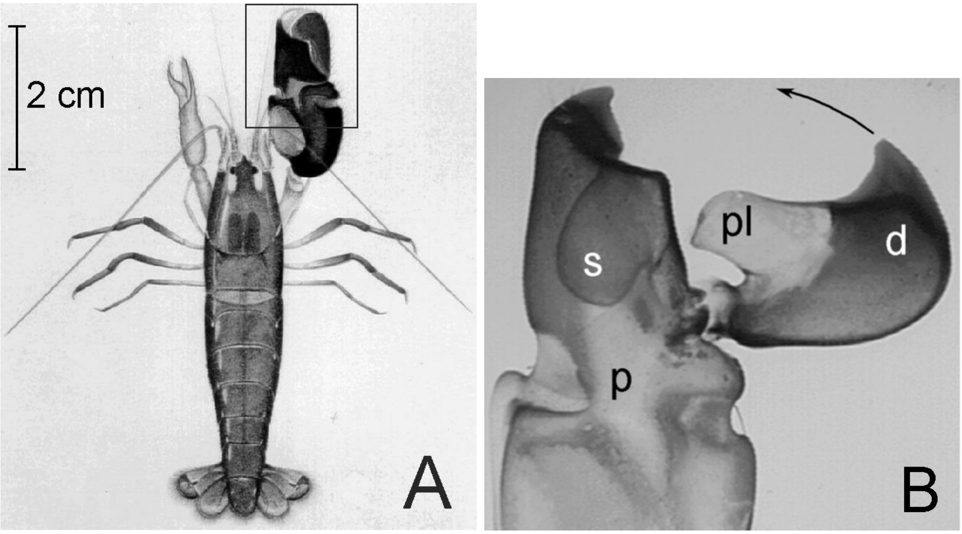

Figure 5.1: (A) *Alpheus heterochaelis* - one of the largest snapping shrimp. The large snapper claw may be either on the right or the left in both sexes. Modified after Brooks & Herrick [8]. (B) Close-up of the snapper claw in its cocked position. The claw is made transparent by the use of methyl salicylate. The claw has a protruding plunger (labeled pl) on the dactyl (d) and a matching socket (s) in the immobile propus (p) (Photograph by B. Seibel). During the extremely rapid closure of the snapper claw a high-velocity water jet is formed when the plunger displaces the water from the propus socket.

the dominant level of ambient noise in (sub)tropical shallow waters throughout the world [2]. These shrimp usually occur in such large numbers that there is continuous snapping, providing a permanent crackling background noise, commonly associated with the sound of burning dry twigs [3]. The snapping sound can be heard day and night [4], with source levels as high as 190 to 210 dB re 1 μPa at 1 m distance (peak-to-peak) [5, 6]. This severely limits the use of underwater acoustics for active and passive sonar, both in scientific and naval applications. The frequency spectrum of a snap is extremely broad, ranging from tens of hertz to beyond 200 kHz [5]. The noise of snapping shrimp is therefore also used as a source for creating pictorial images of objects in the ocean through ensonification [7].

A snapping shrimp of the species *Alpheus heterochaelis* (about 5.5 cm in size) is depicted in Fig.5.1a. The shrimp produces the snapping sound by an extremely rapid closure of its large snapper claw, which may reach 2.8 cm in length, about half its body size. The claw (Fig.5.1b) has a protruding plunger on the dactyl and a matching socket in the propus. Before snapping, the claw is cocked open by co-contraction of an opener and a closer muscle, building up tension until a second closer muscle contracts [9]. This results in an extremely rapid closure of the claw [10]. A high-velocity water jet is formed when the dactyl plunger is driven into the propus socket, displacing water [11, 12]. The water jet is received and analyzed by sensory hairs on the snapper claw of con-specific snapping shrimp. Therefore the snapping plays an important role in intra-specific communication [13]. In addition, it is used to defend a shelter or territory against intruders as well as to stun and even kill prey animals [11, 14].

The loud impulsive snap of the snapping shrimp has been attributed to the mechanical contact made when the dactyl and the propus edges hit each other as the claw closes [6, 15]. Here we will show that the sound of snapping shrimp originates solely from the collapse of a cavitation bubble that is generated by the fast water jet resulting from the rapid claw closure. The water jet velocity is so high that the corresponding pressure drops below the vapor pressure of water. Sea water contains tiny air bubbles, called nuclei [16]. Such a micro-bubble, if located between the dactyl and the propus of the snapper claw, will grow in size when it is entrained in the region of low pressure generated through the water jet. Subsequently, it collapses violently when the pressure rises again.

5.2 Experimental results

The experiments were performed with 7 individuals of *A. heterochaelis*. The shrimp was positioned on a small textile platform in a sea water aquarium and tethered to a vertical holder by a plastic nut glued to its back. The snap was evoked by gently touching the freely movable snapper claw with a soft paintbrush. A hydrophone with an upper frequency limit of 100 kHz was positioned at a small distance from the shrimp. Simultaneously, high-speed images were recorded with a digital monochrome video camera at a frame rate of 40500 frames per seconds (fps) with a resolution of 64×64 pixels. The image acquisition was triggered by the sound of the snap. A typical hydrophone signal is shown in Fig.5.2. The main peak at $t = 0$ is followed by a very broadband signal, which is partly due to the reflections of the main signal at the aquarium walls located at a minimum distance of 15 cm. Therefore, the first reflections start after 200 μs. The hydrophone signal shows a precursor signal before the main peak, similar to that previously observed in recordings of the smaller *Synalpheus paraneomeris* snapping shrimp [5].

A sequence of high-speed images, showing the snapper claw from the top, is presented in Fig.5.3. The snapper claw is in its cocked position in frame 1. Full closure of the claw is achieved at frame 2 (600 μs later) followed by bubble growth (within 375 μs, although the onset of bubble growth is not visible in this view) and bubble collapse at t = 0 in frame 3. The images show that the cavitation bubble, which was recorded in each of our 108 experiments, is non-spherical and elongated

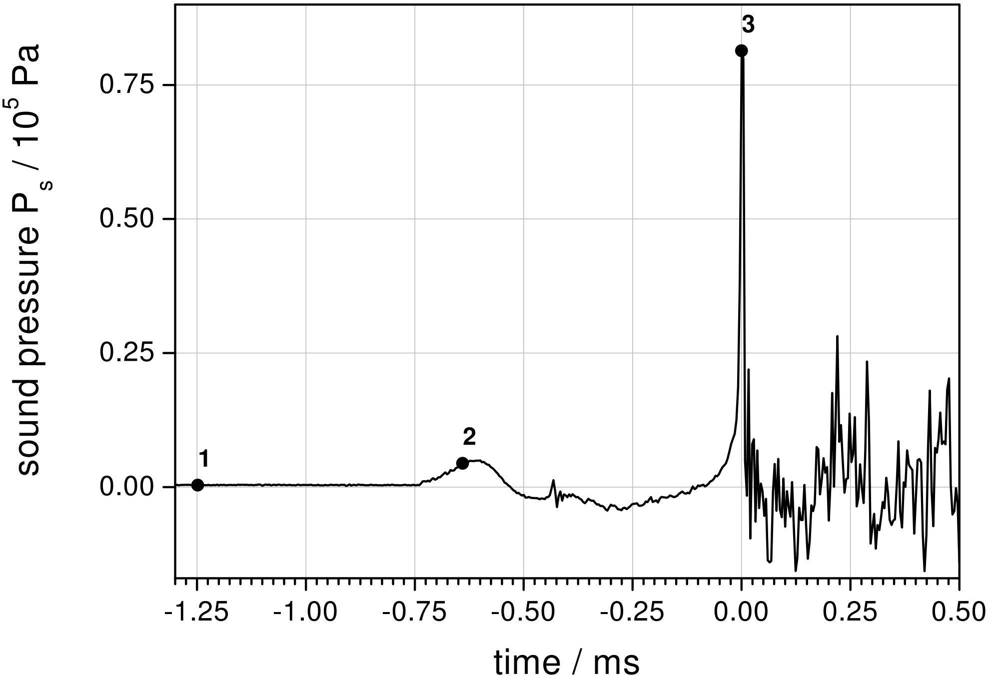

Figure 5.2: Hydrophone signal of a snap by an *Alpheus heterochaelis* female measured at a distance $r = 4$cm. Note the precursor signal before and the broadband signal after the main peak at $t = 0$. The broadband signal is partly due to the reflections of the main signal at the aquarium walls. The small peak at $t = -0.425$ ms coincides with the collapse of a small cavitation bubble under the claw [17].

in the direction of the water jet. The bubble grows to a maximum equivalent radius of 3.5 mm on average. At collapse (frame 3), the transparent single cavitation bubble breaks apart and an opaque cloud of small bubbles is formed, which finally dissolves.

The temporal correlation between the snapping sound and the bubble dynamics was determined from these high-speed video recordings. The hydrophone signal and the exposure timing of the high-speed camera were measured simultaneously, referenced to a trigger signal. The main peak of the snapping sound and the collapse of the cavitation bubble always coincide. An analysis of 19 different experiments showed that the temporal correlation of sound and bubble collapse is achieved with a standard deviation of 0.86 frames, i.e. accurate within 25 μs. Remember that the claw is closed in frame 2, 650 μs (or 26 frames at 40500 fps) before bubble collapse!

The angular velocity of dactyl rotation was determined from the position of the tips of dactyl and propus relative to the position of the pivot point. Claw closure begins with moderate angular velocities (order 100 rad/s) for large opening angles. In

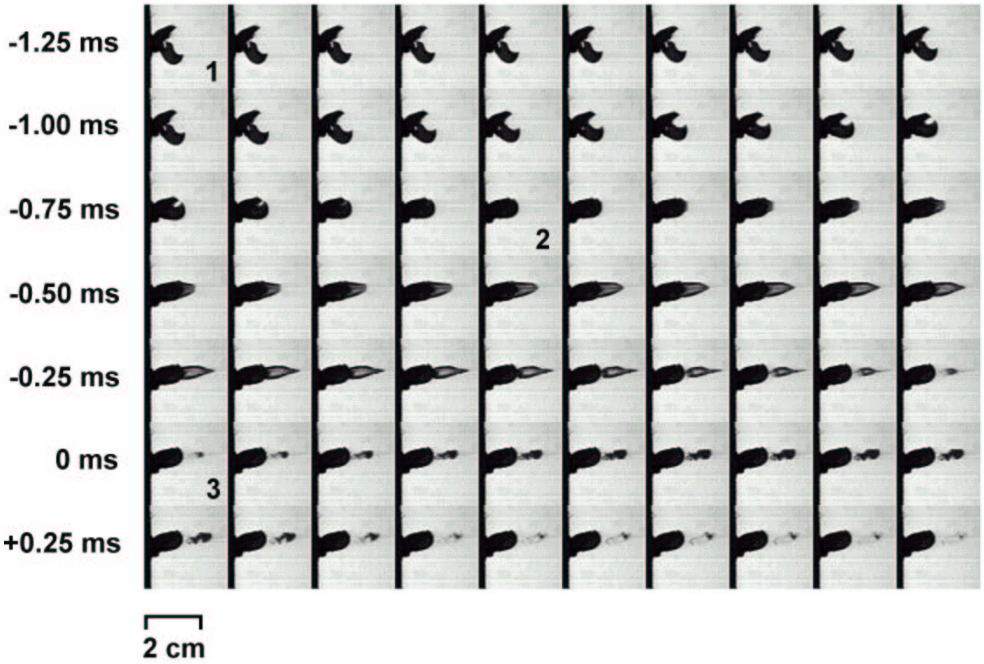

Figure 5.3: A sequence of high-speed images in top view showing the closure of the snapper claw taken at 25 μs-intervals (40500 frames per second). Each tick mark on the time axis of the hydrophone signal in Fig.5.2 indicates an image recording. The dactyl rotation starts at frame 1 at $t = -1.250$ ms. The main peak of the sound emission is at $t = 0$ (frame 3) and coincides with the collapse of the cavitation bubble. Full closure of the claw was already achieved at frame 2, 0.65 ms before bubble collapse.

the final stage of claw closure, the dactyl rotates with an impressive 3500 rad/s. Angular velocities of this order were measured before with a thin laser-coupled optical fiber glued onto the distal tip of the dactyl [10].

The occurrence of cavitation bubbles during the snap of the snapping shrimp now also explains why the snaps are so harmful to prey animals. It is cavitation damage, known to damage e.g. ship propellers and centrifugal pumps. More specifically, here we have an example of jet cavitation, not wake cavitation as in ship propulsion. The destructive force of a collapsing cavitation bubble can be seen during inter-specific encounters: small prey (e.g. worms, goby fish or other shrimp) can be stunned or killed [14]. In a recent study [18] it was found that small crabs (*Eurypanopeus depressus*) are injured by the snap of snapping shrimp. The interaction distance, defined as the distance of the tip of the snapper claw to the nearest body part of the opponent measured along the snapper claw long axis, was reported to be 3 mm on average. In our experiments it is shown that the cavitation bubble collapses 3 mm in front of the tip of the snapper claw (see Fig.5.3). In intra-specific encounters the snap is not used to injure the opponent, but rather as a communication signal. The interaction distance is 9 mm on average [13], far enough away from implosion danger.

5.3 Theoretical Modeling

The velocity of the water jet was estimated from the speed of the cavitation bubble. High-speed video close-ups of the cavitation bubble indicate velocities of the front end of the bubble as high as 32 m/s, while the bubble expands longitudinally with a speed of 9 m/s. This indicates a flow with a speed $\boldsymbol{v}_{max}$ in the order of 25 m/s. This high water jet velocity implies a pressure drop from the ambient pressure $P_0 = 10^5$ Pa, which can, in principle, be modeled through Bernoulli's law. However, there is limited information on the actual temporal and spatial shape of the velocity field, and consequently also on the pressure field. Nevertheless, the unsteady term in Bernoulli's law, $\rho\partial_t\Phi$ (where ρ represents the density of water and ∂_t is the partial derivative with respect to time, and Φ is the velocity potential) can be estimated by dimensional arguments and is smaller or at most of the same order of magnitude as the kinetic energy term. Therefore we estimate the magnitude of the pressure drop as $P_a \propto \frac{1}{2}\rho\boldsymbol{v}_{max}^2$. With the above water jet velocity, $P_a \propto 3105$ Pa. Moreover, we assume a Gaussian pressure distribution in time:

$$P(t) = P_0 - P_a \exp\left(-4(\ln 2)\frac{(t-t_0)^2}{\sigma^2}\right), \tag{5.1}$$

where σ represents the width of the Gaussian pulse. As the pressure $P(t)$ drops below the vapor pressure of water ($P_{vap} = 2 \cdot 10^3$ Pa), cavitation occurs.

The bubble that arises at the tip of the snapper claw is not spherical. Modeling the dynamics of non-spherical bubbles is non-trivial [19], requiring that all parameters such as the water jet velocity and width, the size and shape of the bubble nucleus, etc. be precisely known. This is not the case. However, to get at least a semi-quantitative statement, we can assume a spherical bubble. Its dynamics is well described by Rayleigh-Plesset type equations [16].

Typical bubble nuclei in sea water are between 1 and 50 μm in radius [16, 20]. We assume a nucleus initially filled with air of initial radius $R_0 = 10\mu$m under normal conditions. The results hardly depend on the choice of R_0. The response of the bubble nucleus on the pressure reduction (Eq.(5.1)) is described by the (modified)

Keller-Equation [21], which is of Rayleigh-Plesset type:

$$\begin{aligned}\left(1-\frac{\dot{R}}{c}\right)R\ddot{R}+\frac{3}{2}\left(1-\frac{\dot{R}}{3c}\right) &= -4\nu\frac{\dot{R}}{R}-\frac{2S}{\rho R} \\ &\quad +\frac{1}{\rho}\left(1+\frac{\dot{R}}{c}\right)(p(R,t)+P_{vap}-P(t)) \\ &\quad +\frac{R}{\rho c}\frac{d}{dt}p(R,t).\end{aligned} \tag{5.2}$$

The parameters for an air bubble in water are the viscosity of water ν, its density ρ, the speed of sound c, and the surface tension of the air-water system S. The terms proportional to $\dot{R}/c$ take into account the effects of liquid compressibility. $p(R,t)$ is the pressure inside the bubble and can be modeled by a van der Waals equation of state:

$$p(R,t)=\left(P_0-P_v+\frac{2S}{R_0}\right)\left(\frac{R_0^3-h^3}{R(t)^3-h^3}\right)^{\gamma}, \tag{5.3}$$

with the van der Waals hard core radius $h=R_0/8.54$ [22]. From an estimation of the Peclét number, $Pe=\frac{R\dot{R}}{\kappa}\ll 1$, where κ is the thermal diffusivity, we find that we can assume adiabatic behavior [16, 23, 24], i.e., $\gamma=7/5$ for nitrogene. During the relatively slow process of expansion water vapor enters the bubble, which reduces the violence of the collapse. Since the amount of water vapor inside the bubble is diffusion-controlled [25], we couple an additional equation for the water vapor concentration inside the bubble to the Keller equation [26].

For given bubble dynamics $R(t)$ the emitted sound wave at distance r from the bubble simply follows from [27, 28]

$$P_s(r,t)=\frac{\rho R}{r}(2\dot{R}^2+R\ddot{R}). \tag{5.4}$$

In Fig.5.4 the modeled pressure reduction (Eq.(5.1)) and the calculated bubble radius resulting from Eq.(5.2) are plotted as a function of time. As the pressure decreases, the bubble begins to grow up to a maximum radius of about 3.6 mm. Note the time delay through inertia: At maximum bubble radius the pressure has already risen again to the ambient pressure P_0. Subsequently, the bubble collapses rapidly within about 300 μs. After the bubble collapse, the numerical solution of Eq.(5.2) shows some after-bounces. These are not observed in the experiment, as the bubble is destroyed upon collapse. Indeed, if we perform a linear stability analysis of the spherical bubble [24, 29], we find exactly the same feature at bubble collapse: the bubble is destroyed through a Rayleigh-Taylor type instability.

The model parameters P_a and σ were fitted to match the theoretical radius with the experimentally determined equivalent bubble radius of the ellipsoidal cavitation

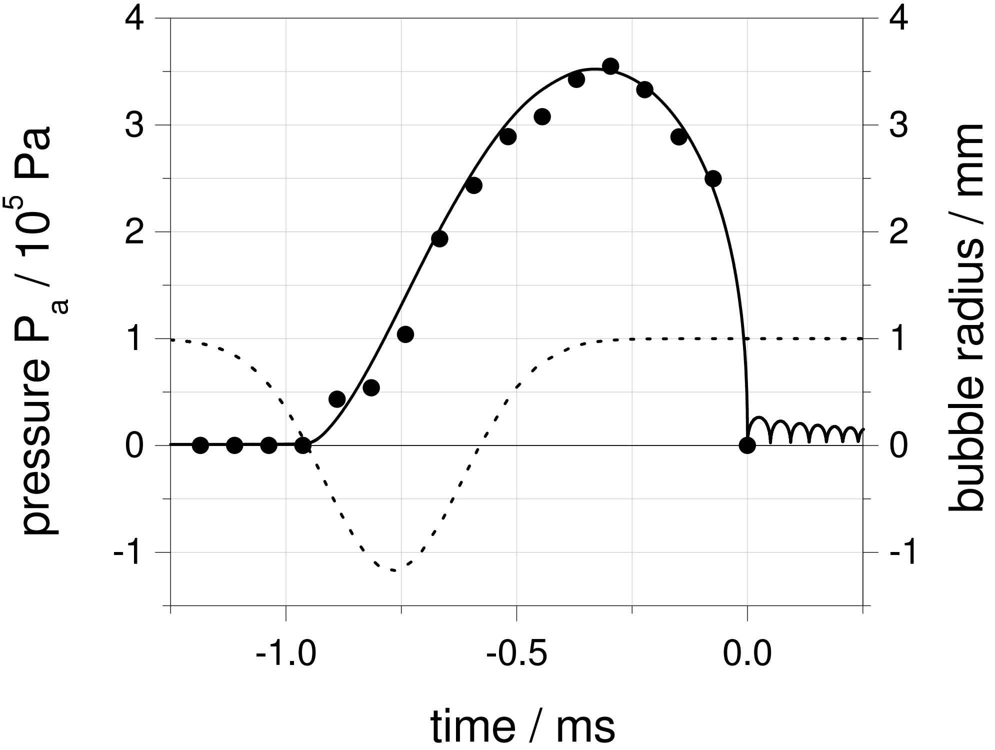

Figure 5.4: The calculated bubble radius $R(t)$ as a function of time (solid line). The temporal change of the pressure field $P(t)$ that was modeled for this calculation is also given (dotted line). The model parameters ($P_a = 2.2 \cdot 10^5\text{Pa}; \sigma = 360\mu\text{s}$) were fitted to match the theoretical radius with the experimentally determined equivalent bubble radius of the ellipsoidal cavitation bubble indicated by the filled circles.

bubble (filled circles in Fig.5.4). Using these model parameters, the calculated sound pressure curve (from Eq.(5.4)) is in good agreement with the experimental sound signal, see Fig.5.5. The main acoustical signal is preceded by a small sinusoidal precursor, caused by the bubble expansion and contraction. At collapse ($t = 0$), the main acoustical signal is emitted. The narrow peaks in the calculated sound signal after the main pressure peak are produced by the aforementioned after-bounces and should not be considered here, as the bubble is destroyed on collapse. Quantitatively, the model overestimates the measured sound pressure, especially the maximum pressure. The reason is threefold: (i) The non-spherical shape of the real bubble reduces the strength of the collapse and therefore the intensity of the emitted sound, (ii) thermal damping effects [30] are not included in the model, and (iii) on the experimental side the limited bandwidth of the hydrophone underestimates the peak value of the

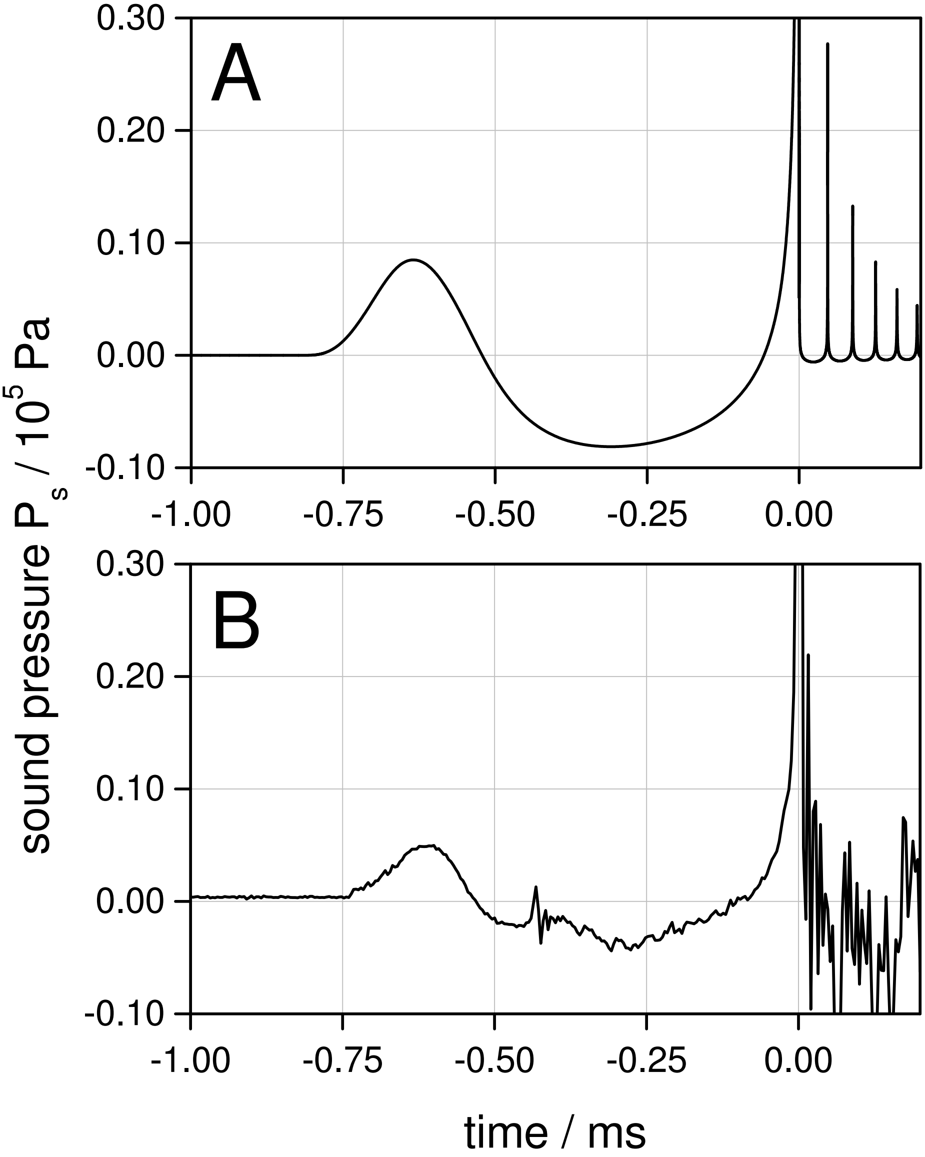

Figure 5.5: (A) The calculated sound pressure $P_s(r, t)$ for $r = 4$ cm with $P_a = 3.0 \cdot 10^5$ Pa and $\sigma = 210\mu$s. The main peak at $t = 0$ ($P_s = 2 \cdot 10^8$ Pa) is drawn off-scale to emphasize the precursor signal. (B) An enlarged view of the experimental sound pressure curve of Fig.5.2.

sound pressure.

The calculated width of the main acoustical peak for the modeled spherical bubble is extremely small, in the order of 100 ps. This δ-like pulse corresponds to a white noise spectrum. Indeed, in previous review articles [1, 5] on ambient noise it was noted that the sound of the snapping shrimp covers a wide frequency range, even in excess of 200 kHz. For a more quantitative comparison of the theoretical and experimental spectrum, one must include the asphericity of the collapse, the acoustical emission of the bubble fragments, and the sound reflections from the walls into the model, which is beyond the scope of this work.

The variation in claw size, claw shape, cocking duration, applied closer muscle force and claw closure speeds of snapping shrimp all lead to slightly different sound signals and obviously they all have different water jet characteristics. By adjusting the two parameters P_a and σ in our model we are able to account for the variety of precursor signals measured from the snaps of the 7 analyzed snapping shrimp [17].

Acknowledgments: Supported by a grant of the Stichting voor Fundamenteel Onderzoek der Materie (FOM) and by a grant of the Deutsche Forschungsgemeinschaft (DFG - Schm 693/5-4) to BS. The experimental assistance of Miriam Hansbauer is gratefully acknowledged. We offer special thanks to Norbert Franz of the electronics workshop of the Dept. of Physics, Technical University of Munich for repairing our Schmitt trigger device on Christmas Eve. MV is supported by FOM. AvdH is supported by the German-Israeli Foundation (GIF).

References

[1] R. Urick, *Principles of underwater sound* (McGraw-Hill, New York, 1983).

[2] D. Cato and M. Bell, Material Research Laboratory Technical Report (MRL-TR-91-23), Defence Science and Technology Organisation, Sydney (unpublished).

[3] M. Johnson, F. Everest, and R. Young, Biol. Bull. **93**, 122 (1947).

[4] F. Everest, R. Young, and M. Johnson, J. Acoust. Soc. Am. **20**, 137 (1948).

[5] W. Au and K. Banks, J. Acoust. Soc. Am. **103**, 41 (1998).

[6] B. Schmitz, in *Physiology of the Crustacean nervous system*, edited by K. Wiese (Springer-Verlag, ADDRESS, submitted (2000)).

[7] C. Epifanio, J. Potter, G. Deane, M. Readhead, and M. Buckingham, J. Acoust. Soc. Am. **106**, 3211 (1999).

[8] W. Brooks and F. Herrick, Mem. Nat. Acad. Sci. Wash. **5**, 319 (1891).

[9] R. Ritzmann, J. Comp. Physiol. **95**, 217 (1974).

[10] B. Schmitz and J. Herberholz, in *New neuroethology on the move* (Thieme, Stuttgart, 1998), p. 241.

[11] J. Herberholz and B. Schmitz, J. Comp. Physiol. A **185**, 41 (1999).

[12] H. Schein, Mar. Behav. Physiol. **3**, 83 (1975).

[13] J. Herberholz and B. Schmitz, Biol. Bull. **195**, 156 (1998).

[14] G. MacGinitie and N. MacGinitie, *Natural history of marine animals* (McGraw Hill, New York, 1949).

[15] P. Volz, Z. Morph. kol. Tiere **34**, 272 (1938).

[16] C. Brennen, *Cavitation and Bubble Dynamics* (Oxford Press, New York, 1995).

[17] M. Versluis, B. Schmitz, A. von der Heydt, and D. Lohse (unpublished).

[18] S. Schultz, K. Wuppermann, and B. Schmitz, Zoology - Analysis of complex systems **101 [Suppl. I]: (DZG 91.1)**, 85 (1998).

[19] J. Blake, Y. Tomita, and R. Tong, Appl. Sci. Res. **58**, 77 (1998).

[20] S. Ceccio and C. Brennen, J. Fluid Mech. **233**, 633 (1991).

[21] A. Prosperetti and A. Lezzi, J. Fluid Mech. **168**, 457 (1986).

[22] S. Grossmann, S. Hilgenfeldt, D. Lohse, and M. Zomack, J. Acoust. Soc. Am. **102**, 1223 (1997).

[23] M. Plesset and A. Prosperetti, Annu. Rev. Fluid Mech. **9**, 145 (1977).

[24] S. Hilgenfeldt, D. Lohse, and M. Brenner, Phys. Fluids **8**, 2808 (1996).

[25] B. Storey and A. Szeri, Proc. Roy. Soc. London A **456**, 1685 (2000).

[26] R. Tögel, B. Gompf, D. Lohse, and R. Pecha, Phys. Rev. Lett. **85**, 3165 (2000).

[27] L. D. Landau and E. M. Lifshitz, *Fluid Mechanics* (Pergamon Press, Oxford, 1987).

[28] S. Hilgenfeldt, D. Lohse, and M. Zomack, Eur. Phys. J. B **4**, 247 (1998).

[29] A. Prosperetti, Quart. Appl. Math. **35**, 339 (1977).

[30] Y. Hao and A. Prosperetti, Phys. Fluids **11**, 2008 (1999).

Chapter 6

Conclusions

In this work we have studied different aspects of nonideal turbulence. A variable-range mean-field theory which has originally been developed for homogeneous, isotropic and stationary turbulence [1], has been successfully extended to weakly anisotropic flow as well as to time periodic driving forces. Although the mean-field theory does not take into account turbulent fluctuations, it seems to be able to correctly predict some basic features of nonideal turbulent flows. This is confirmed by comparing the results with experimental and numerical data. Clearly, the limitation of this approach is that intermittency effects cannot be captured. In this chapter we summarize and discuss the main results of the previous chapters.

The first nonideal property we considered was (weak) anisotropy (Chapter 2, [2]). The second order velocity structure function is decomposed into its SO(3) invariants [3] and the scaling behavior of the different j-amplitudes of the SO(3)-decomposition is derived. For the isotropic sector, $j = 0$, Kolmogorov scaling is recovered, $d_{j=0} \propto r^{2/3}$. The scaling of the anisotropic sectors, $j > 0$, can be calculated order by order in the spherical harmonics Y_{jm}. The higher order j scaling exponents depend on the type of forcing. For a non-analytic forcing, representing shear flow, the same mean-field scaling, $d_j \propto r^{4/3}$, is found for all nonzero and even j, whereas an analytic type of forcing yields $d_j \propto r^{j+2/3}$. The odd j-amplitudes vanish in this case due to symmetry. Analytic means that the velocity profile and the forcing are analytic in the components of the position $\boldsymbol{x}$ and the scale vector $\boldsymbol{r}$. The values found for the non-analytic forcing are consistent with experimental [4] and numerical [5] data for the $j = 0$ and $j = 2$ sectors. This type of forcing may be more general than the analytic forcing, and therefore, may be applicable for a wider range of flows. However, this finding suggests that the scaling exponents of the anisotropic sectors may not be universal as they seem to depend on the type of forcing.

For the higher sectors $j > 2$ the situation is still unclear. While the non-analytic forcing suggests the same mean-field scaling exponents for all higher order j sectors, increasing scaling exponents with increasing j (for $j = 4$ and $j = 6$) have been found in numerical simulations [6]. However, for these high j sectors no experimental data are available yet. In the experiments of reference [4] a second order object has been used to measure the scaling exponent for $j = 2$ which in principle also contains higher j-contributions. If the contributions for $j > 2$ have scaling exponents very different from $4/3$ one would not expect clean scaling behavior for this second order object, as then it would be a mixture of different power laws. On the other hand, the higher j-contributions are expected to be much smaller than the $j = 2$ contributions, and therefore, they may only weakly influence the scaling behavior, i.e., they may be negligible for determining the $j = 2$-scaling exponent. Therefore, the situation is not conclusive for the higher j-amplitudes yet.

Another aspect of nonideal turbulence is studied in the Chapters 3 and 4, [7, 8]. There, we assume fully developed homogeneous and isotropic turbulence which is driven by a modulated driving. The energy transfer time τ, which represents the average time the energy stays in the system while it is downcascading the interaction cascade, plays a crucial role in this case. It can be estimated by the large eddy turnover time τ_L, i.e., $\tau = a\tau_L$, where a is a factor of order 1. The variable-range mean-field theory is extended to a situation with a modulated driving in Chapter 3. In this theory the cascade time τ is assumed to be constant. In real turbulence, nevertheless, this time scale will be fluctuating. To account for the effect of turbulent fluctuations, we performed numerical simulations within two dynamical cascade models of turbulence, see Chapter 4. There, a periodic driving is applied to the GOY shell model [9–16] as well as to the reduced wave vector set approximation of the Navier-Stokes equation (REWA) [17–19]. The main results of all three approaches are summarized in Table 6.1. Two cases are considered: (i) a modulated energy input rate $e_{in}(t) = \epsilon_0(1 + e\sin\omega t)$ (see left column of Table 6.1) and (ii) a modulated force in the Navier-Stokes equation, $\boldsymbol{f} = \boldsymbol{f}_0(1 + e_f \sin\omega t)$ (right column of Table 6.1). The response of the system is studied in terms of the total energy $E(t)$ or the Reynolds number $Re(t)$ of the system.

For the modulated energy input rate we find the following behavior of the response amplitude $A(\omega)$ (defined by $E(t)/E_0 = 1 + eA\sin(\omega t + \Phi)$ where E_0 is the stationary mean value of the energy): For small driving frequencies ($\omega\tau_L \ll 1$) the response amplitude is constant, whereas for large driving frequencies ($\omega\tau_L \gg 1$) the amplitude decreases as $A(\omega) \propto 1/\omega$ indicating that at very large frequencies the oscillation of the driving becomes so fast, that the system cannot follow the oscillation of the driving any more and feels only a constant mean energy input rate. This behavior is found in the mean-field model as well as in both numerical models, see Figs. 3.2, 4.1, and 4.2. The crossover between the two regimes takes place at $\omega\tau_L = 1$ in the mean-field model, and at $\omega\tau_L \simeq 1/a$ in the GOY model, i.e., at frequencies

	Modulated energy input rate	**Modulated force**
Mean-field theory	$\omega \ll 1/\tau$: $A(\omega) \simeq 2/3$ $\omega \gg 1/\tau$: $A(\omega) \propto 2/(3\omega\tau_L)$ Crossover at $\omega\tau_L = 1$ Response maxima and minima: $A(\omega)$ has maxima at $\omega_r(0)\tau_L \simeq 1/a$ and $\omega_r(n)\tau_L \simeq n\frac{\pi}{a}$, n even $A(\omega)$ has minima at $\omega_r(n)\tau_L \simeq n\frac{\pi}{a}$, n odd	$\omega \ll 1/\tau$: $A(\omega) \simeq 1$ $A_{e_{in}}(\omega) \simeq 1.5$ $\omega \gg 1/\tau$: $A(\omega) \propto 2/(3\omega\tau_L)$ $A_{e_{in}}(\omega) \simeq 1$ Crossover at $\omega\tau_L = 1$ Response maxima and minima: $A(\omega)$ has maxima at $\omega_r(0)\tau_L \simeq 1/a$ and $\omega_r(n)\tau_L \simeq n\frac{\pi}{a}$, n even $A(\omega)$ has minima at $\omega_r(n)\tau_L \simeq n\frac{\pi}{a}$, n odd $A_{e_{in}}(\omega)$ has wiggles at $\omega_r(0)\tau_L \simeq 1/a$ and $\omega_r(n)\tau_L \simeq n\frac{\pi}{a}$, n even
GOY	$\omega \ll 1/\tau$: $A(\omega) \simeq 2/3$ $\omega \gg 1/\tau$: $A(\omega) \propto 1/(\omega\tau_L)$ Crossover at $\omega\tau_L \simeq 1/a$ Response maxima and minima: $A(\omega)$ shows main maximum Fluctuations of τ overestimated	$\omega \ll 1/\tau$: $A(\omega) \simeq 1$ $A_{e_{in}}(\omega) \simeq 1.5$ $\omega \gg 1/\tau$: $A(\omega) \propto 1/(\omega\tau_L)$ $A_{e_{in}}(\omega) \simeq 1$ Crossover at $\omega\tau_L \simeq 1/a$ Response maxima and minima: $A(\omega)$ shows main maximum $A_{e_{in}}(\omega)$ has maximum at $\omega\tau_L \simeq 1/a$ Fluctuations of τ overestimated
REWA	$\omega \ll \left(\frac{6}{b}\right)^{3/2}\frac{1}{\tau}$: $A(\omega) \simeq 2/3$ $\omega \gg \left(\frac{6}{b}\right)^{3/2}\frac{1}{\tau}$: $A(\omega) \propto 1/(\omega\tau_L)$ Crossover at $\omega\tau_L \simeq (6/b)^{3/2}$ Response maxima and minima: $A(\omega)$ shows main maximum Kolmogorov constant $b = 83.5$ overestimated	work in progress

Table 6.1: Main results of the three studied models for modulated turbulence

of the same order of magnitude. In the REWA model the crossover takes place at a much smaller frequency. This is because in REWA the Kolmogorov constant b is overestimated by one order of magnitude. With our choice of wave vectors we have $b = 83.5$ instead of the experimental values $b = 6 - 9$ [20–23], which reflects the considerable reduction of the transport of energy through the system due to the mode selection. With this large value of b the crossover frequency as predicted by the mean-field model is at $\omega_{cross}\tau_L = (6/b)^{3/2}$, which is in good agreement with the crossover frequency observed in REWA. Thus, in experiments, where b takes values between 6-9, the crossover frequency can be used to estimate the energy cascade time scale. This has been done in recent experiments [24].

The mean-field response amplitude shows several maxima and minima at frequencies connected to the energy cascade time scale τ, see Fig.3.2. The physical explanation for these response extrema is that at the response maxima, the energy dissipation and the response are in phase, meaning that the transport of energy is very efficient, while it is very inefficient at the response minima. At the latter frequencies the energy dissipation rate and the response are exactly out of phase. The main maximum can also be observed in both numerical models, cf. Figs. 4.1 and 4.2, although it is weakened by the fluctuations. The higher order maxima and minima are completely washed out by turbulent fluctuations in the two numerical models. On the other hand, in the GOY model these fluctuations are artificially large due to the approximation of only one mode per cascade level, and therefore, may not be regarded as an effect of real turbulence. In the REWA simulation, where many more modes per level are taken into account, the fluctuations are much smaller, and probably more realistic. However, in the REWA simulation, too, we observe only a weak and broad first maximum near to the crossover frequency. This can be explained by the large Kolmogorov constant b in this model. Also in the mean-field model, the first maximum is considerably washed out if we assume the same large value of b, and, as the crossover to the $1/\omega$-decay regime is much earlier, the following maxima and minima are shrinked towards very small amplitudes. Therefore, we do not expect to observe these higher order maxima in the simulation anyhow, because at these small amplitudes fluctuations become too large. The large Kolmogorov constant indicates that in this model the energy fluctuations still are stronger than in the Navier-Stokes dynamics.

Also recent experiments in a cylinder between two counter rotating disks [24] revealed evidence for the response maxima. In addition they found a constant response amplitude for low driving frequencies and a $1/\omega$-decay of the velocity response for large frequencies. The experiments were performed with a modulated stirrer velocity. This may be more comparable to a modulated force instead of a modulated energy input rate. Therefore, we considered this case in the mean-field model as well as in the GOY model. For the energy response amplitude we basically find the same frequency behavior as for a modulated energy input rate, including the response maxima and minima in the mean-field model, see Fig.3.7. The GOY model shows the main maximum only due to large fluctuations, see Fig.4.3. The experimentally measured velocity response $\Delta_u = (u(t) - u_0)/u_0$, where $u(t)$ is the measured velocity modulus and u_0 is the (stationary) mean velocity, is connected to the energy response $E(t)/E_0$, which we calculated in our models, by

$$\frac{E(t)}{E_0} = \frac{u(t)^2}{u_0^2} = (1 + \Delta_u(t))^2 \simeq 1 + 2\Delta_u(t) + O(\Delta_u^2). \tag{6.1}$$

Here, E_0 denotes the mean (stationary) value of the energy. Δ_u will be small because also the modulation amplitude of the forcing is set to be small, i.e., the term $\propto O(\Delta_u^2) \ll 1$ is negligible in Eq.(6.1). Therefore, the $1/\omega$-decay for large driving frequencies, which is found in the experiments for the amplitude of Δ_u is in agreement with our findings of a $1/\omega$-decay for the amplitude of the energy response. The constant amplitude for low frequencies is found in experiments as well as in our models. In the case of a modulated force, the energy input rate is not a controlled quantity any more. In the experiments it has been measured as another response of the system which showed the main response maximum. In the mean-field approach we find the following behavior of the amplitude $A_{e_{in}}(\omega)$ of the energy input rate: It starts with a value of $A_{e_{in}}(\omega) \simeq 1.5$ for low frequencies and merges at 1 for large frequencies. This indicates, that at large frequencies the velocity does not feel the oscillation of the force any more, but the oscillation of the energy input rate is only a consequence of the oscillating force. At the frequencies, where the response amplitude $A(\omega)$ has maxima, the energy input amplitude $A_{e_{in}}(\omega)$ has “wiggles”, i.e., a maximum directly followed by a minimum. This indicates that in the case of a modulated driving force, the response maxima can also be measured in the energy input rate as has been done in the experiments. The GOY model again reproduces the basic trend of the mean-field results and also shows the main maximum in the amplitude $A_{e_{in}}(\omega)$. However, due to large fluctuations of the cascade time scale the higher order maxima are completely washed out. For confirmation it would be interesting to see whether the observed behavior of the energy input rate can also be observed in the REWA system.

In conclusion, the basic trend of the response function to a modulated driving as predicted by the mean-field theory can be reproduced by the numerical simulations which include turbulent fluctuations. Also, the main response maximum at a frequency connected to the energy cascade time scale can be observed in accordance with the mean-field results. This as well as the recent experiments which also show the basic features as predicted by the mean-field model clearly indicates, that these maxima are not an artifact of the mean-field model.

However, both numerical models have their artifacts as they either overestimate the fluctuations of the cascade time scale (GOY) or the Kolmogorov constant

b (REWA) which is connected to the energy transport through the system. Therefore, they may not be particularly suited to study the response maxima and minima in modulated turbulence. The fluctuations in the cascade time scale as calculated in the REWA simulation –which are considered to be more realistic than in the GOY model – are only small. This gives us some confidence that with a realistic Kolmogorov constant the main response maximum and possibly even the higher order maxima and minima may be observable in real turbulence. To further study the problem numerically, direct numerical simulations of the Navier-Stokes equation seem to be necessary. As we have seen in the two turbulence models, it is essential for analyzing modulated turbulence that all relevant time scales including their fluctuations are correctly described. Also experimentally it seems worthwhile to further investigate modulated turbulence. E.g., an interesting question would be whether the geometry of the turbulent system as used in [24] changes the response maxima. Furthermore, it would be worth to study different driving mechanisms. In [25] another kind of driving of the same experimental setup as used in [24] is investigated, namely there, the torque of the driving motors is controlled. This may be even more close to the modulated force as we have assumed it in our second case (right column, Table 6.1). It is shown in [25] that with this driving mechanism the fluctuations of the energy input rate are considerably less than with the controlled stirrer velocity that has been used in the experiments on modulated turbulence. Another option may be to modulate the energy input rate which seems to be possible in the same experimental setup, too [26].

Until now we have investigated flows where only one of the ideal properties, isotropy, homogeneity and stationarity, is broken. The mean-field theory seems to be quite successful in correctly describing some basic features of nonideal turbulent flows. However, as already mentioned in the Introduction, nature is more complicated. The snap of the snapping shrimp is one example (see Chapter 5). It has been demonstrated by experiments [27, 28] that the snapping sound is due to the collapse of a cavitation bubble which is produced by the fast water jet emitted from the claw during closure. This jet is clearly turbulent, anisotropic as well as inhomogeneous and time dependent. However, in this case, the essential part of the system results to be the cavitation bubble which produces the sound by its collapse. The dynamics of the bubble and the emitted sound can be modelled by a Rayleigh-Plesset type equation [29–31], while for the other components of the turbulent water flow assumptions have to be made. This equation describes the dynamics of the bubble radius R for a spherical bubble under a time dependent external pressure. The particular time dependence of the pressure is assumed as a Gaussian distribution, where its height and width are estimated only from the mean velocity and duration of the jet, respectively. This rough estimation is sufficient to correctly predict the dynamics of the bubble radius. The jet is turbulent, and therefore the velocity field will be considerably fluctuating, however, this does not seem to have an influence on the bubble dynamics. For a more detailed modeling of the bubble dynamics, the temporal and spatial shape of the velocity field around the snapper claw has to be known very accurately. Furthermore, the asphericity of the bubble collapse as well as the sound emission from bubble fragments have to be taken into account. The assumption of a spherical bubble leads to an overestimation of the emitted sound at bubble collapse as spherical bubbles collapse much more violently than aspherical ones. This would fairly complicate the model, however, it will not dramatically change the qualitative results from this simplified model.

In conclusion, simplified (mean-field) models as used in this thesis seem to be appropriate tools for describing some basic features of nonideal turbulence. Clearly, the limitations of these models are that they neglect turbulent fluctuations. The latter may change the mean-field properties in some cases, as e.g., the response maxima in modulated turbulence. However, those mean-field properties are (partly) observable in real turbulence and therefore are not artifacts of the model. We hope that the mean-field studies of this work will stimulate further experimental and numerical studies on fundamental properties of nonideal turbulence.

References

[1] H. Effinger and S. Grossmann, Z. Phys. B **66**, 289 (1987).

[2] S. Grossmann, A. von der Heydt, and D. Lohse, J. Fluid Mech. **440**, 381 (2001).

[3] I. Arad, V. L'vov, and I. Procaccia, Phys. Rev. E **59**, 6753 (1999).

[4] S. Kurien and K. R. Sreenivasan, Phys. Rev. E **62**, 2206 (2000).

[5] L. Biferale, D. Lohse, I. Mazzitelli, and F. Toschi, J. Fluid Mech. **452**, 39 (2002).

[6] L. Biferale and F. Toschi, Phys. Rev.Lett. **86**, 4831 (2001).

[7] A. von der Heydt, S. Grossmann, and D. Lohse, Phys. Rev. E, in press (2003).

[8] A. von der Heydt, S. Grossmann, and D. Lohse, *Numerical simulations of modulated turbulence*, Preprint, submitted to Phys. Rev. E (2003).

[9] E. B. Gledzer, Sov. Phys. Dokl. **18**, 216 (1973).

[10] M. Yamada and K. Ohkitani, J. Phys. Soc. Jpn. **56**, 4210 (1987).

[11] M. Yamada and K. Ohkitani, Prog. Theor. Phys. **79**, 1265 (1988).

[12] K. Ohkitani and M. Yamada, Prog. Theor. Phys. **81**, 329 (1989).

[13] M. H. Jensen, G. Paladin, and A. Vulpiani, Phys. Rev. A **43**, 798 (1991).

[14] L. Kadanoff, D. Lohse, J. Wang, and R. Benzi, Phys. Fluids **7**, 617 (1995).

[15] T. Bohr, M. H. Jensen, G. Paladin, and A. Vulpiani, *Dynamical Systems Approach to Turbulence* (Cambridge University Press, Cambridge, 1998).

[16] L. Biferale, Ann. Rev. Fluid Mech. **35**, 441 (2003).

[17] J. Eggers and S. Grossmann, Phys. Fluids A **3**, 1958 (1991).

[18] S. Grossmann and D. Lohse, Z. Phys. B **89**, 11 (1992).

[19] S. Grossmann and D. Lohse, Phys. Fluids **6**, 611 (1994).

[20] A. S. Monin and A. M. Yaglom, *Statistical Fluid Mechanics* (The MIT Press, Cambridge, Massachusetts, 1975).

[21] K. R. Sreenivasan, Phys. Fluids **7**, 2778 (1995).

[22] K. R. Sreenivasan and R. A. Antonia, Ann. Rev. of Fluid Mech. **29**, 435 (1997).

[23] S. B. Pope, *Turbulent Flows* (Cambridge University Press, Cambridge, 2000).

[24] O. Cadot, J. H. Titon, and D. Bonn, , *Experimental observation of resonances in modulated turbulence*, Preprint, submitted to J. Fluid Mech. (2002).

[25] J. H. Titon and O. Cadot, Phys. Fluids **15**, in press (2003).

[26] O. Cadot, 2003, private communication.

[27] M. Versluis, B. Schmitz, A. von der Heydt, and D. Lohse, Science **289**, 2114 (2000).

[28] M. Versluis, A. von der Heydt, D. Lohse, and B. Schmitz, Phys. Fluids **13**, S13 (2001).

[29] M. Plesset and A. Prosperetti, Annu. Rev. Fluid Mech. **9**, 145 (1977).

[30] A. Prosperetti and A. Lezzi, J. Fluid Mech. **168**, 457 (1986).

[31] C. Brennen, *Cavitation and Bubble Dynamics* (Oxford Press, New York, 1995).

Summary

Turbulent flows are ubiquitous. This holds for flows in nature such as the atmosphere of the earth or a waterfall as well as for many flows in engineering applications. The governing equation of fluid motion, the Navier-Stokes equation, is known since 150 years, and the basic properties can be understood from this equation. However, most (analytic) approaches to turbulence assume *ideal* flows, i.e., they assume homogeneity, isotropy and statistical stationarity. On the other hand, almost all realistic flows are *nonideal* in the sense that at least one of the above mentioned assumptions is broken. In this thesis several questions of nonideal turbulence are addressed on a fundamental level. A variable-range mean-field theory can be extended to weakly anisotropic as well as time dependent flows.

In Chapter 2 the scaling exponents of the second order velocity structure function for weakly anisotropic turbulence are derived within the mean-field theory. For this purpose, the structure function tensor is decomposed into its SO(3) invariants. In this decomposition, isotropic and anisotropic parts can be easily distinguished. For the isotropic part of the structure function, represented by the $j = 0$ sector in the SO(3) decomposition, Kolmogorov scaling is recovered. The scaling of the anisotropic parts ($j > 0$-sectors) is found to depend on the type of forcing. A – fairly general – non-analytic forcing leads to scaling exponents of 4/3 for *all* anisotropic sectors $j > 0$ whereas an analytic forcing leads to scaling exponents as high as $j + 2/3$. For $j = 0$ and $j = 2$ the results for the non-analytic forcing are in agreement with experimental and numerical data.

A time dependent driving to fully developed turbulence is considered in Chapter 3 within the variable-range mean-field theory. The response of the system to a modulated driving is observed in the second order moments of the large scale velocity difference $D(L,t) = \langle\!\langle (\boldsymbol{u}(x+L) - \boldsymbol{u}(x))^2 \rangle\!\rangle \propto Re^2(t)$ for varying driving frequency ω. For low frequencies the system can follow the oscillations of the driving, whereas for high driving frequencies the amplitude of the response decreases as $\propto 1/\omega$. In addition, the response amplitude shows alternating maxima and minima at frequencies connected with the frequency scale of the energy cascade and multiples thereof.

Turbulent fluctuations lead to a fluctuating energy cascade time scale. These are not included in the mean-field theory. In order to account for the effect of fluctuations, in Chapter 4 modulated turbulence is studied numerically within two dynamical cascade models of turbulence. The GOY shell model as well as the **re**duced **w**ave vector set **a**pproximation of the Navier-Stokes equation (REWA) automatically take into account turbulent fluctuations. The basic trend of the response amplitude as predicted by the mean-field theory can be reproduced, namely a constant amplitude for low driving frequencies and a $1/\omega$-decay for higher frequencies. The main response maximum can also be observed in both models, although it is weakened due to fluctuations. The higher order maxima and minima are fully washed out by fluctuations.

Finally, in Chapter 5 a nonideal example from nature is presented. The snapping shrimp (*Alpheus heterochaelis*) produces a loud snapping sound when rapidly closing its snapper claw. The snapping is among other things used to stun or kill prey animals. During claw closure a high velocity water jet is emitted which lets a cavitation bubble grow from the snapper claw. Experiments demonstrated that the snapping sound solely originates from the subsequent collapse of the cavitation bubble and not from the two claw surfaces hitting each other. A model for the bubble dynamics based on a Rayleigh-Plesset type equation is set up. The results for the time dependence of the bubble radius and the emitted sound are in remarkably good agreement with the experimental data.

Samenvatting

Turbulente stroming is bijna overal te vinden. Dat geldt zowel voor stromingen in de natuur zoals de atmosfeer van de aarde of een waterval als ook voor vele stromingen in de techniek. De vergelijking, die de beweging van een vloeistof beschrijft, is de Navier-Stokes vergelijking. Deze is sinds meer dan 150 jaar bekend en de belangrijkste eigenschappen van stromingen kunnen erdoor worden begrepen. In veel analytische benaderingen van turbulente stromingen wordt aangenomen dat de stroming *ideal* is, wat betekent, dat homogeniteit, isotropie en stationariteit worden verondersteld. De meeste realistische stromingen zijn echter *niet-iedaal*, doordat tenminste een van de genoemde voorwaarden niet van toepassing is. In dit proefschrift worden verschillende vraagstukken over niet-ideale turbulentie op een fundamenteel niveau benaderd. Een "variable range mean-field theory" voor ideale turbulentie kan uitgebreid worden voor zowel zwak anisotrope als tijdsafhankelijke turbulente stroming.

In Hoofdstuk 2 worden schalings exponenten van de tweede orde snelheidsstructuur-functie voor zwak anisotrope turbulentie afgeleid binnen de mean-field theorie. Daartoe wordt de structuurtensor in zijn SO(3)-invarianten ontleed. In deze decompositie kan makkelijk onderscheid gemaakt worden tussen isotrope en anisotrope delen. Voor het isotrope gedeelte van de structuurfunctie, dat gerepresenteerd wordt door het $j = 0$-deel in de SO(3)-decompositie, vinden wij de Kolmogorov schaling. Het gedrag van de anisotrope gedeelten ($j > 0$-sectoren) blijkt van het type aandrijving af te hangen. Een – relatief algemeen – niet-analytische aandrijving resulteert in een schalings exponent van 4/3 voor alle anisotrope sectoren $j > 0$, terwijl een analytische aandrijving tot hogere schalings exponenten, $j + 2/3$ leidt. Voor $j = 0$ en $j = 2$ stemmen de resultaten van de niet-analytische aandrijving overeen met zowel experimentele als numerieke data.

Een tijdsafhankelijke aandrijving van volledig ontwikkelde turbulentie wordt in Hoofdstuk 3 met hulp van de "variable range mean-field theory" benaderd. Hier wordt de respons van het systeem op een gemoduleerde aandrijving waargenomen in de tweede momenten van de snelheidsverschillen op grote schaal, $D(L, t) = \langle\langle(\boldsymbol{u}(x + L) - \boldsymbol{u}(x))^2\rangle\rangle \propto Re^2(t)$ voor variërende aandrijvingsfrequentie ω. Als de frequentie klein is, kan het systeem de oscillaties van de aandrijving volledig volgen, terwijl voor grote frequenties de amplitude van de respons afneemt als $1/\omega$. Bovendien heeft de respons-amplitude afwisselend maxima en minima bij bepaalde frequenties, die gerelateerd zijn aan de frequentie schaal van de energie cascade en veelvouden daarvan.

Turbulente fluctuaties zorgen voor een fluctuerende tijdschaal van de energie cascade. Deze fluctuaties zijn niet in de mean-field theorie inbegrepen. Om rekening te houden met het effect van fluctuaties bestuderen we gemoduleerde turbulentie ook numeriek met twee dynamische cascade modellen voor turbulentie in Hoofdstuk 4. Beide modellen, het “GOY-shell model” en de “reduced wave vector set approximation” van de Navier-Stokes vergelijking, bevatten automatisch turbulente fluctuaties. De essentiële trend van de respons-amplitude zoals voorspeld door de mean-field theorie wordt gereproduceerd: zowel de constante amplitude voor kleine aandrijvingsfrequenties als ook de $1/\omega$-daling voor hoge frequenties worden in de modellen waargenomen. Het hoofdmaximum van de respons wordt in beide modellen gezien, hoewel het verzwakt is door de fluctuaties. De volgende maxima en minima van hogere orde zijn niet meer zichtbaar vanwege de fluctuaties.

Afsluitend presenteren wij in Hoofdstuk 5 een niet-ideaal voorbeeld uit de natuur. De pistoolgarnaal (*Alpheus heterochaelis*) maakt indrukwekkende knallen onder water door zijn schaar met grote snelheid dicht te klappen. De knallen worden door de garnalen gebruikt om te communiceren, maar ook om een prooi te verdoven en zelfs om te doden. Door de sluitbeweging van de schaar wordt het water tussen de schaarhelften met hoge snelheid weggespoten. Dit leidt tot een daling van de druk, waardoor een “cavitatie” bel kan groeien. Experimenten hebben laten zien, dat het geluid alleen door de implosie van deze bel wordt veroorzaakt, en niet door de dichtslaande schaarhelften. Een model voor de dynamica van de bel wordt ontwikkeld op grond van de Rayleigh-Plesset vergelijking. De resultaten uit het model voor de tijdafhankelijkheid van de straal van de bel en het geluid zijn in opmerkelijk goede overeenstemming met de experimentele data.

Zusammenfassung

Turbulente Strömungen gibt es fast überall. Beispiele finden sich sowohl in der Natur, etwa die Erdatmosphäre oder ein Wasserfall, als auch in vielen technischen Anwendungen. Die Gleichung für die Bewegung eines Fluids, die Navier-Stokes Gleichung, ist seit über 150 Jahren bekannt. Die wesentlichen Eigenschaften von Strömungen können aus dieser Gleichung verstanden werden. In den meisten analytischen Ansätzen für turbulente Strömungen werden allerdings *ideale* Strömungen behandelt, d.h. Homogenität, Isotropie und Stationarität werden vorausgesetzt. Reale Strömungen sind jedoch fast immer *nicht-ideal* in dem Sinne, daß mindestens eine der oben genannten Eigenschaften nicht vorliegt. In dieser Arbeit werden einige Fragestellungen nicht-idealer Turbulenz von den Grundlagen aus behandelt. Eine für ideale Strömungen entwickelte skalenabhängige Mean-Field-Theorie kann sowohl für schwach anisotrope als auch für Strömungen mit zeitabhängigen Antrieb erweitert werden.

In Kapitel 2 werden die Skalenexponenten der Geschwindigkeits -Strukturfunktion zweiter Ordnung für schwach anisotrope Turbulenz im Rahmen der Mean-Field-Theorie hergeleitet. Dazu wird der Strukturfunktionstensor in seine SO(3)-Invarianten zerlegt. In dieser Zerlegung können isotrope und anisotrope Anteile leicht unterschieden werden. Für den isotropen Anteil der Strukturfunktion, der durch den $j=0$–Term in der SO(3)-Zerlegung dargestellt wird, findet man das erwartete Kolmogorov-Skalenverhalten. Das Skalenverhalten der anisotropen Teile dagegen hängt von der Art des Antriebs ab. Ein – relativ allgemeiner – nicht-analytischer Antrieb ergibt für die Skalenexponenten *aller* anisotropen Terme $j > 0$ denselben Wert $4/3$, während ein analytischer Antrieb zu mit j anwachsenden Skalenexponenten $j+2/3$ führt. Die Ergebnisse im Falle eines nicht-analytischen Antriebs stimmen mit experimentellen Daten überein, die für $j = 0$ und $j = 2$ vorliegen.

Vollentwickelte Turbulenz mit einem zeitabhängigen Antrieb wird in Kapitel 3 im Rahmen der Mean-Field-Theorie behandelt. Die Antwort des Systems läßt sich an den Momenten zweiter Ordnung der Geschwindigkeitsdifferenzen auf großen Skalen, $D(L,t) = \langle\!\langle (\boldsymbol{u}(x+L) - \boldsymbol{u}(x))^2 \rangle\!\rangle \propto Re^2(t)$, ablesen: sie reagieren auf verschiedene Antriebsfrequenzen mit unterschiedlicher Amplitude. Bei kleinen Frequenzen kann das System den Oszillationen des Antriebs folgen, während für große Antriebsfrequenzen die Amplitude der Antwort mit $\sim 1/\omega$ abnimmt. Außerdem zeigt die Amplitude der Antwort bei bestimmten Antriebsfrequenzen abwechselnd Maxima und Minima. Diese Frequenzen werden durch die Frequenzskala der Energie-Kaskade und Vielfachen derselben bestimmt.

Turbulente Fluktuationen sorgen dafür, daß die Kaskaden-Zeitskala fluktuiert. Diese Fluktuationen sind in der Mean-Field-Theorie nicht enthalten. Um den Effekt der Fluktuationen zu berücksichtigen untersuchen wir in Kapitel 4 modulierte Turbulenz numerisch mit Hilfe von zwei verschiedenen dynamischen Kaskaden-Modellen. Sowohl das „GOY-shell model“ als auch die „reduced wave vector set approximation“ der Navier-Stokes Gleichung (REWA) führen automatisch zu turbulenten Fluktuationen. Die wesentlichen Eigenschaften der Antwort-Amplitude, wie sie von der Mean-Field-Theorie vorhergesagt werden, können reproduziert werden, nämlich eine konstante Amplitude für kleine Antriebsfrequenzen und ein $1/\omega$-Abfall der Amplitude für hohe Frequenzen. Das Hauptmaximum der Antwort wird in beiden Modellen beobachtet, allerdings wird es durch die Fluktuationen abgeschwächt. Die in der Mean-Field-Theorie folgenden Maxima und Minima höherer Ordnung werden vollständig durch die Fluktuationen „ausgewaschen“.

Abschließend wird in Kapitel 5 ein Beispiel nicht-idealer Turbulenz aus der Natur betrachtet. Der Pistolenkrebs (*Alpheus heterochaelis*) erzeugt laute Knalle unter Wasser durch schnelles Zusammenklappen seiner Schere. Die kraftvollen Laute werden zur Kommunikation untereinander verwendet, aber auch kleine Beutetiere können dadurch geötet werden. Beim Schließen der Schere wird ein Wasserstrahl ausgestoßen. Während die Wassergeschwindigkeit ansteigt, sinkt der Wasserdruck. Dadurch entsteht eine Kavitationsblase, die auf eine Größe von einigen Millimetern anwachsen kann. Experimente haben gezeigt, daß der Knall allein durch die Implosion dieser Blase erzeugt wird, und nicht durch das Zusammenschlagen der Schere, wie man zunächst glaubte. Ein Modell für die Blasendynamik aufgrund der Rayleigh-Plesset Gleichung wird entwickelt. Die Ergebnisse des Modells für die zeitliche Entwicklung des Blasenradius’ und des emittierten Schalls stimmen bemerkenswert gut mit den experimentellen Daten überein.

Acknowledgments

I would like to thank all people who contributed to this work in different ways.

First of all I thank my two promotors, Detlef Lohse and Siegfried Grossmann, for agreeing in supervising me and for their continuous support and patience also during difficult times. I am grateful for the many motivating and stimulating discussions.

I also would like to thank Michel Versluis who performed the experiments with the snapping shrimp.

Special thanks to my (over the years changing) office mates, Judith Rensen, Bas Benschop, Irene Mazzitelli, Philippe Marmottant, and Devaraj van der Meer for the nice atmosphere, countless cups of tea and for improving my Dutch.

A big thank you to all people who corrected this thesis and made helpful remarks.

Furthermore I would like to thank all other members of the group “Physics of Fluids”: Leen van Wijngaarden, Andrea Prosperetti, Gerrit de Bruin, Sascha Hilgenfeldt, Ko van der Weele, Henni Scholten, Gert-Wim Bruggert, Joanita Leferink, Marianne van der Linde, Claus-Dieter Ohl, Federico Toschi, Stefan Luther, Marie Caroline Jullien, Kengo Ichiki, Rüdiger Tögel, René Mikkelsen, Florine Meijer, Mark Stijnman, Manish Arora, and of course also the master students for the encouraging working environment.

I am grateful to my parents and my sister who always supported me and had great interest in the forthcoming of this thesis.

In particular, I would like to thank André Mischke for his support and patience through many years and for the exciting life besides Physics.

Anna von der Heydt
Enschede, April 2003

About the Author

Anna von der Heydt was born on April 29, 1974 in Regensburg, Germany. After graduating from high school at the Max-Planck Gymnasium in Göttingen in 1993, she began a study in Physics at the Philipps-University Marburg in March 1994. After the Vordiplom in 1996 she had several tutorial positions in the Departments of Physics and Mathematics. In 1997 she became a fellow of the Studienstiftung des deutschen Volkes and graduated in 1999 in Physics (Diploma). In September 1999 she joined the Physics of Fluids group of Prof. Detlef Lohse at the University of Twente as a PhD student. Starting March 2003 she will be a Post-Doc at the Institute for Marine and Atmospheric Research (IMAU) in Utrecht.